**Technische Universität Wien**

# Temperature Stabilization and Modular Design Approach for Microfluidic Systems

by

Michael Unger

Supervisor:

Ao.Univ.Prof. Dipl.-Ing. Dr.techn. Johann Nicolics

A thesis presented for the
degree of Doctor of Technical Sciences

in the

Faculty of Electrical Engineering and Information Technology
Institute of Sensor and Actuator Systems

30. November 2018

# Declaration of Authorship

I, Michael Unger, declare that this thesis titled, 'Temperature Stabilization of Microfluidic Systems' and the work presented in it are my own. I confirm that:

- This work was done wholly or mainly while in candidature for a research degree at this University.

- Where any part of this thesis has previously been submitted for a degree or any other qualification at this University or any other institution, this is clearly stated.

- Where I have consulted the published work of others, this is always clearly attributed.

- Where I have quoted from the work of others, the source is always given. With the exception of such quotations, this thesis is entirely my own work.

- I have acknowledged all main sources of help.

- Where the thesis is based on work done by myself jointly with others, I have made clear exactly what was done by others and what I have contributed myself.

Signed:

_____

Date:

_____

| Reviewer 1: | Reviewer 2: |
|:---:|:---:|
| Ao.Univ.Prof. Dipl.-Ing. Dr.techn. | Univ.Prof. Dipl.-Ing. Dr. |
| Franz Keplinger | Peter Ertl |

# *Abstract*

**Temperature Stabilization and Modular Design Approach for Microfluidic Systems**

by Michael Unger

Microfluidics is a wide field where applications span microbiological applications such as cancer cell detection, blood analysis, chemical synthesis, spectroscopy and much more. Microfluidic chips are usually made from silicon, plastics or glass where the channel size is limited by the material and manufacturing technology. If a certain technology is applicable for a given task, temperature range, the material itself and its mechanical properties, electrical characteristics and temperature stability have to be taken into account.

The LTCC (Low Temperature co-fired Ceramics) technology opens a wide field of application due to its layer based manufacturing process and the ability to create 3D-structures in a 2.5D process where electrical functions, high temperature stability, mechanical robustness and chemical inertness as well as bio compatibility can be combined in a single module. Depending on the LTCC-material used, limitations are encountered in the different criteria. Therefore, several materials have been characterized and their stability tested.

For the temperature control, an analytical method for predicting the temperature deviations was established and a test module designed. This design potentially replaces a bulky Peltier temperature-control system for the use inside a blood-gas analysis system. The test modules were developed using FE-simulations and prototypes were built and characterized.

A through flow heater for further improvement of the module performance was designed and prototypes built and investigated.

In order to employ a modular design methodology using building blocks in a printed circuit board or an LTCC software package, a procedure for transfer of highly complex layered geometry data was devised. Because the amount of model data plays an important role, new algorithms for data reduction of the model geometry were developed.

# *Kurzfassung*

## Temperaturstabilisierung und Modularer Designansatz für Mikrofluidiksysteme

verfasst von Michael Unger

Mikrofluidik ist ein breites Feld und umspannt zahlreiche Anwendungen wie Krebszellenerfassung, Blut Analyse, chemische Synthesen, Spektroskopie und vieles mehr. Mikrofluidik-Chips werden üblicherweise aus Silizium, Kunststoffen oder Glas gefertigt, wobei die Kanalgröße durch das Material und den Herstellungsprozess eingeschränkt ist. Ob eine bestimmte Technologie anwendbar ist, wird durch das Material und seine Eigenschaften bestimmt, wobei sowohl mechanische und elektrische Kenngrößen als auch die thermische Beständigkeit des Materials ausschlaggebend sind.

Die LTCC (Low Temperature Co-fired Ceramics)-Technologie eröffnet ein breites Anwendungsfeld, da es sich um eine Lagen-basierende (2.5D) Herstellungstechnik handelt und dadurch die Herstellung von 3D-Strukturen ermöglicht wird. Dabei können sowohl elektrische Funktionen als auch Eigenschaften wie hohe Temperaturbeständigkeit, mechanische Robustheit und chemische Beständigkeit sowie Biokompatibilität in einem Modul vereint werden. In Abhängigkeit der Einschränkungen, die vom Material ausgehen, müssen die Materialien bezüglich ihrer Stabilität und Eignung charakterisiert werden.

Für die Temperaturregelung wurde eine analytische Methode entwickelt, die es erlaubt, Abweichungen der Temperaturverteilungen vorherzusagen und zu optimieren und ein potenziell sperriges Peltier-Temperaturregelsystem eines Blut-Gas-Analysesystems unter Zuhilfenahme der FE-Simulation zu miniaturisieren und Prototypen herzustellen, und diese zu charakterisieren.

Ein Durchlauferhitzer zur weiteren Verbesserung der Temperaturprofilgüte und Dynamik des Systems wurde ebenfalls entworfen, hergestellt und ausgemessen.

Um modulare Designverfahren komplexer Mikrofluidikmodule einsetzen zu können, musste auch ein Verfahren entwickelt werden, um hochkomplexe lagenbasierte Module, die in einem Leiterplatten bzw. LTCC Softwarepaket entworfen werden, in die Simulationssoftware einlesen zu können. Dabei spielt auch die Datenmenge eine Rolle, die bei der Datenkonversion auftritt, weshalb auch Algorithmen zur Reduktion der Modelldaten entwickelt wurden.

# *Acknowledgements*

# Contents

# List of Figures

# List of Tables

# List of Abbreviations

| | |
|---|---|
| $Al_2O_3$ | Alumina |
| $E_A$ | Activation Energy |
| 3D | Three-dimensional |
| CAD | Computer Aided Design |
| CCD | Charge Coupled Device |
| CNC | Computer Numerical Controlled |
| CPE | Constant phase element |
| CTA | Column Type Array |
| CTE | Coefficient of Thermal Expansion |
| DNA | Deoxyribonucleic acid |
| EDS | Energy-dispersive X-ray Spectroscopy |
| EIS | Electrochemical Impedance Spectroscopy |
| FE(M) | Finite Element (Method) |
| HPLC | High Performance (or pressure) Liquid Chromatography |
| HTCC | High temperature co-fired ceramic |
| LTCC | Low temperature co-fired ceramic |
| NTC | Negative temperature coefficient |
| PCB | Printed Circuit Board |
| PCR | Polymerase Chain Reaction |
| PMMA | Polymethylmethacrylat |
| PS | Polystyrene |
| PTC | Positive temperature coefficient |
| PTFE | Polyterafluorethylene |
| RNA | Ribonucleic acid |
| SEM | Scanning Electron Microscopy |
| SMT | Surface-Mount Technology |
| Taq | Thermus aquaticus Polymerase |
| TCR | Temperature Coefficient of Resistance |
| XRD | X-ray Diffraction |

# Chapter 1

# Introduction

Since ancient times ceramic products have been created as decoration objects, containers and tools. Over time, the use of purified raw materials from nature have been replaced by synthetically mass produced highly pure powders where high performance ceramics with defined physical properties were created. This ranges from cutting tools, thermal insulators, temperature shock resistant sheets like Ceran®, electrical circuit carriers (thick-film technology, LTCC, HTCC) to human body implants. The application of ceramic materials as biocompatible implants (artificial joints) is state of the art now. Still, ceramic is an expensive material because of its high manufacturing effort and not widely used for microbiological, chemical and general microfluidic applications. The material itself is rather cheap, but to obtain a product many steps are necessary and a lot of optimizing for the sintering process must be conducted. Therefore, mainly glass and disposable plastics are used as far as possible. The same is true for chemical synthesis where borosilicate glass is the standard material for reaction vessels followed by PTFE. In the industrial field, special corrosion resistant steel alloys or enameled steel vessels are employed. For laboratory-sized synthesis, miniature glass reactors are available but offer a limited pressure and temperature range. The following chapter gives an overview of potential applications where the use of LTCC-technology because of mechanical, thermal, electrical and chemical properties of the materials are beneficial and also because of the need of a precise temperature control.

## 1.1 Microbiological and analytical applications

### 1.1.1 Column chromatography

Column chromatography is a separation technique that allows separating compounds based on their retention time inside a packed column as shown in figure 1.1. While this technique is used for post-processing reactions to isolate the desired compound it is also used for analytical purposes as High Performance (or pressure) Liquid Chromatography (HPLC) at elevated pressure at around 60 bar. The substance to be analyzed is eluated/dissolved and the molecules travel through the column while interacting with the porous column packing depending on their charge and hydrophilic or hydrophobic nature. The charge of the molecules itself depends on the pH-value of the eluent and can be controlled during the process to achieve optimal separation. At the end of the column, usually an optical detector is employed that gives a signal proportional to the concentration of the current molecules species. The optimum separation of a column is when the output signal reaches the baseline (base-line separated). While usually the analysis is carried out near room temperature, HPLC at higher temperature up to 100 °C has also been investigated [10]. Carr et al. found a significant change in the retention



Entry of column

Eluent

Sample applied on top of column filling (stationary phase)

Separation of molecule species due to different migration speed along column

Stationary phase (e.g. alumina or silica)

Separated compounds

Exit of column

Detector

Light source
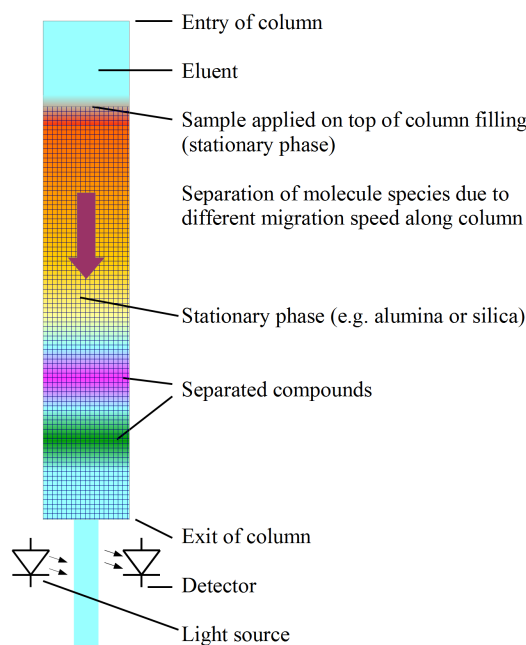
FIGURE 1.1: Schematic of column chromatography.

parameters over temperature as can be seen in figure 1.2. The chromatographic retention $SP$ in equation 1.1 denotes a logarithmic capacity factor of a molecule species. The subscript 2 designates a solute property such as molar volume ($V_2/100$), polarizability-dipolarity ($\pi_2^*$), hydrogen bond acidity ($\alpha_2$), or hydrogen bond basicity ($\beta_2$). $SP_0$ is an

independent retention introduced by the column (intercept), the coefficients $m,s,a$ and $b$ are obtained by experiment and fitting parameters of the mathematical equation to the measured characteristics. For a given phase system consisting of stationary phase and eluent, a measure of separation between two compounds can be obtained by subtracting the chromatic retention of the two compounds. [4, 11, 12].

While the temperature stability or distribution might be "good enough" for a small quantity of known compounds, this situation changes when a multitude of compounds is present and separation suffers. The molecule species can "overtake" each other based on the temperature dependent retention time in extreme cases. In this case, chromatography needs highly stable conditions for operation.

$$SP = SP_0 + m \cdot V_2/100 + s\pi_2^* + a\alpha_2 + b\beta_2 \tag{1.1}$$



(a) m-parameter
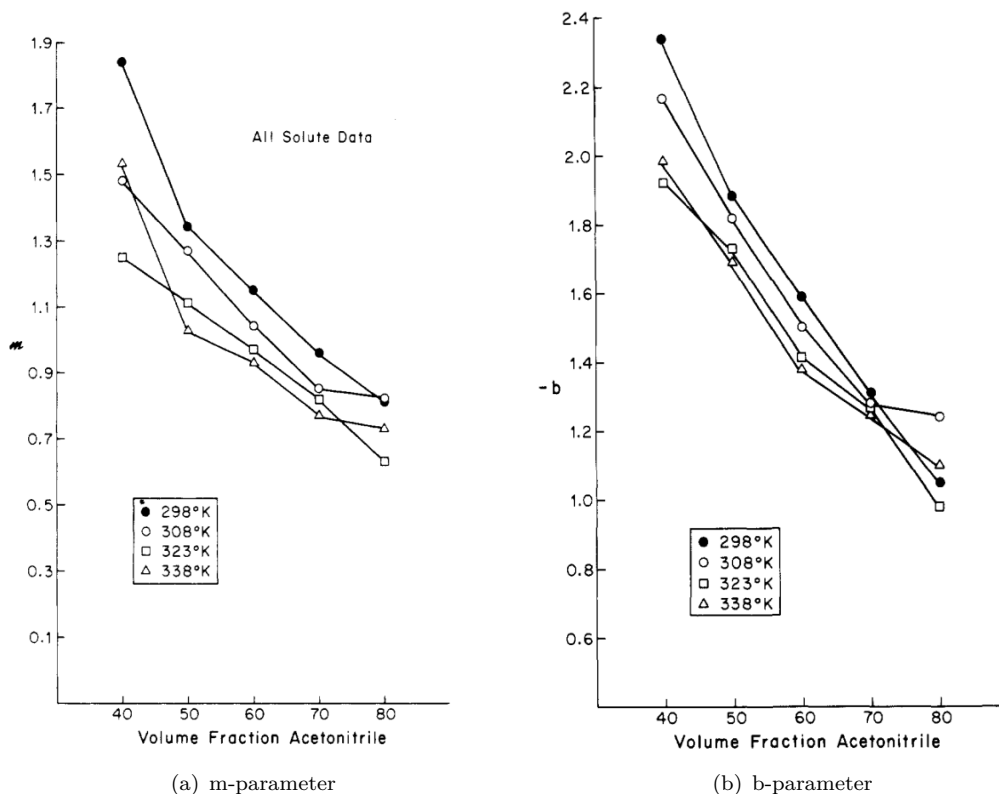
(b) b-parameter

FIGURE 1.2: Temperature dependence of retention parameters [4].

## 1.1.2 Enzymatic measurement methods

The basic principle of enzymatic measurement methods is the use of a selectively acting enzyme that processes the substance to be detected (analyte) where the change of a

parameter or the secondary substance itself can be detected (photometric absorption, polarization, electric conductivity, fluorescence, etc.). For an automated measuring system, the detection itself is preferably done by a method that delivers an electronic signal. In case that optical properties change such as absorption, polarization or fluorescence a photo-diode or a CCD detector with an optical filter can be employed. In certain cases, it is possible to use electrolysis to translate the amount of a substance into a charge, which is the quantitative indicator for the molar amount. One of the classic examples of enzymatic measuring methods is the blood glucose content measurement. The measuring principle relies on the enzyme glucose oxidase which decomposes glucose into a lactone and hydrogen peroxide ($H_2O_2$) as shown in figure 1.3. Enzymatic glucose detec-
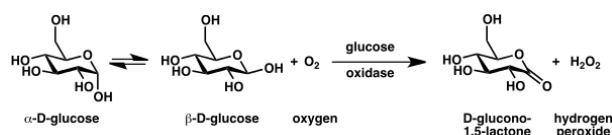


FIGURE 1.3: Glucose-Oxidase reaction:
$$Glucose + O_2 \longrightarrow D-glucono-1,5-lactone + H_2O_2$$

tion uses an electrode instead of $O_2$ to take up the electrons needed to oxidize glucose and to produce an electric current[13]. The total amount of charge that is passed as current through the cell is equivalent to the total amount of glucose in the blood sample. The accuracy of the measuring principle is determined by the volume of the sample and the temperature that greatly influences enzyme activity. As an example the activity of alkaline-phosphatase which was essayed by Peterson et al. [5] is shown in figure 1.4. The enzyme shows a maximum activity around $37\,^{\circ}C$ which correspond to the normal body temperature. All enzymes show such a behavior but the temperature range is matched to the living environment of the organism (e.g. bacteria living in the arctic or near volcanoes at the bottom of the ocean.) The problem of the reproducibility of the sample volume can be solved by using a capillary that automatically takes up the right amount of blood from the sample. The temperature sensitivity itself is not a problem as long as the temperature is kept in the activity range of the enzyme and a long enough measurement time is allowed. Because the measurement accuracy is high enough small portable units with disposable capillary assemblies are now widely used by diabetes patients as glucometers [13]. A measurement device was already realized as LTCC module [14]. If a fast cyclic sample exchange (mass sample analyses) or continuous measuring setup is needed (online patient monitoring in intensive care) that require highly temperature stable operation (e.g. enzymatic measuring techniques or other temperature sensitive applications like blood gas analyses) often bulky setups with Peltier-temperature controllers are used in these situations. This makes it extremely hard or impossible to design a small portable unit [15].
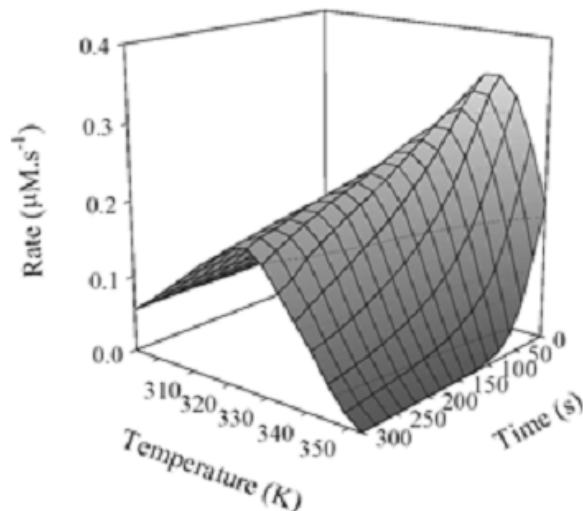
FIGURE 1.4: Temperature activity of alkaline-phosphatase [5].

### 1.1.3 Optical detection

Column chromatography and enzymatic measuring methods are usually coupled with optical detection in order to quantify the analyte. The problem is that under different pH or at different temperatures a wavelength shift or change in quantum efficiency can occur which influences the accuracy of the measurement. Figure 1.5 shows a significant change of optical properties of Chlorophyll A in the relevant temperature range of 25 to 37 °C. Ross et al have used a temperature sensitive Rhodamine B solution (figure 1.6) to measure the temperature inside a microfluidic channel [7]. Not only absorption and emission maxima but also excited state lifetime and wavelength might be temperature dependent. Although these dyes might not be directly related to microbiological measurements it gives a good impression that optical properties of chemical compounds can vary with temperature to a great extent. Significant amounts of stains and dyes have been developed for hematology, histology and chromatography. An enormous amount of laser dyes as optical amplifier has been investigated [16] and many of them such as chlorophyll occur in different organisms.

### 1.1.4 DNA replication by polymerase chain reaction (PCR)

The polymerase chain reaction is a means of multiplying DNA fragments in order to increase the amount of DNA for further processing (e.g. forensic identification). The PCR is based on a very simple principle of overheating the DNA (denaturing) to 97 °C in order to split it in two half strands. After that, primer binding is accomplished at 48 to 69 °C where the double strand rebuild is started. After priming, the Taq-polymerase is reconstructing the full strands by coupling amino acids are contained in the reaction
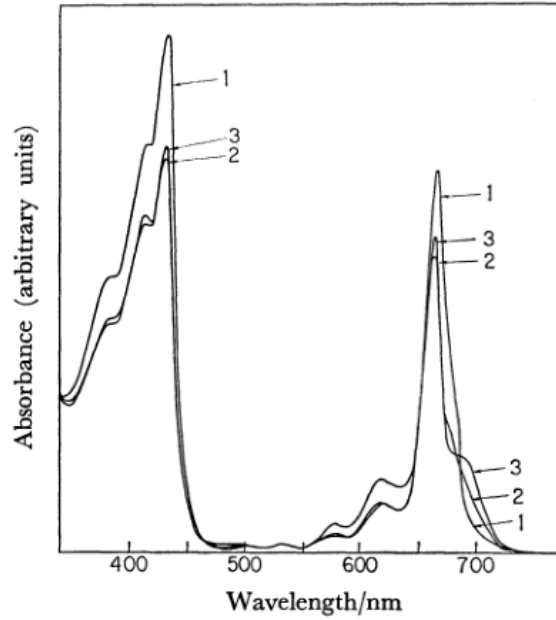
FIGURE 1.5: Temperature dependent absorption of chlorophyll A (one of the dyes used in photosynthesis) in 3-methylpentane solution [6].
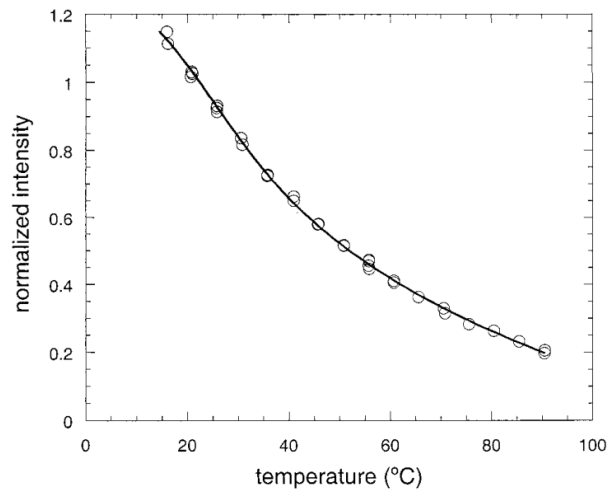


FIGURE 1.6: Normalised fluorescence intensity as a function of temperature used to calibrate the fluorescence-based temperature measurement [7].

medium. In the ideal case, the number of DNA-strands is doubled with each cycle. Microfluidic chip modules and LTCC modules have been already developed by several research groups [17, 18] greatly decreasing the size of the apparatus previously used.

## 1.2   Chemical synthesis

The application of thermally optimized ceramic reactors can be beneficial in different fields of synthesis. Chemical synthesis often involves fast exothermic reaction requiring

6

proper thermal management. For reactions that are performed under harsh conditions like elevated temperature and high pressure or high temperature reactions over 500 °C where borosilicate glass reactors cannot be used anymore ceramic, quartz or enameled steel is the only option.

### 1.2.1 Exothermic temperature sensitive reactions

Many reactions are fast and exothermic and are difficult if not impossible to conduct in typical reaction vessels. A whole field of fast and simple reactions are summarized under the term "flash chemistry". The problems with such fast and exothermic reactions include polymerization, side product formation or unwanted racemization of the product. In such a case, the reaction must be carefully analyzed and a proper reactor designed to allow efficient cooling of the reaction medium. Depending on the amount of heat liberated even synthesis in a 25 ml flask can lead to extremely low yields. Figure 1.7 and table 1.1 show the schematic and the yields of the Swern-Moffat oxidation in different reaction setups[8]. The Swern-Moffat reaction converts secondary alcohols to ketones and primary alcohols to aldehydes. The reaction between cyclohexane-carboxylic acid and oleum is another example of an exothermic reaction that leads to by-product formation, which reduces the yield of the mixed acid anhydride [19].

| Method | Residence time $t_{R1}$ | T in °C | Selectivity of cyclohexanone |
|---|---|---|---|
| Micro reactor | 2.4 | -20 | 88 |
| | 0.01 | 0 | 89 |
| | 0.01 | 20 | 88 |
| Flask | | -20 | 19 |
| | | -70 | 83 |

TABLE 1.1: Swern-Moffatt oxidation of cyclohexanol using a microreactor and a flask.[8]
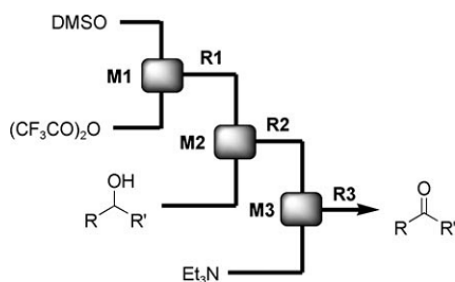


FIGURE 1.7: A micro reactor system for room temperature Swern-Moffatt oxidation: M1, M2, M3: micro-mixers. R1, R2, R3: microtube reactors.[8]

However, some synthesis require a minimum temperature for the reaction to start but also have a maximum temperature only several degrees above starting temperature where side product formation or polymerization becomes prohibitive. Because higher temperature means higher energy in the system, a direct synthesis might not be possible and makes it necessary to employ protection groups or perform the synthesis in several steps to avoid bad yield. However, a mini- or microreactor may be designed allowing the synthesis to be run under optimal reaction conditions. The rather small synthesis throughput can be increased by running microreactors in parallel where LTCC as mass production technology can be fully utilized.

### 1.2.2 High pressure and mid temperature range reactions

These types of reactions are usually conducted inside an autoclave at temperatures $<300\,°C$ and pressures up to 60 bar as hydrothermal synthesis[20]. These reactions include carbonylations [21], deoxygenations of carbonic acids like benzoic acid [22] and oxidations of alkyl-aromatic compounds to carboxylic acids [23]. Using potentially poisonous, corrosive and lethal chemicals makes it unattractive to investigate such reactions in a lab when the reaction conditions include water at $250\,°C$ and high pressure. Therefore, such synthesis are scaled down and investigated using microreactors made of etched glass or are performed in metal capillary tube reactors. The disadvantage is that due to thermal expansion in hot regions stress can appear leading to rupture of the glass reactor. The metal capillary approach is also not always suited because of the required chemical inertness of the reaction tube. An alternate approach is to use a PTFE-tube which is reinforced by a metal part to withstand the pressure; However the temperature range is limited to about $250\,°C$. In contrary, ceramic reactors using HTCC- or LTCC-technology can be designed to withstand 60 bars [24], at elevated temperature the decrease in Young's modulus must be taken into account.

### 1.2.3 High temperature reactions

High temperature reactions up to $700\,°C$ are usually used for the petrochemical industry. The reaction setup usually includes a protective gas system (e.g. using Argon to prevent oxidation) and a tube furnace. A well-known application is the dehydration of acetic acid to acetic anhydride or acetone to ketene [25]. It is possible to design LTCC reactors for operating temperatures (only) below $700\,°C$, since LTCC materials frequently start softening already at this temperature. For even higher reaction temperatures, HTCC-ceramic is appropriate with a softening temperature well beyond $1000\,°C$. The high

pressure range as can be utilized at room temperature is not applicable at high operation temperature.

## 1.3  Motivation

It is easily verified, that numerous applications require a precise and stable temperature distribution and are influenced by changing boundary conditions. This is why temperature regulation is an important integral part of a microfluidic system. Depending on the application and location of operation (in the field or in the lab) the size can also play an important role. The temperature control can be a major problem if a system should be miniaturized to create a portable unit while maintaining the quality of the temperature stability especially when several section on the same module need different stable temperature levels. In order to control the temperature the main components are the heater or cooler, the temperature measurement and the regulator or controller. The overall microfluidic module can be too complex to be optimized in a single step. It would be highly desirable if the module could be split into independent building blocks. Those blocks can be one of the following:

- Thermally passive blocks that do not change the temperature (they do not release or consume thermal energy) like Sensor-cells, mixers and connectors.

- Thermal insulation of building blocks to suppress mutual influence (high temperature section must not overheat low temperature section).

- Thermally active blocks that change the temperature by liberating or consuming thermal energy like reactors, heaters and coolers.

- Interface blocks connecting the fluid lines, which can have any temperature to the internal function blocks such as flow-through heater or cooler for inflowing or outflowing medium.

The idea is to design blocks with equal temperature at the lateral boundaries when exposed to the chosen boundary conditions at upper and lower surfaces. Although the method of arranging such function blocks might not be optimal for achieving maximum miniaturization it greatly eases the design of such systems. If a fluid is to be kept at constant temperature even without any endothermic or exothermic effects, a heating or cooling solution can only be designed if the fluid itself does not influence the temperature profile. This means the fluid has to remain static or in a stationary flow, which basically negates the possibility to exchange it discontinuously unless it already has the desired temperature when it enters the critical section of the module.

A second important application for the temperature field synthesis is the control of thermomechanical stresses that arise from a temperature gradient inside a device. If a part of a substrate is hotter than its circumferential part (even if only one material is involved) it will tend more to expand but will be hindered by the cooler surrounding structure. This leads to bulging of the material and results in a bad thermal contact or the destruction of the device due to excessive thermomechanical loads.

The following chapter focuses on a method to easily creating complex systems by defining boundary conditions and dividing these systems into building blocks. Latter ones can be assembled arbitrarily to form the desired function - basically a Thermo-"LEGO®" that is based on electronic schematics programs and PCB layout CAD systems. The overall system will differ in its performance from the separately designed and optimized blocks. A major task will be to transfer the data of the whole - now complex - physical model as a 3D-model into the simulation package allowing for multiphysics simulation (electrical, piezo-electric, thermal, thermo-mechanical, fluidic, magnetic, etc.). This procedure has to be done for rather simple geometries and building blocks as well as for the whole highly complex device.

# Chapter 2

# Modular Design

## 2.1 Design process

In order to achieve a highly stable temperature distribution it is necessary to protect the device from unforeseen influence like parasitic air streams or wind caused by other appliances or thermal and solar radiation imposing a temperature gradient onto the module. Furthermore, the different sections like mixers, heated or cooled reactors, measuring ports, etc. have a different influence on the complete module and make it quite complicated to find an optimal solution for the whole structure. The first step in designing the heater or cooler structure for the desired temperature distribution is to determine the operating environment of the module such as freely operated inside a lab or inside an appliance where it might be exposed to air streams from cooling fans. If the environmental influence is strong but not (sufficiently) predictable, it is crucial for further design to protect the module from such influences. The most obvious solution is to mount the module inside an enclosure and achieve stable boundary conditions. Figure 2.1 illus-
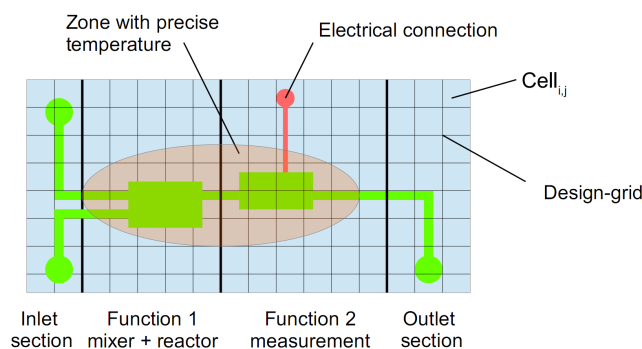


FIGURE 2.1: Design concept using separately optimized sections illustrating the subdivision into cells inside a grid.

trates the design concept showing the building blocks for different functions. In order to

optimize the blocks separately the mutual influence of these blocks is simply considered non-existent. The reason is that each module subsection will be designed in such a way that they have the same temperature along the interfaces. For blocks with significant temperature differences lateral boundary conditions are defined to substitute for the rest of the module. The subdivision into building blocks also matches the technique of sub-modeling when using finite element analyses (FEM) where the adjacent section is only represented as boundary condition instead of considering the model of the adjacent block. Most importantly, the fluid that enters the module is simply considered to have already the desired temperature and thus fluid flow will not change the temperature profile. Practically this will not be the case and an interface (inlet or outlet) block will have to be designed to cope with this problem. Interface blocks for fluid exchange, which make sure the temperature profile inside the module remains undisturbed, can also be designed independently from the other blocks. Their purpose is to heat or cool the fluid to the desired temperature when it enters or leaves the module. For each block a heating or cooling structure is designed that compensates heat loss (e.g. by convection) and produces the desired temperature profile. For this purpose, it is important to consider not only the static or stationary temperature distribution but also take the heat capacity into account that is coupled to the volume elements of the heater. Figure 2.2 shows the heat creation and flow in neighboring volume elements, only one of the four laterally linking thermal resistors and the one to the ambient are shown. If the temperature is equal inside two adjacent cells these volume elements can be treated as not coupled and show the same temperature over time function.
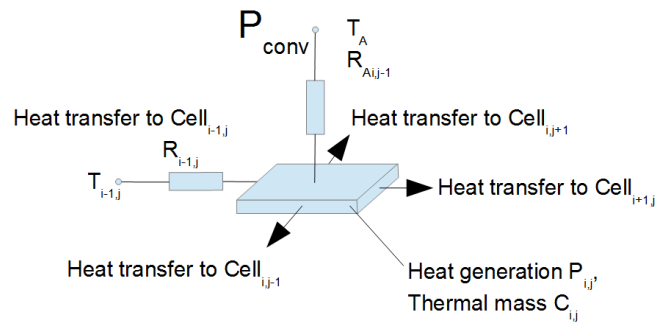


FIGURE 2.2: Heat transfer and heat generation inside cell$_{i,j}$.

## 2.2 Heater design

If a module is sufficiently thin, an important simplification can be applied successfully: the heat generation can be assigned to a 2D-section of the module. If this is not the case the heat diffusion in the out-of-plane direction is related to non-negligable temperature

differences, which could be compensated by increasing the heating power. However, in order to avoid temperature transients and overheating it is necessary to heat up the entire module slow enough. If the design requirements cannot be met with one single, centrally positioned heater layer the power must be distributed more equally by employing several heating layers.

Considering a discretized module with an equidistant grid (figure 2.1) which is independent from the FE-model and only serves the design of the heater structure, an equivalent circuit can be given for a cell$_{i,j}$ that liberates a heat $P_{i,j}$. This element has a heat capacity $C_{i,j}$ which is coupled to the heat source. Convection is modeled by a resistor $R_{Ai,j}$ that is determined by area and convection film coefficient $h$ and the ambient Temperature $T_a$. Adjacent cells are coupled through the resistances $R_{i-1,j-1}, R_{i-1,j+1}, R_{i+1,j-1}$ and $R_{i+1,j+1}$ to the correlating element temperatures $T_{i-1,j-1}, T_{i-1,j+1}, T_{i+1,j-1}$ and $T_{i+1,j+1}$. From the equivalent circuit the heat $P_{i,j}$ can now be calculated:

$$
\begin{aligned}
P_{i,j} = (T_{i-1,j-1} - T_{i,j}) \cdot \frac{1}{R_{i-1,j-1}} + (T_{i+1,j-1} - T_{i,j}) \cdot \frac{1}{R_{i+1,j-1}} \\
+ (T_{i-1,j+1} - T_{i,j}) \cdot \frac{1}{R_{i-1,j+1}} + (T_{i+1,j+1} - T_{i,j}) \cdot \frac{1}{R_{i+1,j+1}} \\
+ (T_a - T_{i,j}) \cdot \frac{1}{R_{A(i,j)}} + \frac{\mathrm{d}T_{i,j}}{\mathrm{d}t} \cdot C_{i,j}
\end{aligned}
\tag{2.1}
$$

Assuming that a flat temperature profile is achieved in the desired area, the heat flow to neighboring cells is zero leaving only convection and heat capacitance to determine the temperature of an element.

$$
P_{i,j} = (T_a - T_{i,j}) \cdot \frac{1}{R_{A(i,j)}} + \frac{\mathrm{d}T_{i,j}}{\mathrm{d}t} \cdot C_{i,j}
\tag{2.2}
$$

If the spacing $a$ of the cells with thickness $d$ is equidistant $R_{A(i,j)}$ and $C_{i,j}$ can be expressed as

$$
R_{A(i,j)} = \frac{1}{h \cdot A_{i,j}}
\tag{2.3}
$$

and

$$
C_{i,j} = C_P \cdot \varrho \cdot a^2 \cdot d
\tag{2.4}
$$

yielding

$$
P_{i,j} = (T_a - T_{i,j}) \cdot \frac{1}{h \cdot A_{i,j}} + \frac{\mathrm{d}T_{i,j}}{\mathrm{d}t} \cdot C_p \cdot \varrho \cdot a^2 \cdot d
\tag{2.5}
$$

This differential equation is of the standard type and a time constant can be expressed as

$$
\tau_{i,j} = \frac{h \cdot A_{i,j}}{C_p \cdot \varrho \cdot a^2 \cdot d}
\tag{2.6}
$$

13

The border cells in the region of the flat temperature profile will have to supply heat flux to the cells with lower temperature. If the time constants are equal for all the cells and the power dissipation matched, it is possible to heat up the whole structure to the steady state temperature distribution without a rate limit. Without the necessity for several control loops, a single reference temperature measuring point and power amplifier can be used. This makes it possible to avoid major temperature transients and to control the thermo-mechanically induced stress. In practice the heater geometry will be not a continuous area but rather some conductive track (e.g. meander) and the heat generation is not uniform across the desired areas. Therefore, it is important to estimate the temperature ripple caused by the heater geometry or create a design rule for the heater structure. Depending on the heat diffusion through the material a heating rate has to be chosen that keeps the temperature ripple in lateral direction under a given limit.

Depending on thermal conductivity and specific heat, a grid with sufficiently spatial resolution can be chosen and a mean thermal capacity per element together with a thermal resistance can be calculated. A mini heater can be placed inside each 2D-element where the trace width determines the electrical power loss. Therefore, a matched heating power distribution can be designed that compensates local heat loss. Depending on the time constant $\tau_{i,j}$ given by heat removal resistance $R_{Ai,j}$ and thermal capacitance $C_{i,j}$ it is possible to heat the module in such a way that the temperature rises proportionally in all locations to the final temperature distributions.

The quicker the heating has to be performed, the finer the 2D-grid has to be to avoid inhomogeneity in the temperature distribution. Depending on the manufacturing method, it might not be possible to achieve this goal. Thin film technology creates very homogeneous material distributions with basically no defects where as thick film technology has higher tolerances regarding lateral dimensions and thickness and also can have defects like pinholes. Small structures may be feasible to manufacture in thick film technology but the defects and tolerances create too much deviation between desired and actual heating power distribution. Figure 2.3 shows the heater array principle. The single heater structures can be connected either in series or in parallel using additional ground and supply voltage layers. In order to extract the heating power for each 2D-element an equidistant grid representation of the proposed microfluidic module has to be created so the heat removal per element can be calculated. A procedure to transfer the CAD-data to the simulation package is described in chapter together with an algorithm to reduce the amount of data for the simulation by coarsening and mesh creation. If the timing requirements are less stringent, a large structure can be designed spanning over the whole module. In such a case the properties of the structure can be modulated with

mathematical functions to optimize the temperature profile. This strategy is presented in the following chapter.
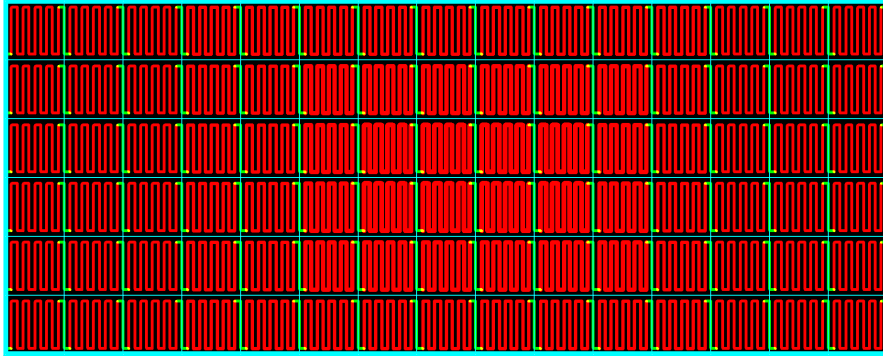


FIGURE 2.3: Proposed heater array that compensates heat losses due to convection. Red: resistor paste with varying trace width, green: conductor paste in a 2D-grid, structure connected in series for constant current operation.

## 2.3  Temperature measurement

In order to assess the temperature inside the sections, temperature sensors have to be embedded into the module. Basically three possibilities exist for an LTCC module:

a) Resistive temperature sensors

Resistive temperature measurement used in thick-film and LTCC technology can be divided into two types. A mostly linear temperature sensor with a PTC characteristic that can be expressed as $R_\mathrm{T} = R_0 \cdot (1 + (T - T_0) \cdot \alpha)$. Deviations from the ideal linear characteristics can be considered by adding higher order terms. Platinum based resinate pastes result in a very thin $(100\,\mathrm{nm})$ metal film which has a temperature coefficient of approximately $2500\,\mathrm{ppm/K}$. Resinates can only be applied on the outside of the modules in a post firing process and cannot be embedded. PTC-resistor pastes are available that are compatible with the co-firing used in LTCC and have a similar sensitivity than a platinum based resistor. A further possibility is the usage of an NTC-Paste based on Ruthenium oxide. NTC-Resistors have an exponential characteristic and exhibit a high sensitivity which is based on the following equation: $R_\mathrm{T} = R_\mathrm{N} \cdot e^{\frac{1}{T_0} - \frac{1}{T}}$. NTCs have a significantly higher sensitivity at lower temperatures and are highly nonlinear.

b) Thermocouples

The measuring principle is based on the Seebeck effect where the difference in work function manifests as a temperature dependent contact voltage. It always needs a reference contact at a defined temperature and delivers only signals in the range of several

$10\,\mu\text{V}\,\text{K}^{-1}$. However, a contact can be kept very small and, therefore, a point measurement of temperatures is possible. Thermocouples are usually built as welded wires, in the case of thick film and LTCC technology they are screen printed using two different contact pastes. However, their rather low output signals make them less attractive for the use in such a module because small resistors are easy to implement. On the other hand, thermocouples offer low resistivity and, therefore, they are less sensitive to electromagnetic interference. Moreover, they can be applied at high temperature when resistors would suffer from premature aging.

c) Capacitive temperature sensors

The measurement principle is measuring the capacitance of an electrode structure that is influenced by the geometric change (thermal expansion) and changing dielectric properties. A small sensor will have a very small capacitance and a high impedance and is therefore even less attractive than the realization of a thermocouple. Especially the behavior of the dielectric can be quite unexpected as impedance spectroscopy showed. A study on the temperature dependence of the permittivity of dielectrics has been included as section in Appendix A).

# Chapter 3

# Blood analysis subsystem - feasibility study

Based on an existing design of a blood diagnosis system, a simplified module design is derived. This design serves as a proof of concept and is first studied using finite element simulation and after optimization is realized as thick film module. The weight is placed on optimizing the thermal design rather than the function as a real blood analysis module. As pointed out in chapter 1, for enzymatic measuring methods it is of crucial importance that the temperature distribution is stable at and around the sensing elements inside the fluidic channel. Figure 3.2 shows an explosion view of the module set-up. The original inner core consists of a metal base plate that is fixed to a Peltier temperature control unit. This metal plate is coated with an inert polymer layer, which in turn carries various sensing electrodes and enzymatic sensing areas. The electrodes themselves are covered by another polymer layer; only the sensing areas are exposed to the fluid. A plastic part is clipped onto this plate employing a gasket forming a micro-channel system. For operation, a homogeneous temperature distribution is needed inside that channel and a tight temperature tolerance must be kept. Because of intellectual property of a company, further details cannot be disclosed. Instead of placing the module onto a regulated Peltier-element for heating and cooling, an integrated heater on a ceramic baseplate is designed to substitute the costly and bulky set-up. This approach eliminates the need for the large Peltier temperature-control system and combines the temperature control with the sensing functions in one ceramic module. For this purpose, a ceramic substrate made of alumina $Al_2O_3$ is used where heaters and sensors as well as the passivation layers can be applied by conventional thick film technology. Along the channel, a temperature of $37\pm0.25\,°C$ must be guaranteed. Inside the channel, the temperature of a $100\,µm$ thick fluid layer above the sensors is critical for reproducible measurement results. The steady state final temperature distribution

should be reached 15 s after power-up or after the exchange of the fluid sample. The design process is schematically outlined in figure 3.1, the fixed dimensions and material data for all simulations is summarized in table 3.1.
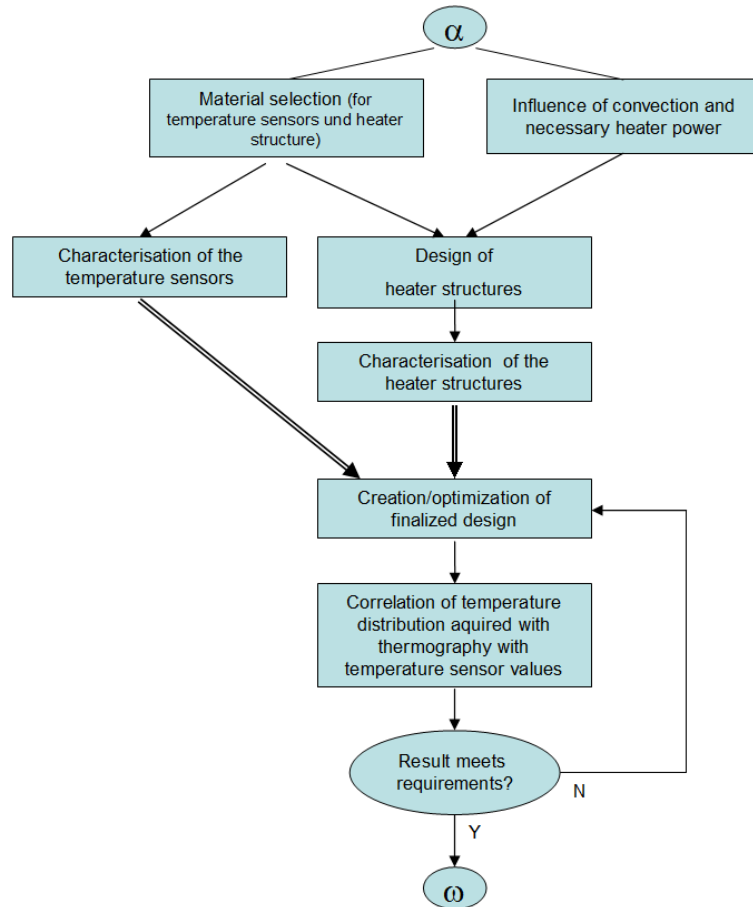


FIGURE 3.1: Design workflow of sensor module.
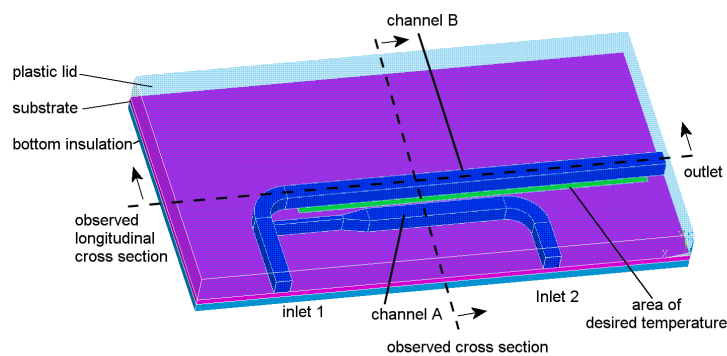


FIGURE 3.2: Simplified model build up.

## 3.1 Preliminary investigations for the feasibility study

In order to create a homogeneous temperature distribution inside the fluid at the desired locations it is first necessary to check the influence of the boundary conditions like module placement inside the housing and resulting convection. Furthermore, it is crucial to check from the very start if the module geometry allows it to reach the goals with a single heater underneath the fluid channel or if further measures must be taken (e.g. multiple regulated heated zones). Based on an estimation of heat loss (coarse simulation) it is possible to obtain the maximum stationary heating power the heating resistor must be designed for. The dynamic behavior must also be taken into account not only for the power up but also for the fluid exchange, as these are different scenarios. Fur future mobile use the heating power applied should be just high enough to heat up the unit in the specified time and use as little as possible continuous heating to keep the temperature stable.

### 3.1.1 Heat loss and temperature distribution with constant temperature boundary condition

In order to obtain basic information about the feasibility of the approach in a static case (the fluid is resting, as the module has been pre-filled) fluid a finite element analysis is carried out and the heat losses through convection is calculated. For this purpose, the model is reduced to a simple geometry consisting of the ceramic substrate and plastic cover connected to it. Any conductor traces are not yet considered (see figure 3.2). For the calculation the area underneath the channel where the constant temperature must be obtained is simply set to $T_S = 37\,°\mathrm{C}$ and the ambient temperature is assumed to be $T_U = 22\,°\mathrm{C}$. On the bottom side of the substrate, an insulation of plastic is weakening the effect of the natural convection the module is exposed to.

### 3.1.2 Calculation of necessary heating power

For investigation of the influence of varying convection, two cases were modeled: Case a: The convection film coefficient h is varied from 1 to $30\,\mathrm{W/m^2K}$ and the total dissipated heat is calculated. The thickness of the bottom insulation is held constant $d_i = 1\,\mathrm{mm}$. Case b: The convection film coefficient h is assumed to be constant ($10\,\mathrm{W/m^2K}$) and thickness of the bottom insulation $d_i$ is varied. The total heat flow out of the model is again calculated. The simulation parameters for this study are summarized in table 3.2, the material parameters are listed in table 3.1. The calculated heat flux which is removed through the outer surface (=necessary heating power) is as expected highly

| Component | Material | Dimensions | | | thermal conductivity $Wm^{-1}K^{-1}$ | spec. heat capacity $Jkg^{-1}K^{-1}$ | spec. resistivity $\Omega m$ | density $kgm^{-3}$ |
|---|---|---|---|---|---|---|---|---|
| | | length mm | width mm | thickness mm | | | | |
| sensor substrate | $Al_2O_3$ | 49.5 | 26.5 | 1 | 24 | 850 | n.a. | 3900 |
| plastic lid | PMMA | 49.5 | 26.5 | 3 | 0.19 | 1470 | n.a. | 1190 |
| bottom insulation | PMMA | 49.5 | 26.5 | 1 | 0.19 | 1470 | n.a. | 1190 |
| interconnects, heat spreader, contacts | Ag | from CAD data | | $12 \cdot 10^{-3}$ | 429 | 232 | $1{,}6129 \cdot 10^{-8}$ | 10490 |
| heater | Paste ESL29230 | — | — | $12 \cdot 10^{-3}$ | 100 | 450 | $2.4 \cdot 10^{-6}$ | 8400 |
| temperature sensor | Paste PTC2611 | — | — | $12 \cdot 10^{-3}$ | 100 | 450 | $1.2 \cdot 10^{-4}$ | 8400 |
| fluid in channel | $H_2O$ | — | 1.6 | 1.6 | 0.597 | 4187 | n.a. | 1000 |

TABLE 3.1: Component geometry and material properties.

| Boundary condition | symbol | value |
|---|---|---|
| Ambient temperature | $T_U$ | 22 °C |
| Substrate temperature | $T_S$ | $T_S$=37 °C |
| thickness of bottom insulation | $d_i$ | 1 mm or variable |
| convection film coefficient | h | 10 W/m²K or variable |

TABLE 3.2: Boundary conditions and parameters for FE-analysis.
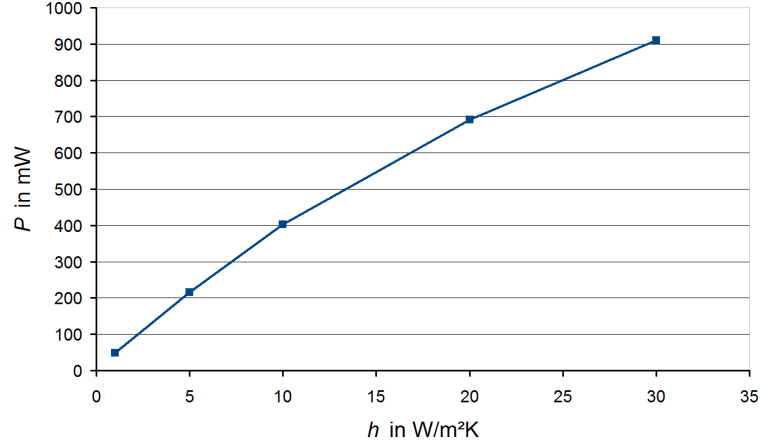


FIGURE 3.3: Dissipated heat with variable convection and fixed insulation thickness $d_i$=1 mm (case A).
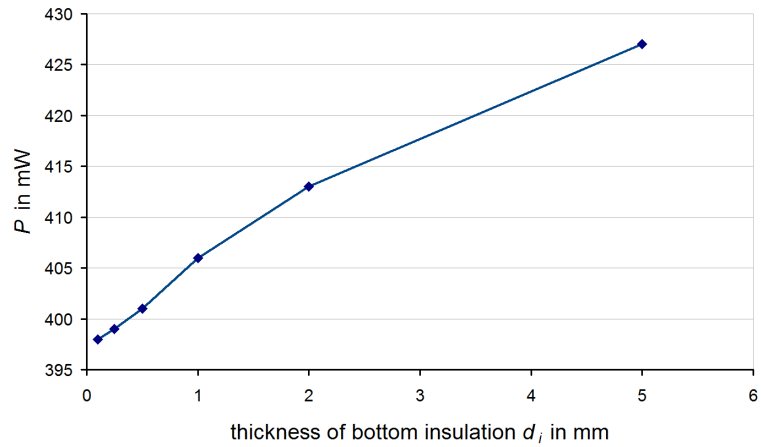


FIGURE 3.4: Dissipated heat with constant convection h=10 W/m²K and variable insulation thickness $d_i$ (case B).

dependent on the convection (figure 3.3). This means that the resulting temperature distribution of the module is mainly (figure 3.5) determined by the thermal contact resistances due to mounting inside the housing and the convection acting on the module inside it. For still air and free convection a convection film coefficient of $h$=10 W/m²K is assumed. An insulation on the bottom side will have the same effect like the reduction of the convection coefficient but does not play such a great role as can be seen in figure 3.4.
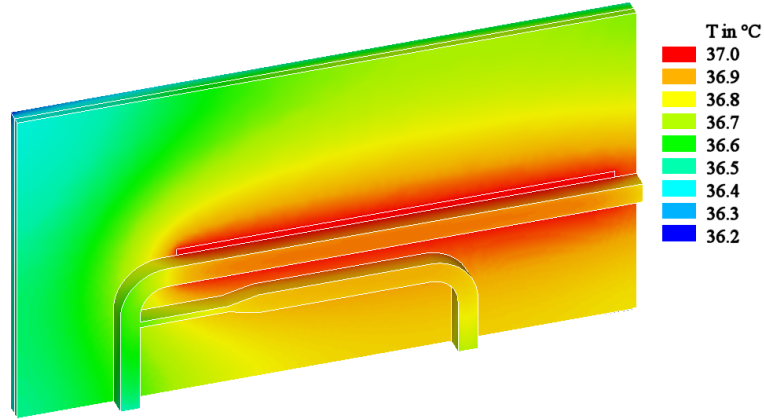
FIGURE 3.5: Temperature distribution on substrate and fluid with constant convection h $= 10\,\mathrm{W/m^2K}$ and variable insulation thickness d$_i = 1\,\mathrm{mm}$ (plastic part not shown).

### 3.1.3 Homogeneity of temperature profile inside channel

The sensor principle requires that the temperature difference inside the fluid within a 100 µm thick layer above the sensors must not exceed 0.5 K. For the temperature distribution the results from case A with a convection film coefficient 10 W/m²K) and a bottom insulation thickness of $d_i = 1$mm were selected. Figure 3.2 shows the location of the planes where the cross sections (figure 3.6 and 3.7) were obtained. A significant temperature gradient exists vertically inside the fluid channel but is sufficiently small (for the detailed view see figure 3.8). This gradient is caused by the heat loss through convection over the outer surface of the plastic lid. However, the temperature variation along the channel is extremely small <0.1 K while the temperature difference between the two parallel channel sections is 0.5 K. This shows that an appropriate regulated input-power is needed to compensate for slight changes in convective thermal losses as well as a properly designed heating power distribution to optimize the temperature profile inside the channel and across the substrate. The following conclusions are drawn: The
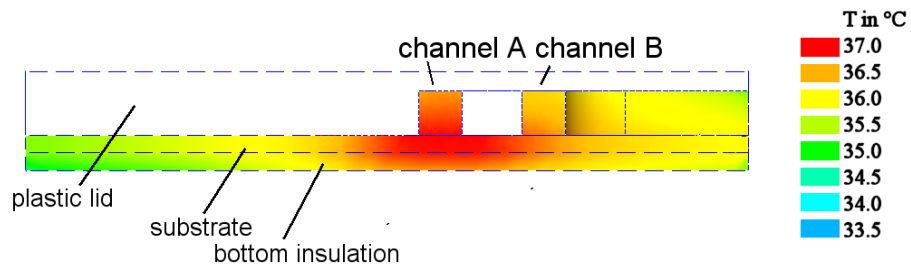


FIGURE 3.6: Temperature distribution of cross section inside channel.

temperature gradient that occurs along the vertical axis inside the channel is sufficiently small 1 K/mm) and allows constructing a module with heaters in only one plane without the use of additional insulation measures. If the heating zones are significantly larger than the channel, the plastic lid is also heated over a greater area reducing the heat flow

22
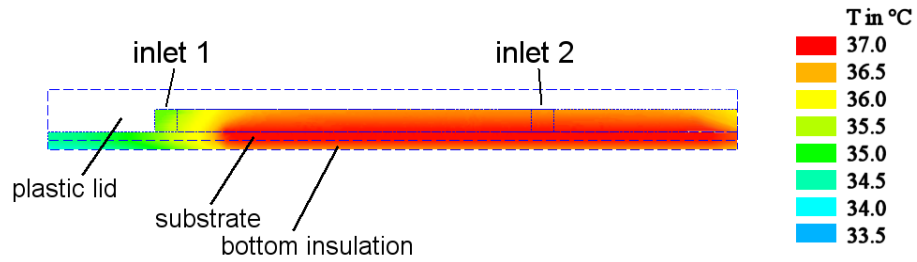
FIGURE 3.7: Temperature distribution of longitudinal cross section inside channel.
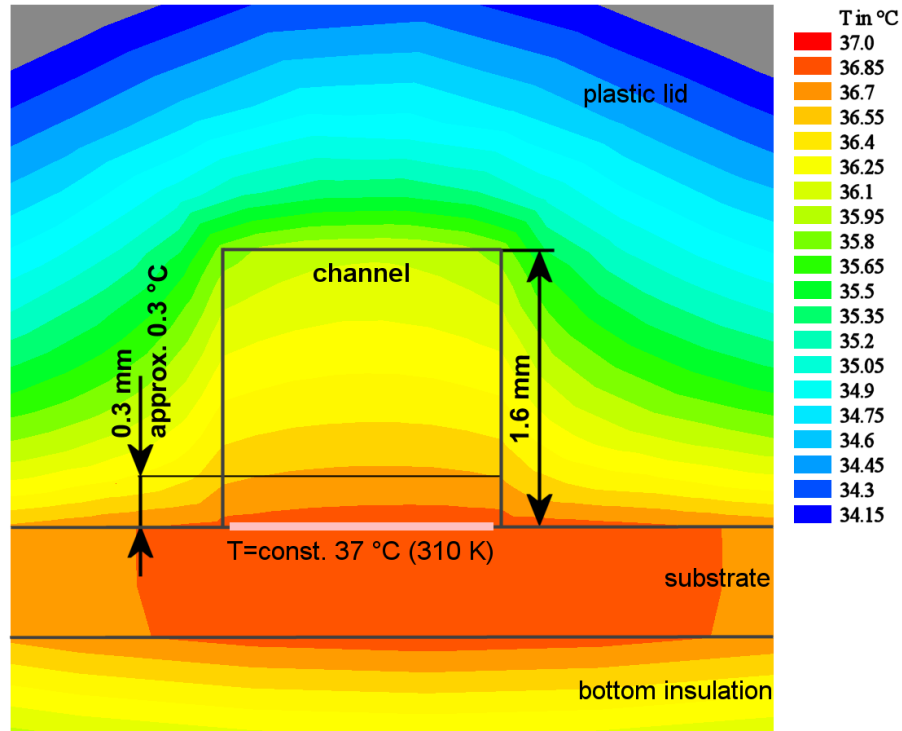


FIGURE 3.8: Detailed view of temperature distribution inside channel.

out of the channel into the surrounding material. This, in turn, helps further reducing the gradient inside the channel.

### 3.1.4 Material selection for manufacturing

For the realization of the sensor module, standard thick film technology materials were considered. As substrate a $1\,\mathrm{mm}$ thick 96% $Al_2O_3$ ceramic was chosen, which is the most common substrate material and was supplied pre-cut to the desired geometry by a company. This material allows the application of a wide range of thick film pastes optimized for this substrate type. For temperature measurement, the PTC2611 resistive paste was selected that is used for precise temperature sensing resistors. For the heater structure, a cost effective heater paste ESL29230 was selected which can be used where

high power dissipation densities occur. For the interconnects, the frequently used solderable AgPd-paste ESL9695 was employed. As passivation layers the low sintering glass past ESL4771 as well as the polymer paste ESL245SB were used. The latter offers a cost advantage compared to the glass paste and does not influence the resistors because it is cured at 120 °C. It can be expected that the glass paste is sufficiently bio-compatible and inert to the liquid whereas no information is available regarding the polymer paste. Compatibility between the materials has to be evaluated first as a mutual influence of conductor paste and passivation is expected.

## 3.2 Evaluation of the temperature homogeneity created by heating structures

This section discusses aspects and progress of the design of a heating structure that allows forming a homogeneous temperature distribution. At first, several distributed rectangular heating zones were used to check if this undertaking is possible at all. A heated band structure was derived from these results and the stationary and dynamic quality of the temperature distribution is studied. Further improved structures (fence- and meander structure) were characterized and finally the meander chosen as best solution for the targeted application. Later verification samples of fence and meander structures were built and characterized to validate the simulation results.

### 3.2.1 Distributed evenly heated zones

Based on the studies in the previous section a design was derived where several heating zones are located on both sides of the fluidic channel. These heating zones surrounding the channel will compensate for vertical heat loss due to convection and also compensate the lateral heat flow inside the substrate which, in turn, will hopefully help stabilizing a homogeneous temperature profile inside the channel. For further improvement of the temperature profile, a well thermally conducting silver stripe is located directly underneath the fluid. The proposed layout can be seen in figure 3.9, the sizes of the zones are listed in table 3.3, the boundary conditions are the same as in previous simulations (table 3.2. The results show a good homogeneity of the temperature distribution in the relevant areas (figure 3.10). In the cross sectional view in figure 3.11 a reduced vertical temperature gradient can be observed compared to figure 3.8. The reason lies in the bigger heated area that also compensates the heat flow out of the fluid into the surrounding material of the plastic lid in a better way. The total heating power comprised of the contributions from the single zones (216 mW+78 mW+91 mW+62.5 mW=447.5 mW) shows

| Component | Dimensions | | | Power |
|---|---|---|---|---|
| | Length mm | Width mm | Thickness μm | W |
| silver heat spreader | 30 | 2 | 12 | — |
| heating zone 1 | 42 | 2 | 12 | 0.216 |
| heating zone 2 | 15 | 2 | 12 | 0.078 |
| heating zone 3 | 21 | 2 | 12 | 0.091 |
| heating zone 4 | 10 | 2 | 12 | 0.0624 |

TABLE 3.3: Component geometry, material properties and operating parameters.

a good match with the predictions from the previous section where the dissipated heat has been calculated for constant temperature regions on the substrate (figures 3.3 and 3.4) that is now the required heating power.
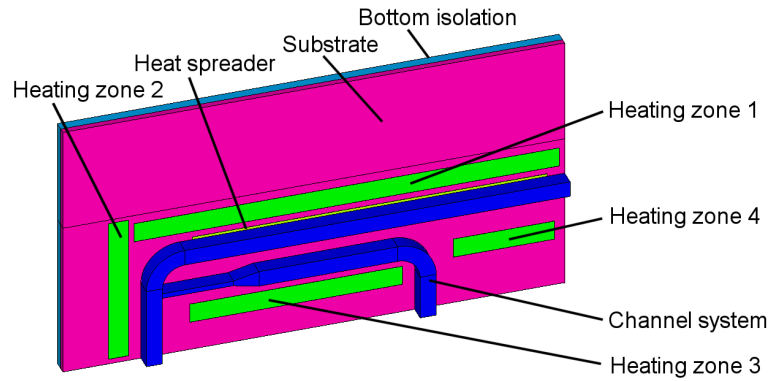


FIGURE 3.9: Model with 4 heating zones and a silver layer heat spreader(plastic lid not shown).
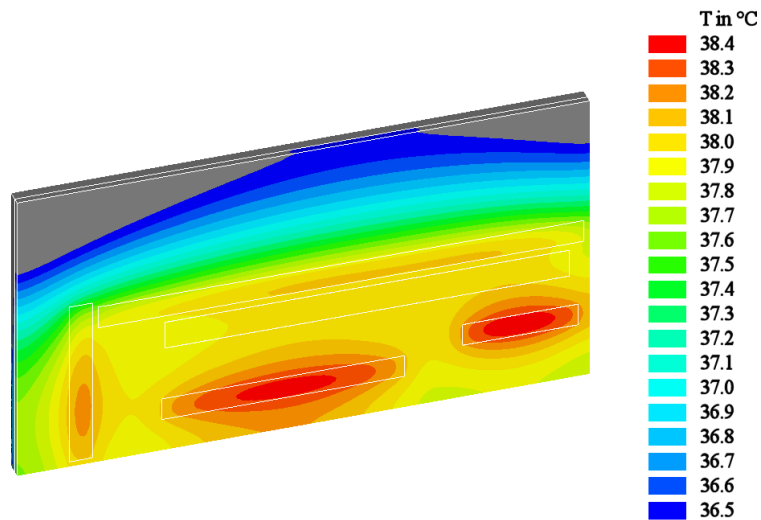


FIGURE 3.10: Temperature distribution when using 4 heating zones (plastic lid not shown).

25
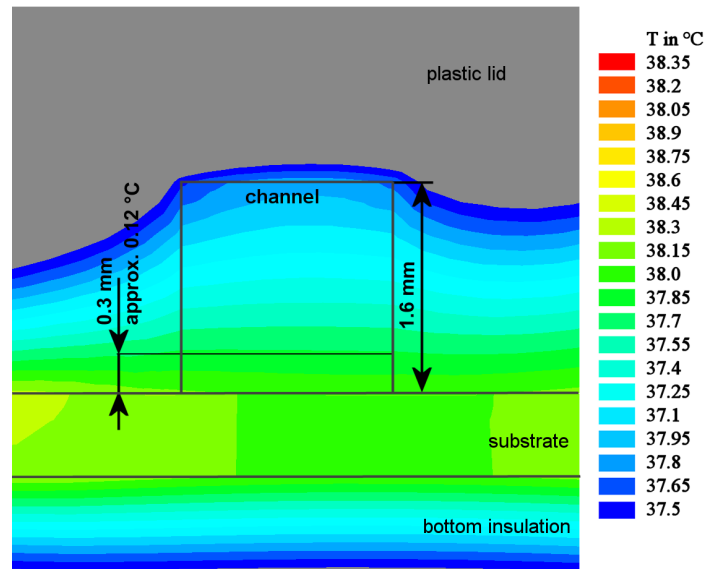
FIGURE 3.11: Detailed view of the temperature distribution in the channel cross-section when using 4 heating zones.

### 3.2.2 Heated band structure

The separate heating zones are now combined into a heated band structure (figure 3.12) and further modifications are performed:

- The heating zones are adjusted to the shape of the fluidic channel and are electrically connected in series by a silver track, which is 12 µm thick and also forms the contacts for external supply.

- The silver heat spreader does not improve results and is therefore removed.

- The sensor connections are now taken into account and are modeled as 12 µm thick silver tracks.

- Because the sensor module will be mounted inside a housing, the bottom insulation is no longer needed and also removed.

- The plastic lid that is forming the fluid channel is reduced in size so that the contact pads are accessible.

The boundary conditions are summarized in table 3.4. The temperature distribution shows a satisfactory flat profile which is shown in figure 3.13.

| Boundary condition | symbol | value |
|---|---|---|
| Ambient temperature | $T_U$ | 22 °C |
| convection film coefficient | h | 10 W/m$^2$K or variable |
| Heater voltage | | |
| static operation | $U_{Heater}$ | 2.1 V to reach desired temperature at reference point |
| control loop operation | $U_{Supply}$ | 12 V as controller supply voltage |

TABLE 3.4: Boundary conditions and parameters for FE-analysis.
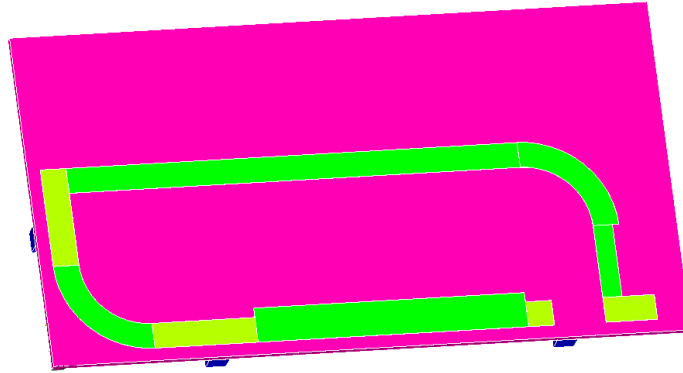


FIGURE 3.12: View of heater sections (green) and interconnects (yellow) of heated band structure.
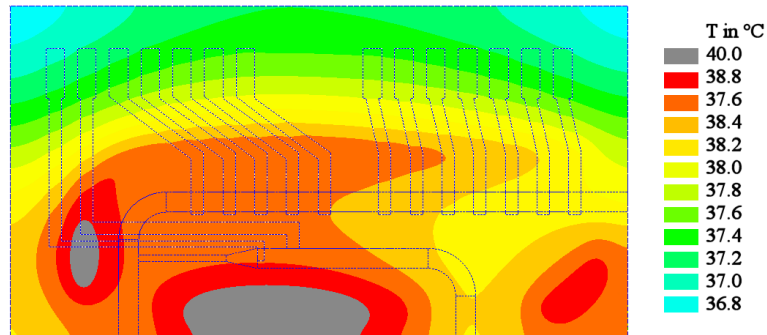


FIGURE 3.13: Temperature distribution on top side of substrate of heated band structure.

**Power-on step response of the module**

This simulation is performed to extract the characteristic values for controller optimization. When operating the heater at a static voltage level of $U_{Heater}$=2.1 V the temperature at the measuring point reaches the desired value of 37 °C see figure 3.13. The step response is depicted in figure 3.14. The system shows PT1Td behavior with a time constant $\tau_1 = 270$ s and a delay time of $\tau_d < 1$ s.
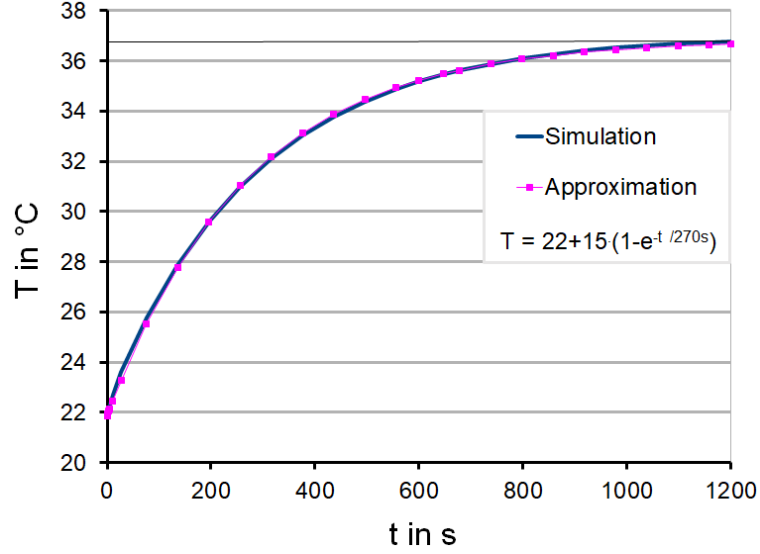
FIGURE 3.14: Step response of the heated band structure with $U_{Heater} = 2.1\,\text{V}$.

**Closed loop operation**

The PI-control algorithm was chosen and realized by means of an ANSYS-script using $100\,\text{ms}$ time steps. This time-stepping defines moments where the temperature at the reference point is evaluated, a new supply voltage is computed and the boundary conditions set accordingly. The optimal controller parameters were chosen after Chien, Hrones und Reswick[26] and were calculated with following equations:

$$K_s = \frac{T_{step}}{U_{step}}, \ K_P = 0.34\frac{\tau_1}{K_s}, \ \tau_I = 1.2\tau_1$$

$T_{step}$ is the temperature step between start and stationary value, $U_{step}$ is the voltage accordingly, $\tau_1$ is the major time constant and $K_s$ is the proportional value of the unregulated system. The PI-controller parameters are calculated to be $K_P = 8.9$ for the proportional part and $\tau_I = 324\,\text{s}$ integral part for closed loop operation. Although the controller is able to regulate the desired temperature at the reference point within only $7\,\text{s}$ (see figure 3.15 and figure 3.16), it takes over $30\,\text{s}$ for the temperature distribution to settle in the entire module (figure 3.17). This shows that a single control loop with only one temperature sensor can only be used with restrictions to stabilize the overall temperature profile. In order to heat the whole volume up to the desired temperature in a minimum amount of time, it is necessary to couple the majority of the heat capacity to the heater. Therefore, this approach using multiple heated zones was discarded from further investigation.
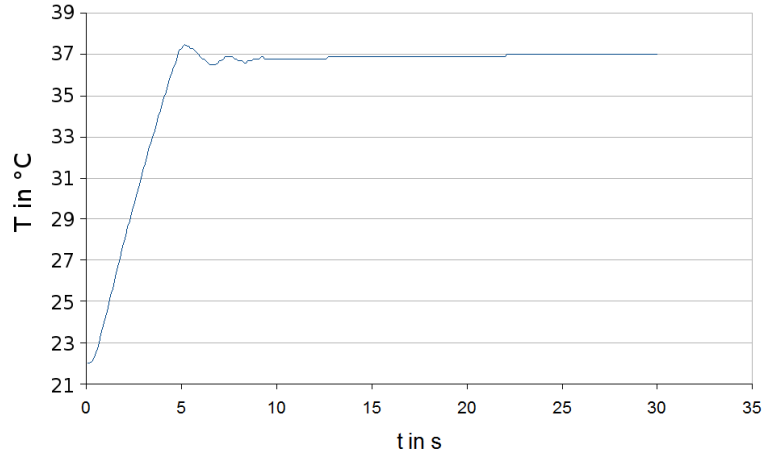
FIGURE 3.15: Step response of the controller loop of the heated band structure.

### 3.2.3 Fence-structure with variable geometry parameters

The aim is to design a heater structure that allows rapidly achieving the desired stable temperature distribution over the whole substrate without further drifts after the desired temperature has been reached at the reference point. For the first design a fence structure has been chosen where parameters like trace width, distance and overall dimensions can be arbitrarily chosen and the temperature profile adjusted accordingly while still maintaining easy implementation of the parallel connected heating strips in the FEM-software (see figure 3.18). Figure 3.19a shows the temperature distribution on a simple design for a fence-structure (32 spokes with width $b_s = 0.5\,\text{mm}$) on a rectangular substrate (size $26.5 \times 49.5\,\text{mm}^2$, thickness $1\,\text{mm}$). With this design, an elliptical static temperature maximum is obtained with a heater voltage $U_{Heater}$ of $0.5\,\text{V}$. To improve the result several geometry parameters can be adjusted:

- Total width and height of the heater structure

- Width or height modulation of the whole structure

- Number of spokes

- Density of the spokes

- Modulation of the spoke width

By sinusoidal modulation of the spoke width of the heater structure (narrow spokes in the middle with higher resistance and therefore lower localized heating power), the resulting temperature maxima occur at the outer regions of the heater structure. The resistance modulation can be easily composed of mathematical functions to optimize the temperature distribution in the critical regions. In the first step, the original structure

29
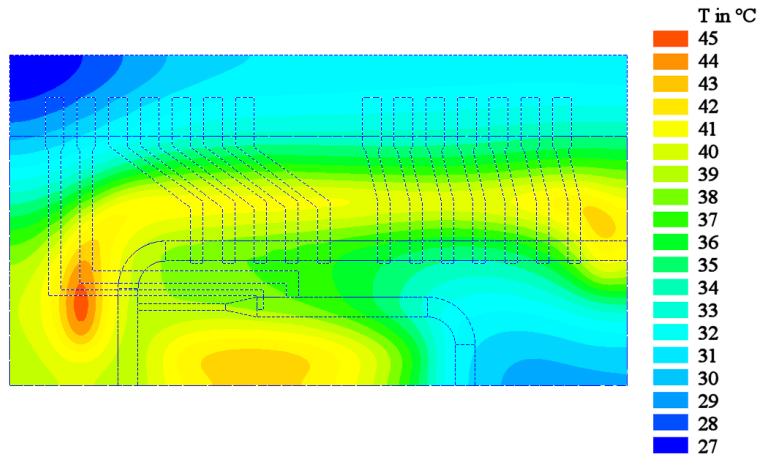
FIGURE 3.16: Temperature distribution on substrate surface after t = 7s.
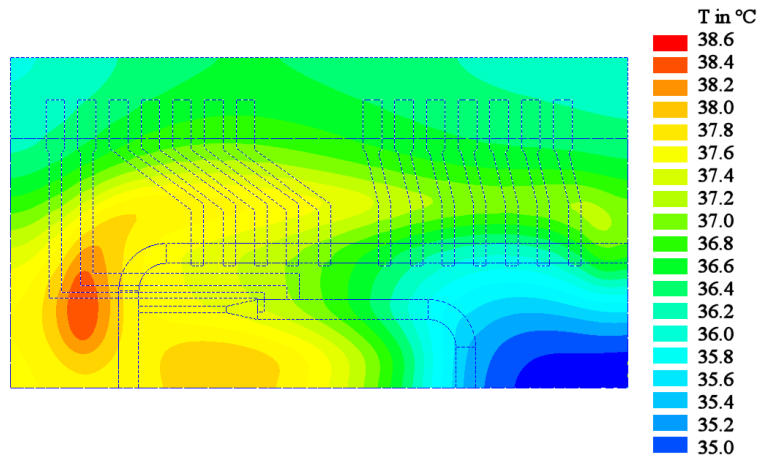


FIGURE 3.17: Temperature distribution on substrate surface after t = 30s.
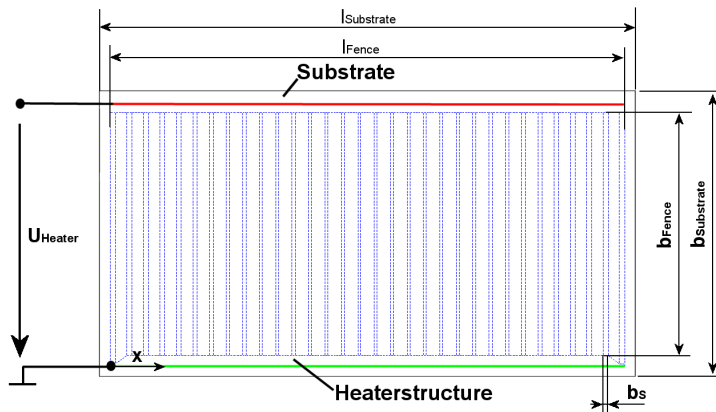


FIGURE 3.18: Simplified model for study of the spoke width modulation.

(a) $b_s = 0.5$ mm

(b) $b_s = 0.5mm \cdot (1 + 0.5 \cdot sin(t))$

(c) $b_s = 0.25mm \cdot (1 + 0.5 \cdot sin(t))$

(d) $b_s = 0.25mm \cdot (1 + 0.3sin(t) + 0.05 \cdot sin(3x))$
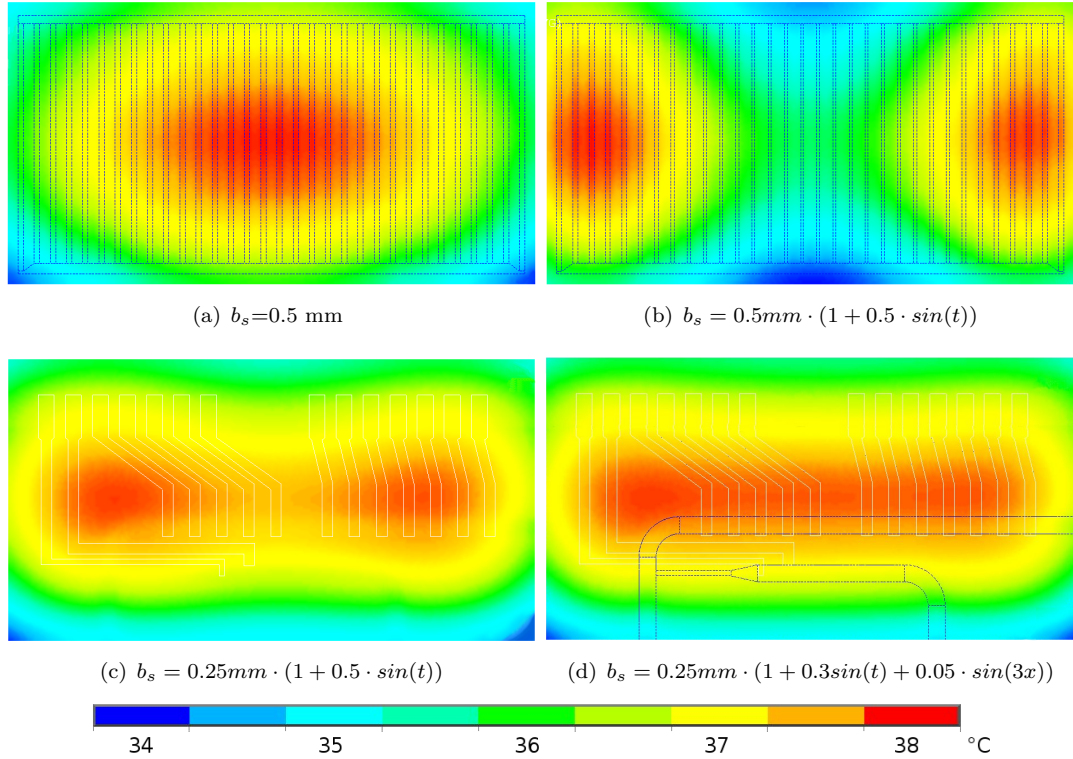
FIGURE 3.19: Temperature distribution of the fence-structure with spoke width $b_s$ modulated by a mathematical function.
a) and b) on bare substrate, c) and d) inside module.

is changed by modulating the spoke width according to $b_s = 0.5\,mm \cdot (1 + 0.5 \cdot sin(t))$ with $t = 1 \cdot x/l_{fence}$. The resulting temperature distribution is shown in figure 3.19b. By using more terms in the above expression further optimization of the temperature distribution is easily possible (figure 3.19c and d) and after reducing the size of the heater structure the layout can be included in the original design (figure 3.23) to obtain a homogeneous temperature distribution inside the channel. Based on these results an optimized design is created (figure 3.20), the proposed layout is shown in figure 3.21. The boundary conditions and operating parameters are summarized in table 3.5.
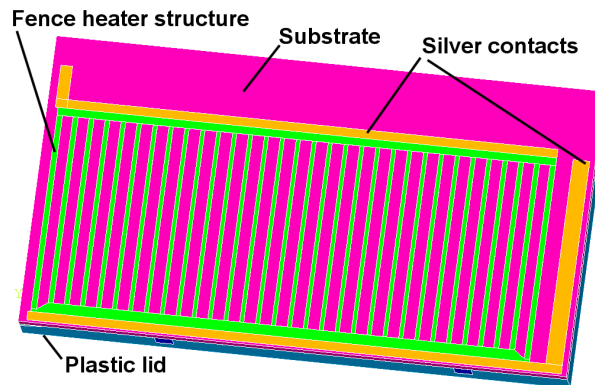


FIGURE 3.20: Model with optimized fence heater structure.

31
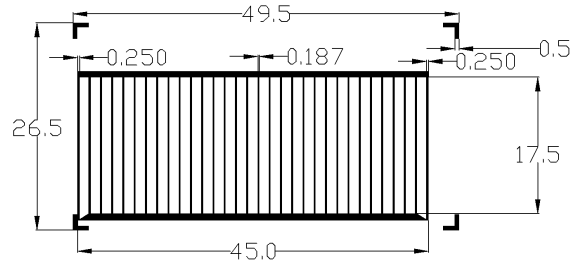
FIGURE 3.21: Dimensions of the optimized fence heater structure.

**Power-on step response of the module**

The same strategy to obtain the characteristic value for the PI-controller optimization was followed like the heated band structure. The fence structure requires a substantially lower heater voltage of $U_{Heater} = 0.546$ V to reach the desired temperature distribution due to significantly lower resistance (see figure 3.23). The step response at the reference point is shown in figure 3.22 which shows the same PT1Td behavior with a slightly larger time constant $\tau_1 = 290$ s compared to the 270 s and a negligible delay time $\tau_d < 1$ s.

**Closed loop operation**

The same control algorithm (PI-controller) was used with the same 0.1 s time steps. The controller parameters were calculated with the same equations that were used for the heated band structure: $K_P = 2.8$, $\tau_I = 348$ s. Due to the much lower operating voltage, the proportional term is higher and the integration time constant is 20% larger.

**Summary for the fence structure**

The simulation results are very promising as the desired temperature distribution can be reached very quickly. Nonetheless, several drawbacks can be recognized: In order not to obtain a too low electrical resistance, it is necessary to choose a minimum trace width

| Boundary condition | Symbol | Value |
|---|---|---|
| Ambient temperature | $T_U$ | 22 °C |
| Convection film coefficient | h | 10 W/m²K |
| Heater voltage | $U_{Heater}$ | 0.546 V to reach the desired temperature in steady state, 2.5 V as controller maximum output voltage. |

TABLE 3.5: Boundary condition for the fence-structure simulation.
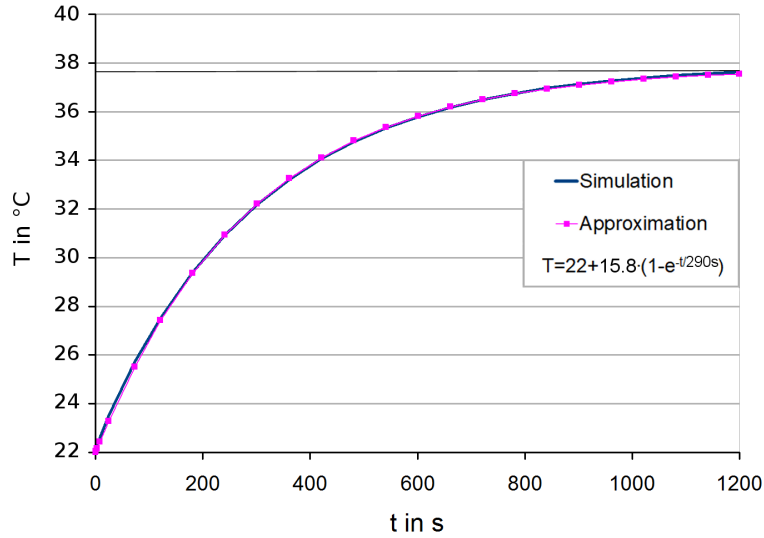
FIGURE 3.22: Temperature step response of fence-structure.
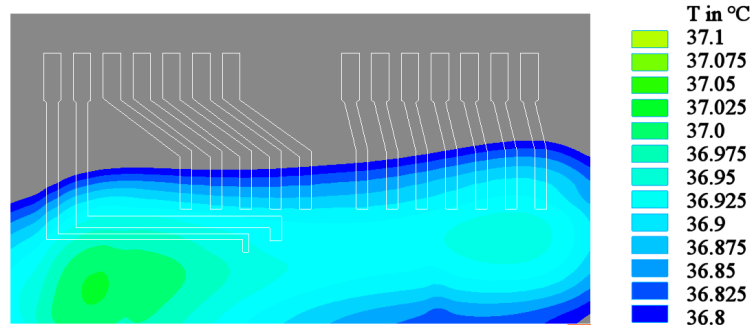


FIGURE 3.23: Steady state temperature distribution of fence-structure with $U_{Heater}$=0.546V.

of 180 µm which can be considered within technical limits of the printing process. The problem lies in variations of the geometry caused by the printing process that cause over-proportional changes in temperature distribution. Although very thin conductors are used an overall resistance of less than $1\,\Omega$ is achieved which leads to increased influence of the silver contact areas and connection lines. The fence structure could prove as problematic during manufacturing and is treated with less priority - by using a high resistance paste and for future projects, it could still be interesting for some purpose.

### 3.2.4 Meander structure with varying geometric parameters

In this part of the study, two different variants of meander structures were considered while modulating their geometry parameters. When designing heating resistors it is important to keep in mind that a limited supply voltage - in this case $12\,\mathrm{V}$ - is available. This limits the maximum heating power that can be liberated with a certain resistor value that is determined by the number of loops and track thickness and width. The number of loops are important for homogeneity of the temperature profile because a

33
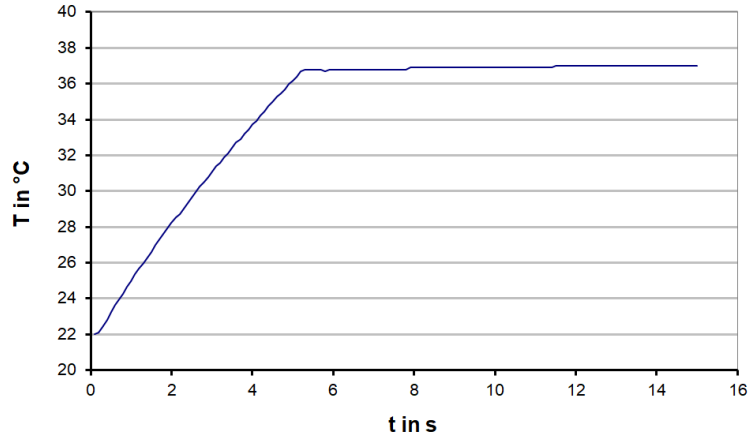
FIGURE 3.24: Step response of the controller loop of fence structure.

low number of loops leads to a high temperature ripple. For further investigations the meander structure as in figure 3.25 was chosen where a good temperature distribution is reached after adjusting geometry parameters. The geometry and material parameters as well as the boundary conditions are summarized in table 3.6, the proposed layout is shown in figure 3.26. The applied conductor track adds an anisotropic thermal conductivity to the substrate. A 90 degree rotated meander structure proofed to be detrimental to the goal of having a flat temperature profile due to increased thermal conductivity in the wrong direction as depicted in figures 3.27 and 3.28.
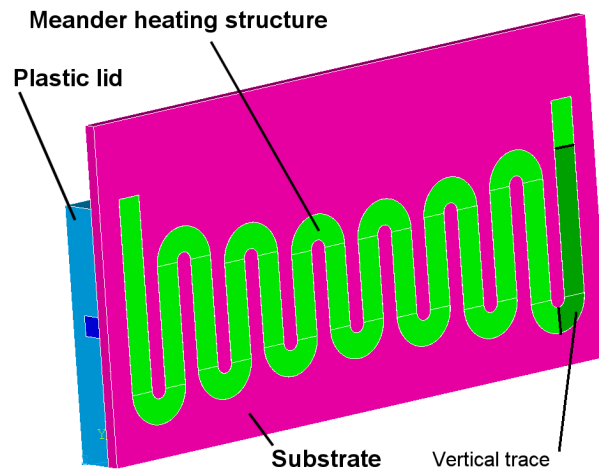


FIGURE 3.25: meander heating structure with 14 vertical traces.

**Power-on step response of the module**

The meander requires a heater voltage $U_{Heater}$=3.05 V to reach the desired temperature distribution in the sensing areas with a desired value of 37 °C (see figure 3.30). The step response at the reference point is shown in figure 3.29 which shows the expected

34
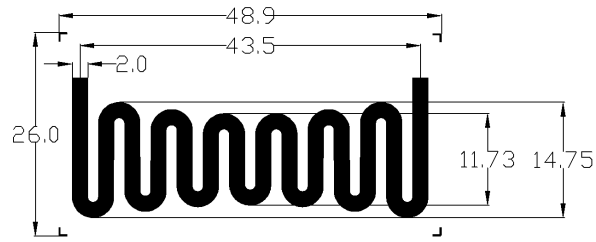
FIGURE 3.26: Dimensions of the optimized meander heater structure.
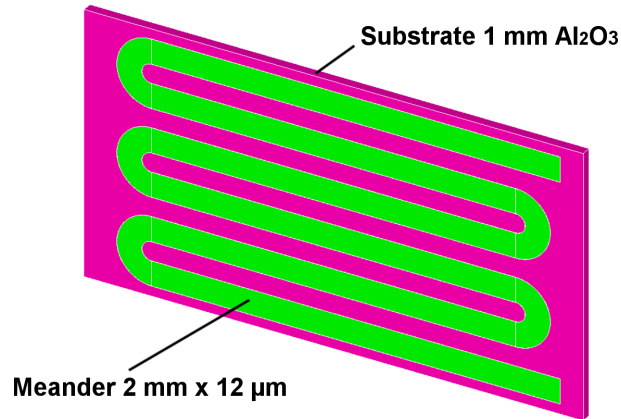


FIGURE 3.27: Model of a 90 degree rotated meander structure.
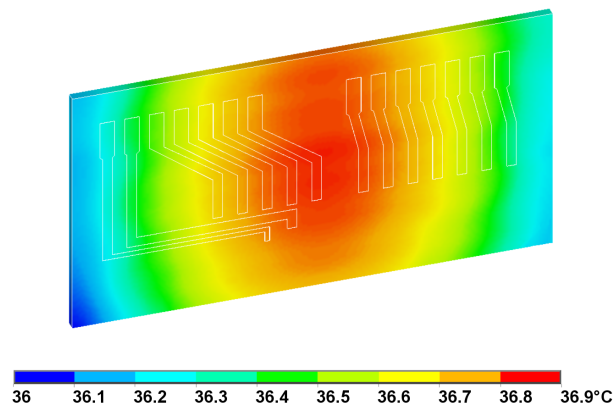


FIGURE 3.28: Temperature distribution of a 90 degree rotated meander structure.

PT1Td behavior with a time constant $\tau_1 = 280\,s$ and again a negligible delay time $\tau_d < 1s$. These values are close to the time constants of the other two structures. The temperature profile is perfectly flat in the desired areas as can be seen in figure 3.30.

**Closed loop operation**

The PI-control algorithm was applied again with the calculated parameters: $K_P = 17.9$, $\tau_I = 336\,s$, the maximum operating voltage is limited to 12 V. The proportional factor $K_P$ is twice the value that has been determined for the fence structure while the integrator

| Boundary condition | Symbol | Value |
|---|---|---|
| Ambient temperature | $T_U$ | 22 °C |
| Convection film coefficient | h | 10 W/m²K |
| Heater voltage | $U_{Heater}$ | 3.05 V to reach the desired temperature in steady state, 12 V as controller maximum output voltage. |

TABLE 3.6: Boundary condition for the meander-structure simulation.

time constant $\tau_I$ is 4.5% smaller. Figure 3.30 shows the power-on step response for the closed loop operation.

### 3.2.5 Dynamic behavior (Power-on and fluid exchange)

In a further simulation, the settling time of the control loop was determined at power-on and after fluid exchange. For temperature control a PI-controller with the parameters $K_P = 17.9$ and $\tau_I = 336\,s$ was used that allowed the pre-filled channel to be heated to the desired temperature within 11 s without overshoot (see figure 3.32). At the time of 20 s a pressure of 0.2 bar is applied for 3 s which causes fluid exchange (figure 3.33top shows the temperature distribution at t = 20 s before fluid exchange).The maximum flow velocity occurs in the middle of the channel and reaches a magnitude of 56 mm s$^{-1}$. After fluid exchange (see figure 3.33 middle) a homogeneous temperature profile is obtained within 14 s (t = 37 s) which is shown in figure 3.33 bottom. While the temperature at the reference point shows only minor fluctuations (blue curve), the drive voltage output by the controller shows a significant response and a damped oscillation as the temperature settles(orange curve). The device is capable of achieving the desired stable temperature distribution after 14 s, both after power-on and fluid exchange and thus meets the requirements for measurement. However, after fluid exchange and settling of the temperature distribution still an asymmetry is observable. A possible improvement would be the use of a flow-through heater to prevent the incoming fluid from altering the temperature distribution to a large extent.

## 3.3 Manufacturing of samples, characterization and aging

Based on the results of the simulations two types of heater structures (fence in figure 3.34 and meander in figure 3.36) were manufactured and verified. The meander structure was evaluated with an early design that was further improved during and after verification of the heater paste. In order to obtain statistical characteristics of the heating elements,
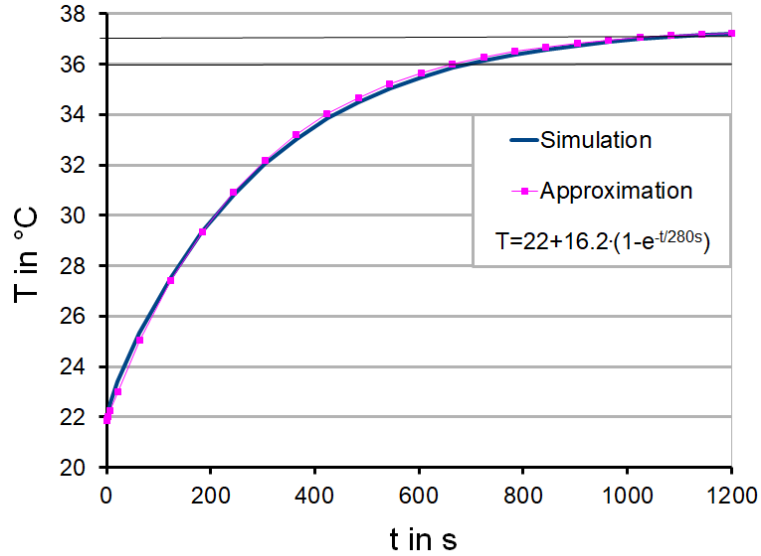
FIGURE 3.29: Temperature step response of the meander-structure.
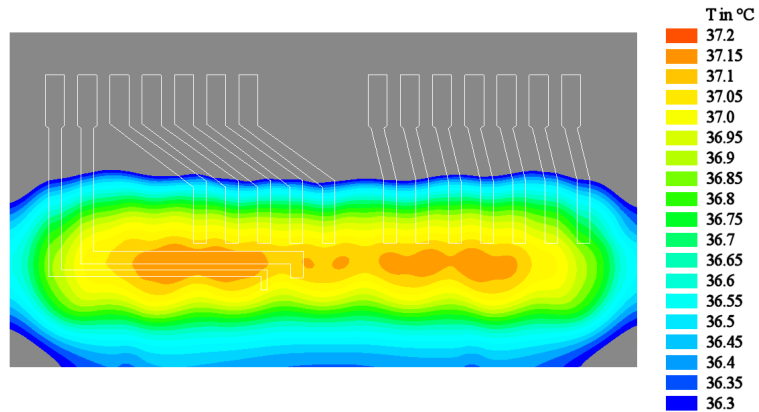


FIGURE 3.30: Steady state temperature distribution of the meander-structure with $U_{Heater}$=3.05 V.

30 samples of each type (meander and fence) were manufactured at first without passivation (figure 3.37). After the first characterization of the resistors (heater and sensors), a glass passivation layer was applied by screen printing and sintering with the manufacturing parameters shown in table 3.8 which were also used for the demonstrators later.

For the characterization of the samples, the same setup as for the characterization of the temperature sensors was used. The samples were fixed to the Peltier-temperature control system (figure 3.38 and 3.39 developed by Michael Weilguni [**?** ] which provides a flat temperature profile on top and bottom side of the sample (figure 3.40. Exchangeable probe adapters make it possible to efficiently test different sample and electrode geometries. The samples were measured using the 4-wire (Kelvin) method employing a Keithley 2000 high resolution multimeter. For the measurement those five samples were
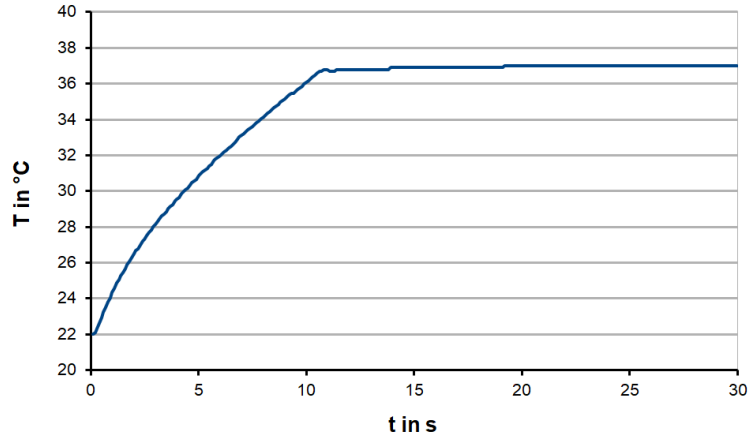
FIGURE 3.31: Step response of the controller loop.
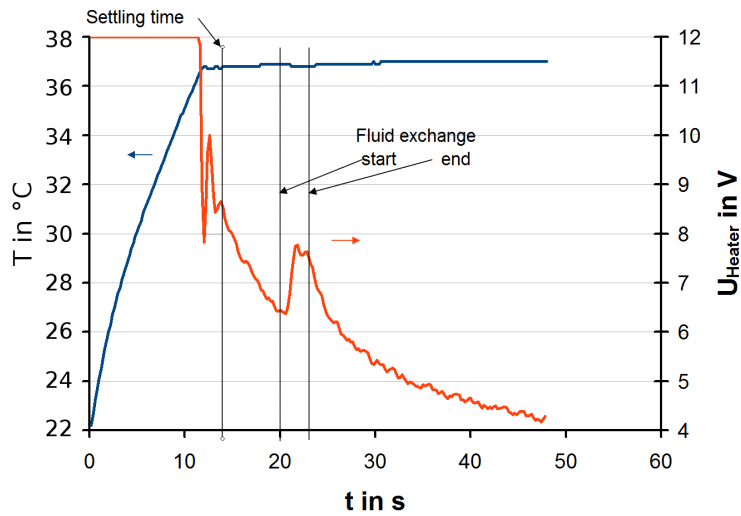


FIGURE 3.32: Temperature versus time function (blue curve) and temporal heater voltage function (red curve) during power on and fluid exchange cycle in closed loop control.

chosen that showed resistance values equally distributed over the total resistance range. This allows checking of correlations between resistance variations and temperature coefficient of resistivity. After this characterization, the samples were further coated with a glass passivation layer and characterized again. This was followed by aging at 300 °C for 300 h and another characterization. The differences indicate the long-term stability of the resistors. Table 3.7 shows resistance values and temperature coefficient of the samples after manufacturing, aging and application of the glass passivation layer. The temperature dependence of the resistance is shown in normalized diagrams in figure 3.42a after manufacturing, in figure 3.42b after application of the passivation layer and in figure 3.42c after 300 h aging. The statistical distributions are shown in figure 3.41.

The variation in resistance of the samples lies in the expected range of ±15% with this technology. The application of the glass passivation layer causes a significant increase

t = 20 s

t = 23 s

t = 50 s

T in °C

38
37
36
35
34
33
32
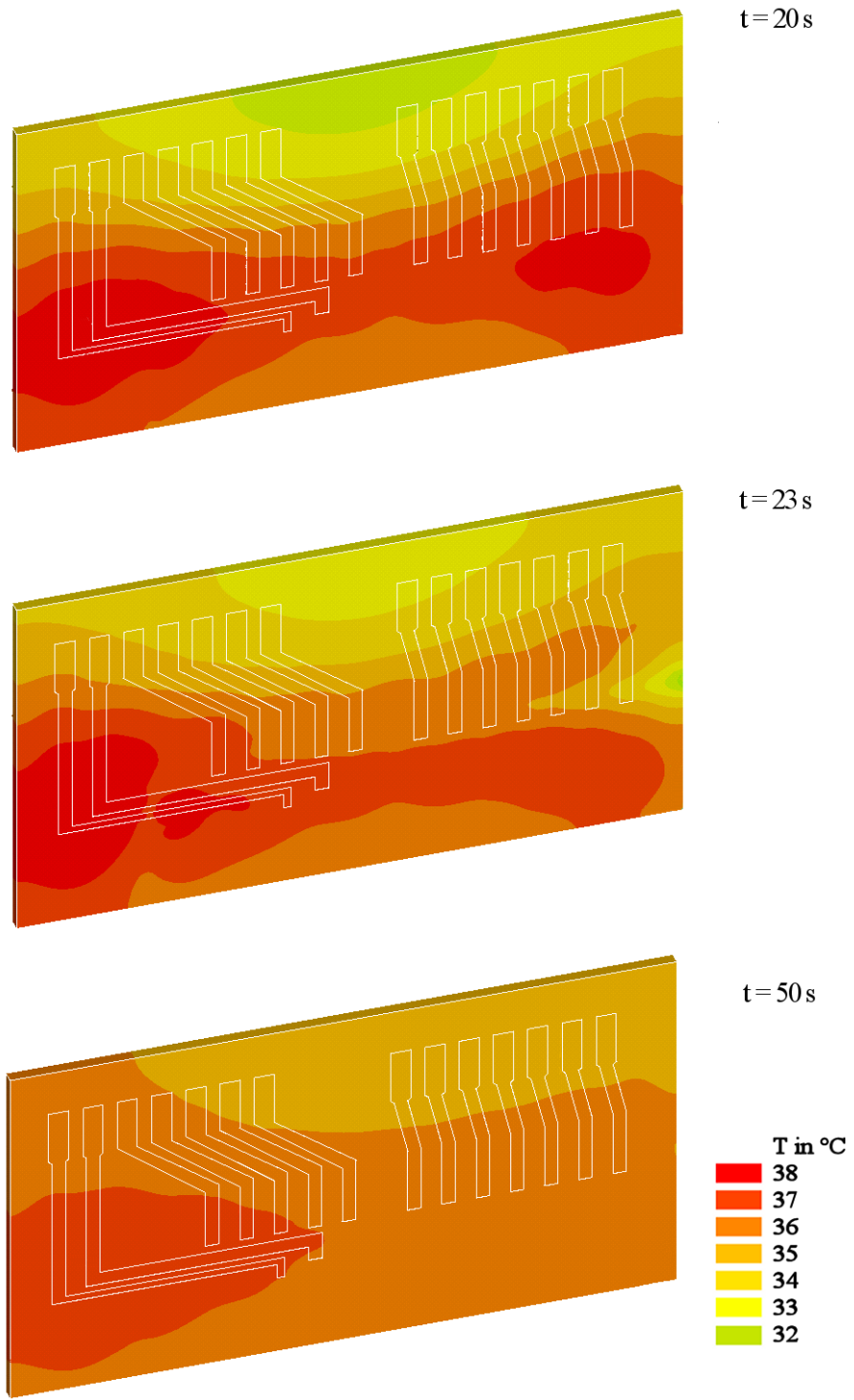
FIGURE 3.33: Temperature distribution at t=20 s before fluid exchange, t=23 s immediately after fluid exchange and at t=50 s, 14 s after fluid exchange.
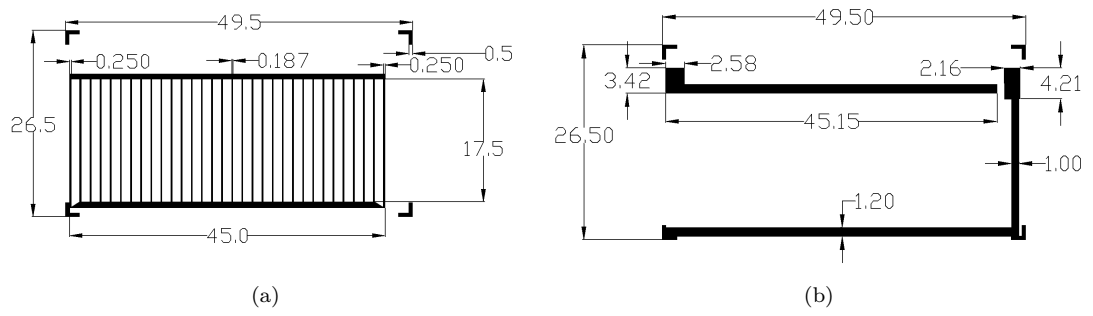
FIGURE 3.34: Resistive and connection layer of fence structure.
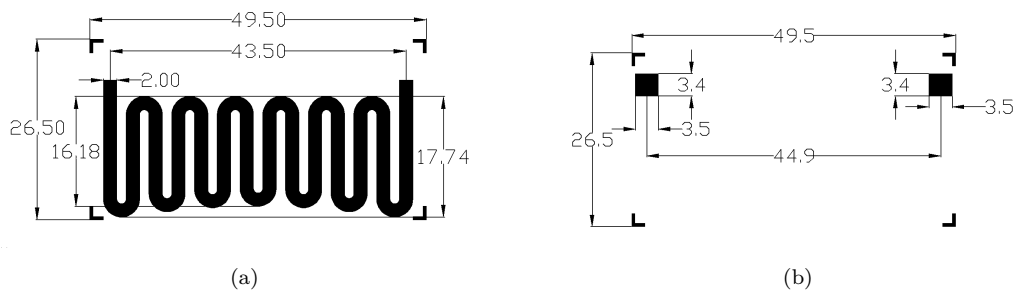




FIGURE 3.35: Resistive and connection layer of the meander structure.
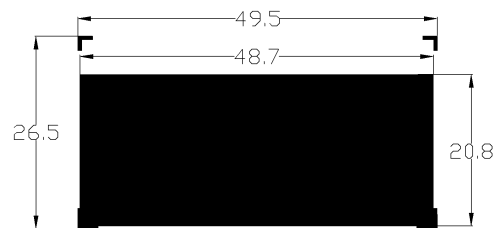


FIGURE 3.36: Passivation layer for the fence- and meander-structure.
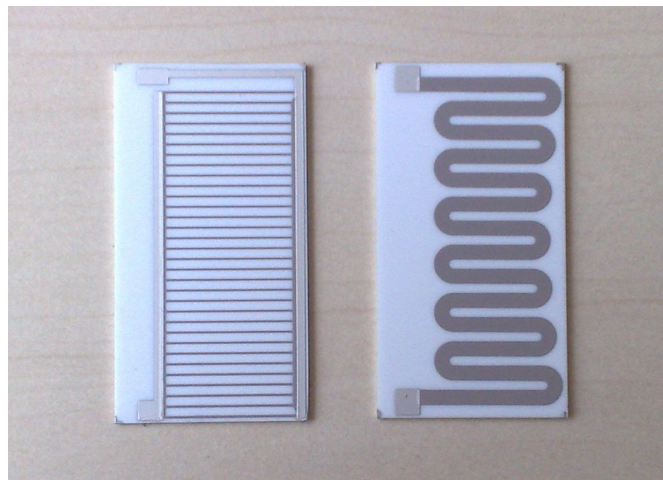


FIGURE 3.37: Fence- and meander-structure in layout version 1.
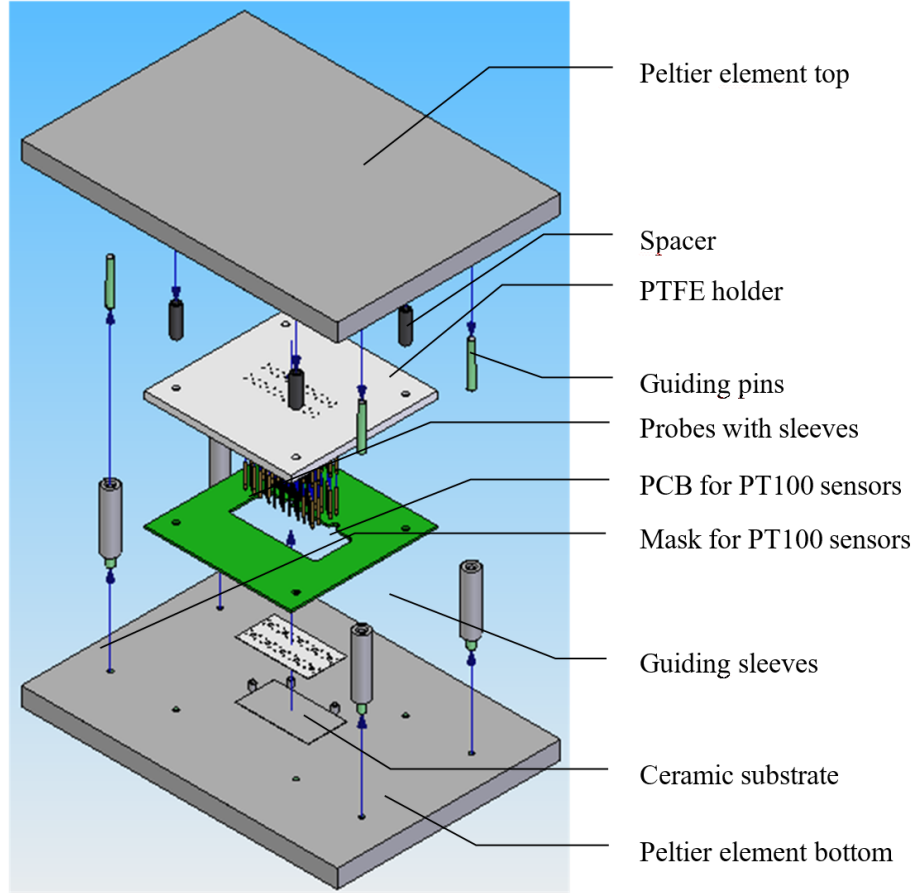
FIGURE 3.38: 3D-model of the TCR measurement setup.

| Sample | | Simula-tion | no passivation | with glass passivation | with glass passivation + aging 300 h |
|---|---|---|---|---|---|
| meander | resistance $\Omega$ | 29.7 | 33.2 +11.8% | 51.6 +55.0% | 52.54 +1.8% |
| | TCR ppmK$^{-1}$ | 3000 | 3365 +12.2% | 3310 -1.6% | 3250 -1.8% |
| Fence | resistance $\Omega$ | 0.68 | 0.78 +14.2% | 1.24 +59% | 1.25 (+0.8%) |
| | TCR ppmK$^{-1}$ | 3000 | 2846 -5.1% | 2783 -2.2% | 2951 +6.0% |

TABLE 3.7: Results from paste characterization (percentage indicates change of resistance and TCR based on previous fabrication step).

of resistance compared to the bare heater geometries in both cases(see table 3.7), the temperature coefficient of resistivity is also influenced (meander: -1.6%, fence: -2.2%). The change of the resistance over time is proportional the squre root of a diffusion coefficient $D$ and the time $t$ according to [27, p47]:

$$\Delta R \propto \sqrt{Dt} \tag{3.1}$$

41
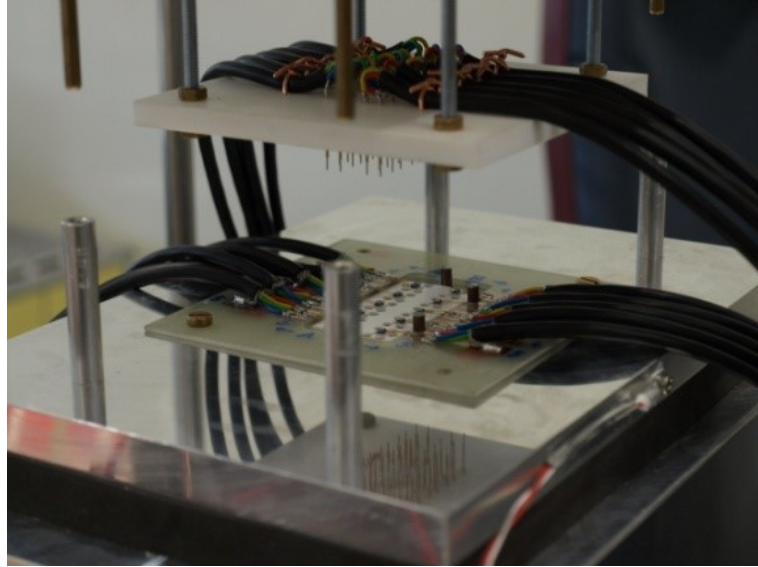
FIGURE 3.39: Image of the TCR measurement setup.
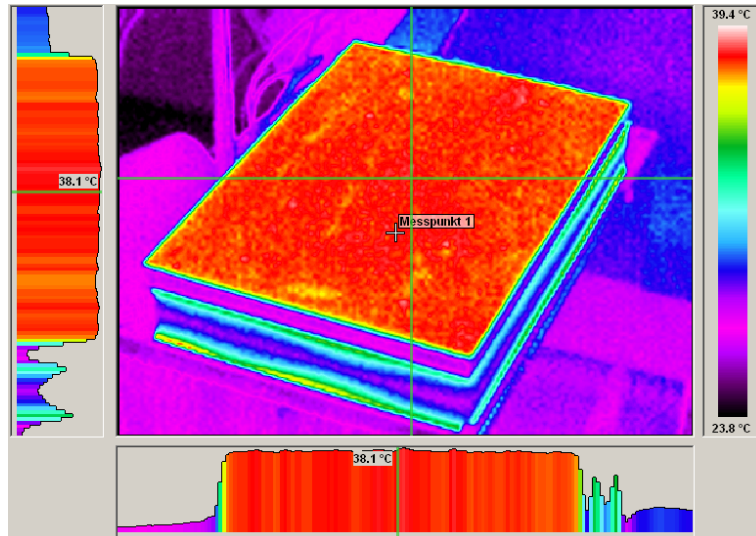


FIGURE 3.40: Temperature distribution of the temperature controlled plate of the TCR measurement setup.

The changes of the resistance due to diffusion effects are described using the Arrhenius law [28, p356] where $E_A$ is the activation Energy, $k_B$ the Boltzmann constant and T the temperature in K. The diffusion coefficient $D$ depends according to the Einstein relation on the temperature itself.

$$R = De^{\frac{E_A}{k_B T}} \tag{3.2}$$

A worst-case can be estimated by choosing a relatively low activation energy of 0.9 eV [27, p153]. The acceleration factor $a$ can be calculated by

$$a = e^{\frac{E_A}{k_B}\left(\frac{1}{T_{op}} - \frac{1}{T_t}\right)} \tag{3.3}$$
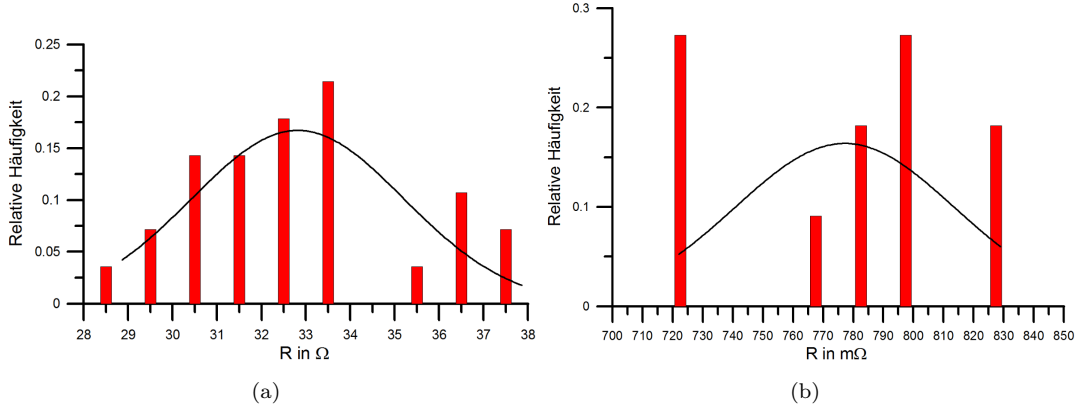
FIGURE 3.41: Resistance statistics of a) meander and b) fence heating resistors.

with the operation temperature $T_{op}$ and the test temperature $T_t$. If a worst-case operating temperature of $70\,°C$ is assumed, a test temperature of $100\,°C$, $200\,°C$ and $300\,°C$ corresponds to acceleration factors of 11, 4269 and 200563 respectively. The aging process ($300\,°C$ for $300\,h$) shows significant influence on the properties of the heater geometries (meander: $R_{25}$ +1.82%, TCR -1.8%, fence: $R_{25}$ +0.8%, TCR +6%) but stability is still high as this accelerated aging test corresponds to an operating time of 700 years at $70\,°C$. The slight difference in TCR after passivation between the two structures can be attributed to the very thin lines of the fence structure and the bigger influence in paste boundary and interface regions, which shows that the meander is superior to the fence structure.

## 3.4 Verification of temperature distribution

For analyzing the temperature distribution of the substrate, a thermography camera is used. Because the camera calculates the temperature based on the received thermal radiation of the surface, the emissivity of the surface has to be known. Because only a limited temperature range has to be considered, the sample is coated with a high emissivity varnish and the substrate temperature is measured with the embedded sensing resistors underneath the channel. In this way, a qualitative measurement for the temperature distribution can be obtained.

### 3.4.1 Estimation of self-heating of sensing resistors during operation

For precise temperature measurements, it is important to measure the resistance values of the sensing resistors with great accuracy. Therefore, a high enough voltage drop must occur to achieve the desired resolution. This could lead to self-heating of the resistors
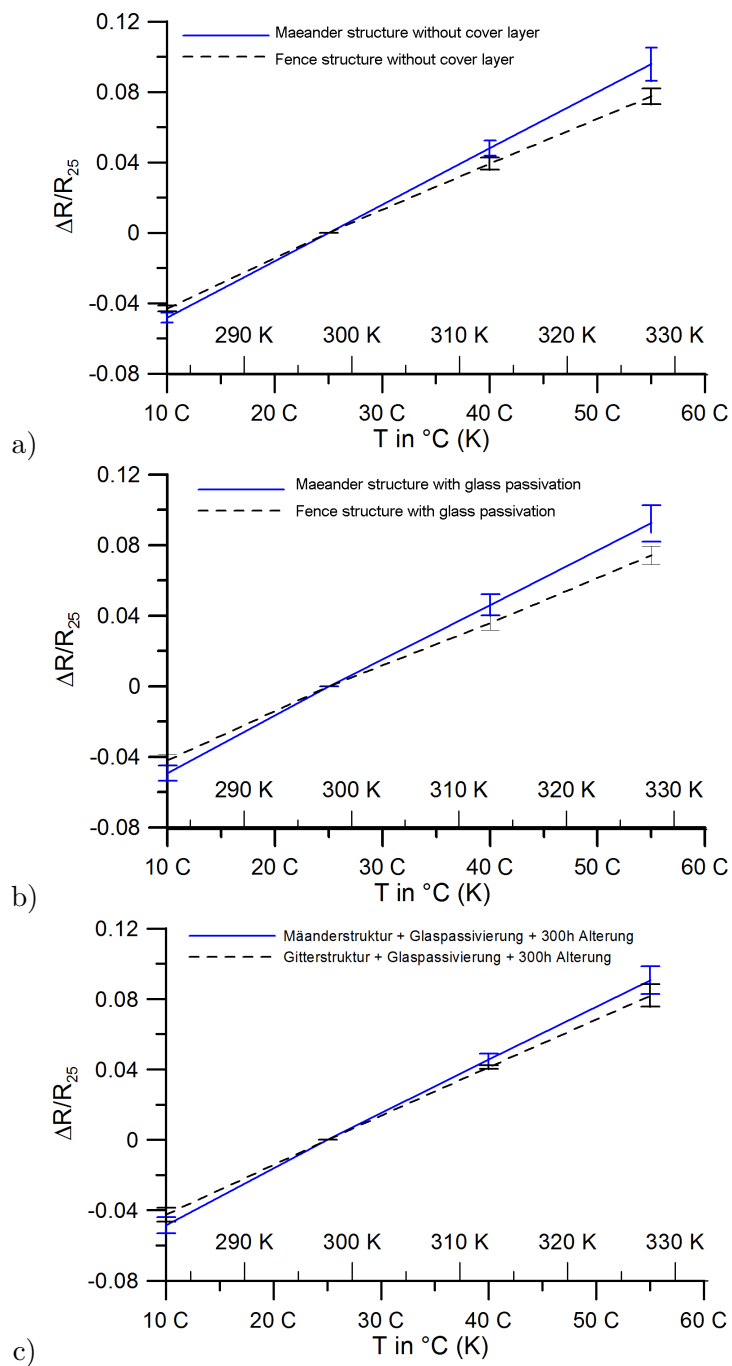
FIGURE 3.42: Experimentally assessed temperature dependence of resistance of fence and meander structure after distinct fabrication steps: a) without cover layer, b) with glass passivation and c) with additional aging for 300 h.

influencing in turn the temperature profile as well as the temperature measurement itself. In a simple FE-analysis the influence of the sensing resistors on the temperature profile is investigated. For this purpose, a simplified model was designed where a simple resistor is placed onto a $Al_2O_3$-substrate. The substrate is exposed to natural convection on all sides ($T_U = 22\,°C$, $h = 10\,W/m^2K$). The results show that a voltage drop of even $100\,mV$ is fully acceptable and no critical self-heating takes place. These values correspond to a current of less than $1\,mA$. In figure 3.43a and 3.43b the resulting temperature profiles with higher power dissipation are shown. Figure 3.43c depicts the temperature increase over time at different voltage levels at the sensing resistor. In case that the measurement leads to a significant distortion of the temperature profile, there is still the possibility of a pulsed measurement.

### 3.4.2 Manufacturing of demonstrators

Based on the results from the resistor and heating structure characterization a sensor-module with an improved meander structure together with the three temperature sensing resistors R1, R2, and R3 was realized. For practical use a build-up as shown in figure 3.44 was used with glass passivated sensing resistors that measure the temperature at critical points. Figure 3.45 shows the lateral locations of the resistors and the channel layout. The production parameters for the different process steps are summarized in table 3.8.

| layer | paste | screen print process | | | drying | sintering | |
|---|---|---|---|---|---|---|---|
| | | mesh type | mesh size | stencil thick-ness | | burnout | sinter phase |
| heater structure | ESL29230 | | 325 | 50 | | | |
| intercon-nect top | ESL9695 | | 325 | 50 | $150\,°C$, | $580\,°C$, | $850\,°C$, |
| intercon-nect bottom | ESL9695 | stain- | 325 | 50 | $15\,min$ | $10\,min$ | $10\,min$ |
| tempera-ture sensors | PTC2611 | less | 325 | 30 | | | |
| glass passivation top | ESL4771 | steel | 200 | 50 | | $350\,°C$, $10\,min$ | $550\,°C$, $10\,min$ |
| polymer passivation bottom | ESL242SB | | 200 | 50 | curing $150\,°C$, $30\,min$ | | |

TABLE 3.8: Process parameters for component pastes.
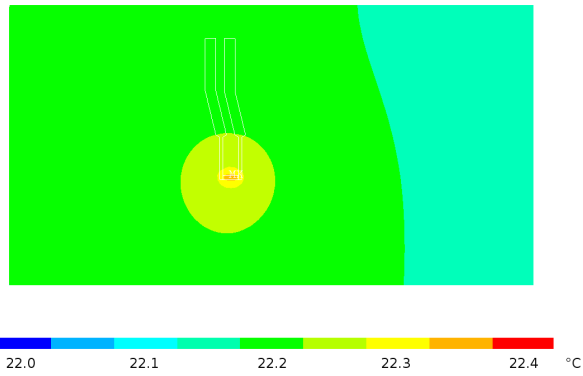
a) Temperature distribution with 0.5 V voltage drop across the resistor.
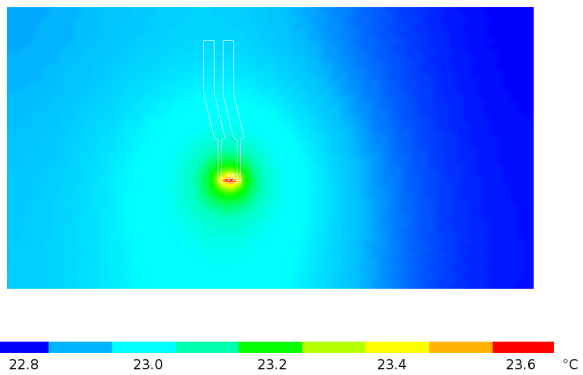


b) Temperature distribution with 1 V voltage drop across the resistor.
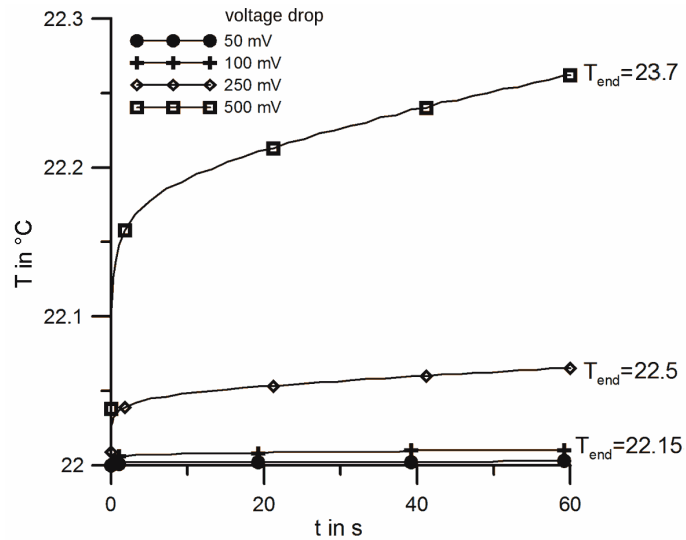


c) Temperature increase over time at different voltage drops across the sensing resistor.

FIGURE 3.43: Self-heating of a $100\,\Omega$ sensing resistor.
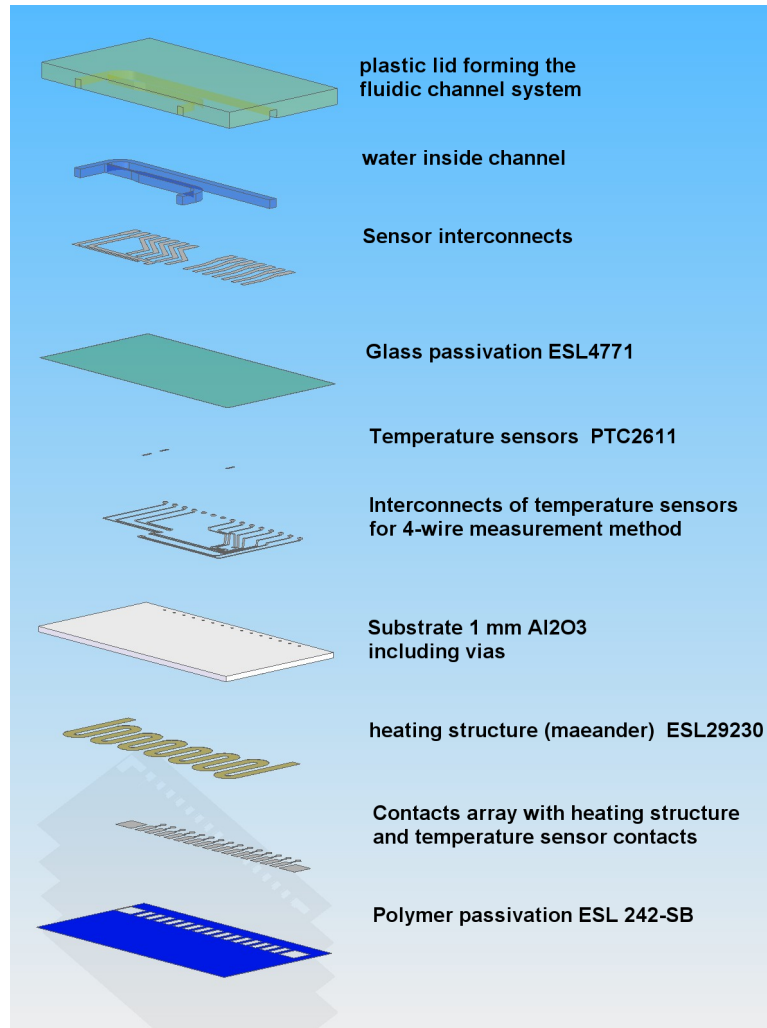
FIGURE 3.44: Explosion view if complete sensor build-up.
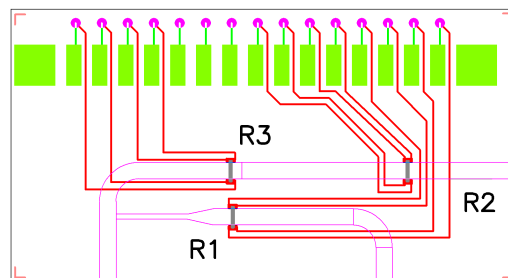


FIGURE 3.45: Positions of sensor resistors on the substrate.

The verification samples were manufactured using a 50 μm stencil reducing the resistance to roughly 12 Ω. The temperature sensing resistors R1, R2, and R3 were printed with a 30 μm stencil to increase the resistance with an applied glass passivation layer to values around 65 Ω. Resistors R1 and R3 have a uniform, while R2 has an increased layer thickness. The reason is the topology of the substrate caused an increased created stand-off height between stencil and substrate during the screen printing process which occurs for R2 to a greater extent. This leads to a thicker paste deposition and results in a lower resistance compared to R1 and R3 which can be seen in figure 3.46. Usually the resistor paste is printed first. In this case, however, the approach to apply the conductor lines first was chosen to fire the sensing resistors only once at high temperature. The substrate was glued to a plastic lid matching the dimensions used in the simulation and the channel was filled with water. The inlet and outlet ports were closed with sticky tape to seal the fluid in.

### 3.4.3 Verification of the temperature distribution

With the sensor-module, application-relevant measurements were performed and the temperature at the reference locations measured with the integrated PTC-resistors. The samples were contacted by means of a soldered contact pin array and secured in an array socket (see figure 3.47). This allows the fast exchange of devices to be tested, the thin contacts assure little heat removal and influence on the temperature profile. The resistance measurements were carried out with the Kelvin method using an OMEGA OMB-DAQ-56 USB Logger with 22 bit resolution in a ±1.5 V range. The resistors were connected in series, supplied with a measuring current and the voltage drop of each resistor recorded (see figure 3.49). For acquiring the temperature distribution, a PCE-TC3 thermography camera was used. The samples were painted with varnish with an emissivity of 0.98 because the ceramic shows a significant reflection of thermal radiation. The heating power was set to 0.33 W without a controller and a stable temperature distribution with 37 °C at the reference point was reached. Before measuring the temperature distribution, the temperature dependence of the sensing resistors had to be determined (calibration measurement). For this purpose, the sample was mounted on a Peltier-temperature control system and the resistance recorded at several temperatures (figure 3.50, resistor properties see table 3.9). Following this measurement, the sample was placed inside a plastic box to shield it from air streams and connected to a power supply. In the thermography images (figure 3.48), the temperature distribution shows the desired homogeneous distribution in the channel areas. The temperature values obtained from the embedded temperature sensors (table 3.9) match the thermography recordings very well and also qualitatively with the simulation results (see
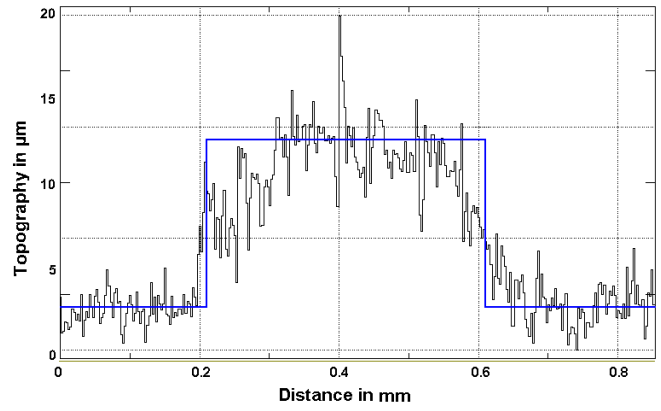
(a) R1
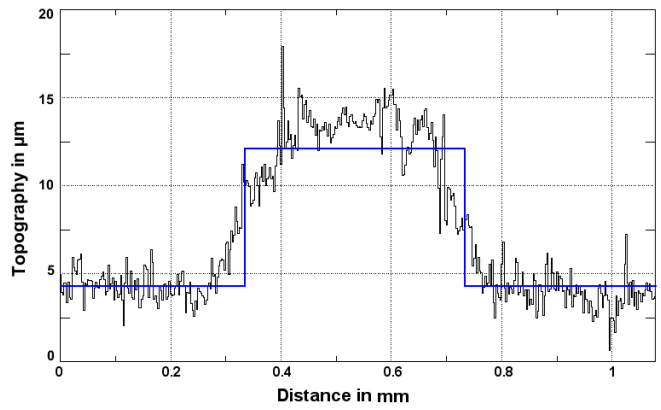


(b) R2
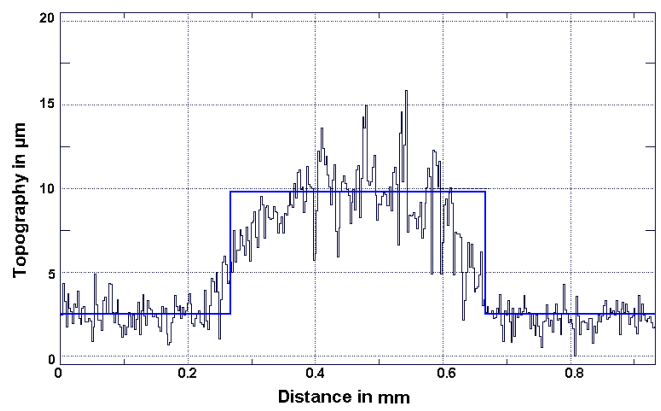


(c) R3

FIGURE 3.46: Topology of temperature sensing resistors.
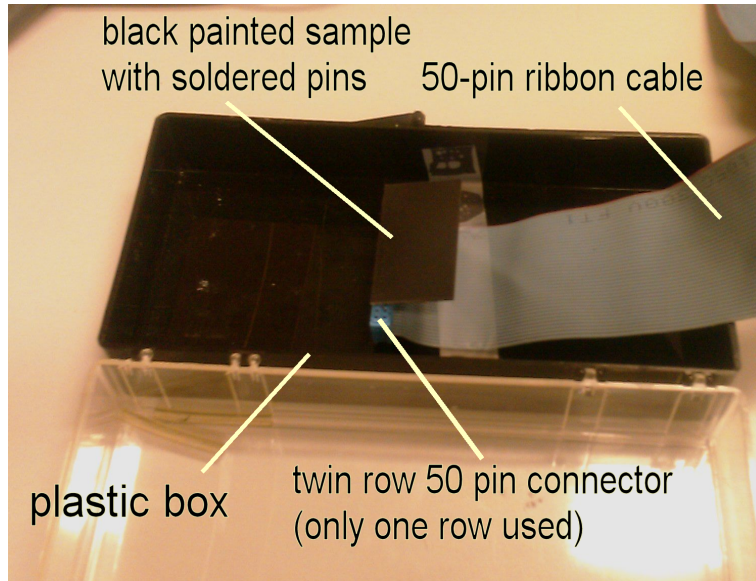
FIGURE 3.47: Measurement set-up for thermography recording.
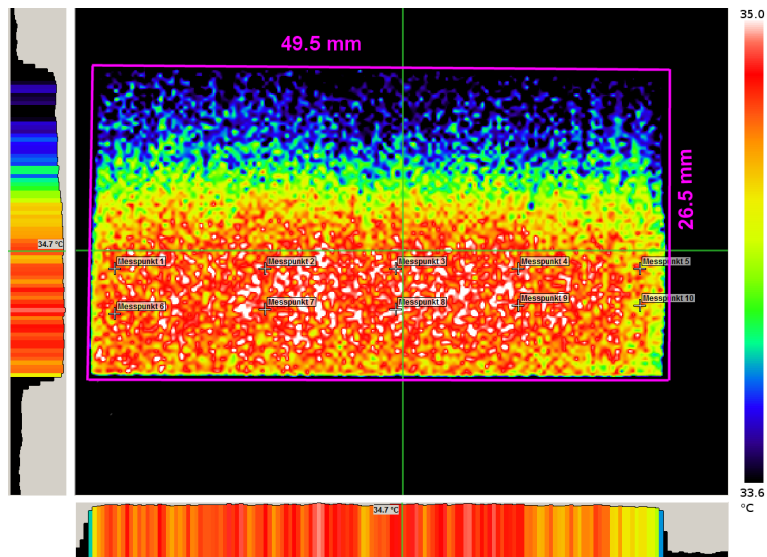


FIGURE 3.48: Thermography image of the meander-structure.

figure 3.30). Because the module was not enclosed completely, the higher convection caused a reduction of the temperature from 37 °C to only 34.7 °C. Still an exceptionally flat temperature distribution with a spatial variation of only 80 mK can be observed.

| Resistance $\Omega$ | 66.67 | 55.78 | 66.86 |
| --- | --- | --- | --- |
| TCR ppmK$-1$ | 2996 | 3014 | 3000 |
| calculated temperature C | 34.682 | 34.670 | 34.603 |

TABLE 3.9: Measurement results of resistors and correlated temperature.
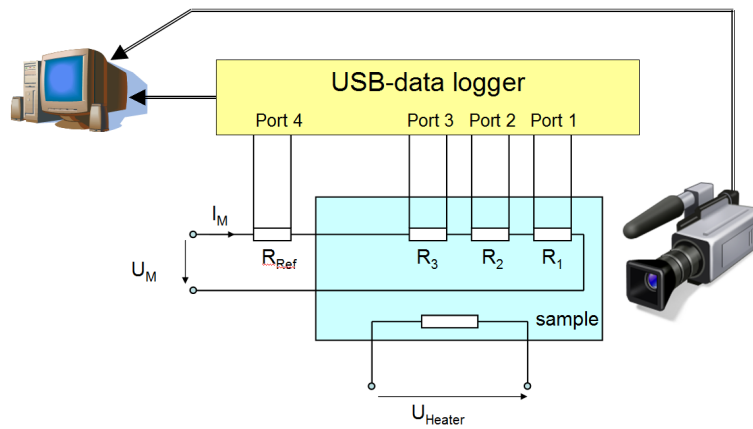
FIGURE 3.49: Overview of measurement set-up.
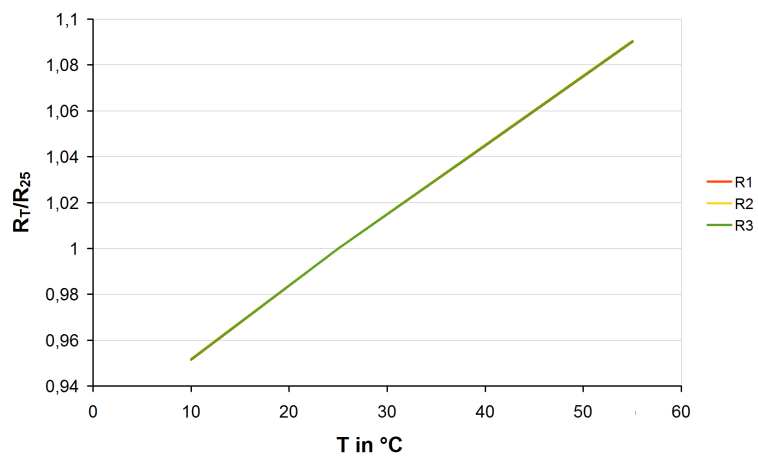


FIGURE 3.50: Sensor resistors temperature response.

### 3.4.4 Homogeneity of the temperature distribution of the fence-structure

For the verification of the temperature distribution of the fence structure a sample without embedded temperature sensing resistors was used. The sample was connected to the power supply only by a thin wire to reduce the temperature profile distortion caused by the heat escaping via the connection. The fence structure was heated like the meander structure by a power of 0.33 W. The temperature profile obtained by thermography matches the simulation results (compare figure 3.23 and figure 3.52). Further investigations were not conducted because this design was not considered useful for the realization of the demonstrators.



FIGURE 3.51: Measurement set-up for thermography recording.
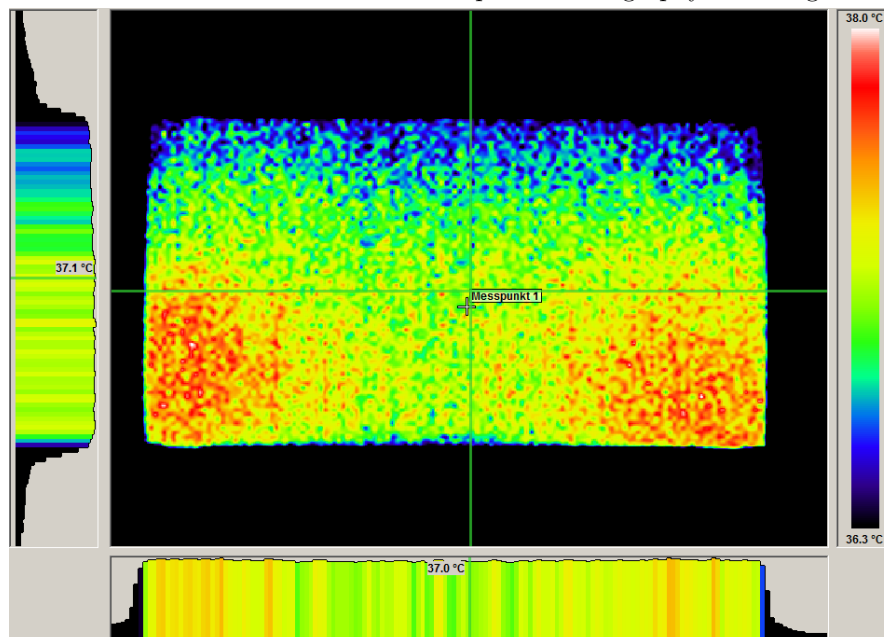


FIGURE 3.52: Thermography image for the fence-structure.

## 3.5   Conclusions

The study shows that it is possible to achieve a homogeneous temperature distribution on the carrier substrate alone with a heater structure where the lateral temperature gradient as well as the vertical gradient inside the channel is exceptionally small and, therefore, allows the measurement with the sensors placed inside the channel. The measurement results obtained from the test vehicles match the simulation results very well. The temperature profile recorded with thermography of the final optimized meander structure has the high homogeneity as expected and shows a very well correlation with the temperature values from the integrated temperature sensors. The application of a passivation layer causes an almost doubling in resistance value for both, the meander and the fence structure. The aging tests confirmed a high stability of heating and resistor paste. However, the increase in resistance caused by the passivation layer must be considered during the design phase. The fence structure is in general useful but not applicable to this design due to a very low resistance. It exhibits an opposite change of the TCR during aging compared to the meander structure (+6% compared to -1.8%). This is caused by boundary effects where the resistor paste is influenced largely by passivation and conductor interfaces. This means that the track width is simply too narrow and will cause problems. The polymer passivation had no effect on the behavior of the resistors as it is cured at a much lower temperature compared to the glass passivation. The remaining small but noticeable asymmetry in temperature distribution suggests that the usage of a flow-through heater could further improve the performance of the module if necessary.

# Chapter 4

# Flow-through heater

Many biochemical or biomedical applications involving enzymatic measurement methods require highly stable temperature distribution during measurement - usually $37\,°C$ as for instance with alkaline phosphatase [5]. If the measurement is carried out on a per cycle basis where the channel system is flushed and the sample liquid exchanged, the heating during discontinuous flow is generally not critical. The measurement module including the fluid can be heated together and the desired stable temperature distribution will be reached after a given time. This is no longer possible when the cycle rate is increased and the settling time can no longer be met or the measurement is carried out continuously e.g. to monitor blood contents in real time. The fluid exchange must not change the temperature distribution inside the critical measurement sections of the module. For this reason, a separate continuous-flow heater with controller circuit is required to allow immediate measurement after fluid exchange. Care must be taken that the fluids are heated to an maximum allowable temperature level bot not overheated. This chapter of the thesis focuses on the temperature profile inside the fluid channel of the flow-through heater module and presents an optimization process yielding a homogeneous temperature profile at the heater outlet for varying geometry at different flow rates and fluid temperature as well as their possible realization in LTCC technology. The first step is performed as an FEM-study to investigate the quality of the temperature profile using a small defeatured model [29]. The second step is the design of an LTCC module with heating meanders that is then simulated (multiphysics), built and characterized.

## 4.1   Finite Element Modeling Based Study

For modeling the continuous-flow heater, the section containing the heater is investigated regarding the effects of varying heater chamber width, number of heating layers

and heating power. Different solutions are then compared and conclusions are drawn. According to the Hagen-Poiseuille-law for a rectangular shaped channel [30], the velocity profile inside the channel has parabolic shape. In order to simplify the calculation, an analysis is run with a test pressure to extract the overall flow resistance of the channel geometry. Because the flow rate is proportional to the pressure drop, it is possible to calculate the necessary pressure that has to be applied to achieve the desired flow rate according to the following equation:

$$\dot{V} = \frac{K \cdot h^3 \cdot \omega}{12\mu \cdot l} \Delta p = R_{flow}^{-1} \cdot \Delta p \qquad (4.1)$$

where $\dot{V}$ denotes the volumetric flow rate, $K$ the correction parameter for the aspect ratio of the channel, $\mu$ the viscosity, $l$ the channel length and $\Delta$p the pressure drop. The height $h$ of the channel is smaller than the width $w$ of the channel. For channels where $h>w$, $h$ and $w$ have to be exchanged. $K$ depends on the aspect ratio $w/h$ of the channel and ranges from 0.42 for $w/h = 1$ to approximately 0.9 for $w/h = 7.5$. The effect of all these parameters can be expressed as a flow resistance $R_{flow}$. The heating power is calculated via equation 4.2 from the theoretical energy carried by the fluid when heated from room temperature 22 °C to the desired temperature of 37 °C. The actual heat transfer rate to the fluid is determined via the temperature profile at the outlet.

$$P_{fluid} = \dot{V} \cdot \rho c_P \cdot \Delta T \qquad (4.2)$$

$P_{fluid}$ is the required heating power, $\rho$ the fluid density, $c_p$ the heat capacity respectively and $\Delta T$ the desired increase in temperature. Because fluid simulations can be problematic regarding the convergence, it is important to check not only the plausibility of the temperature distribution but also the heat balance if the heat carried by the fluid $P_{fluid}$ and losses through convection $P_{conv}$ are consistent with the input power.

$$P = P_{conv} + P_{fluid} \qquad (4.3)$$

Based on equations 4.2 and 4.3 a heat transfer efficiency can then be defined as

$$\eta = P_{fluid}/P \qquad (4.4)$$

whereby this formulation expresses that any $\eta < 100\%$ is due to heat losses by convection at the module's surface.

### 4.1.1 FE-Model

In a provisional approach, a model containing only two heating layers was considered. The module consists of a ceramic block with an embedded fluid channel that widens into the heating section. The bulk material of the module is Heraeus CT800, CeramTec GC or $Al_2O_3$. These materials have been proven usable for biological applications, sinter sufficiently dense and are compatible with the available pastes [31, 32]. Figure 4.1 shows the model setup with inlet and outlet port and a heating chamber of 10 mm width. Tables 4.1 and 4.2 give an overview of applicable material properties and the geometric dimensions. For this study, the heater geometry has been simplified to be a homogeneously heated section of bulk material as shown in figure 4.1. For all surfaces except inlet and outlet port, free air convection was specified. Fluid outlet pressure $p_{OUT}$ was set to 0 at the outlet and inlet pressure was calculated to achieve the desired flow rate.

| **Material** | | | **Bulk material (fired)** | | | **Fluid** | |
|---|---|---|---|---|---|---|---|
| **Property** | | | **Heraeus CT800 [6]** | **CeramTec GC [7]** | **$Al_2O_3$ [5]** | **$H_2O$ [5]** | **Air [5]** |
| density | $\rho$ | [kgm$^{-3}$] | 3200 | 2920 | 3900 | 1000 | 1.2 |
| heat capacity | $C_P$ | [Jkg$^{-1}$K$^{-1}$] | --- | --- | --- | 4187 | 1.005 |
| therm. conductivity | k | [Wm$^{-1}$K$^{-1}$] | 4.3 | 2.2 | 27 | 0.597 | 0.055 |
| viscosity | $\mu$ | [Pa s] | -- | -- | -- | 1 | 17.1E-6 |

TABLE 4.1: Material properties for FE-model.

| **Component** | **Length** mm | **Width** mm | **Height** mm | **Material** |
|---|---|---|---|---|
| Ceramic Block | 15 | 15 | 4 | Heraeus CT800 or CeramTec GC |
| Channel inlet & outlet | --- | 1.6 | 1.6 | fluid |
| Heater section | 5 | $w$ | 1.6 | fluid |
| Widening section | 3 | 1.6 to $w$ | 1.6 | fluid |
| Heating fin layers | 5 | $w$ | 0.1 | Heraeus CT800 or CeramTec GC 2-5 layers |

TABLE 4.2: Model Geometric parameters.
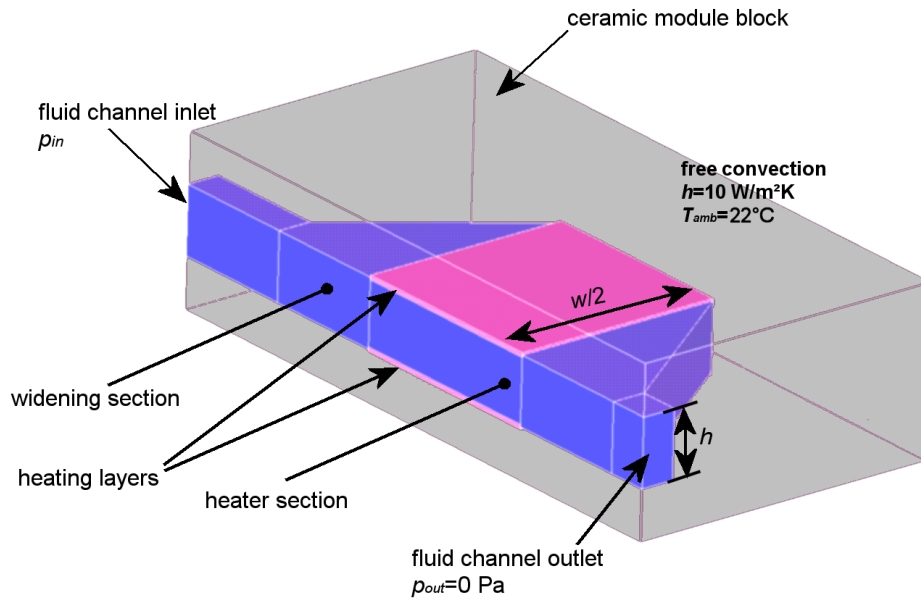
FIGURE 4.1: FE-Model overview as cross section along symmetry axis.

## 4.1.2 Influence of heating chamber width on the temperature distribution

It can be foreseen that at a high flow rate heating up fluid layers close to the horizontal symmetry plane (due to their larger distance to the heater planes)enough effectively is possible (due to their larger distance to the heater planes). In order to reduce the flow velocity the chamber width is increased between the heaters. The steady-state temperature distribution in the entire module, particularly the profile in the fluid, is analyzed by applying such a heating power level $P_{fluid}$ according to equation 4.2 that at the outlet a mean fluid temperature of $37\,°\mathrm{C}$ is obtained. Under this condition, we can observe that the heat loss $P_{conv}$ dissipating from the module's surface by convection increases with diminishing flow rate. In figure 4.3 this tendency is expressed by the dependence of the heat transfer efficiency in a range of $0.1 \leq \dot{V} \leq 25\,\mathrm{ml\,min^{-1}}$. A strong non-linearity is visible: the gain of efficiency becomes very small with increasing flow rate above a level of around $5\,\mathrm{ml\,min^{-1}}$. This is important because a further increase of flow rate degrades temperature homogeneity and is related to overheating of the fluid in the vicinity of the heaters. On the other hand, by increasing the chamber width the flow velocity at a given flow rate is lowered. Figure 4.4 depicts this tendency. But it also shows that lowering of the fluid's maximum temperature $T_{max,Fluid}$ becomes less significant above a width of around $12\,\mathrm{mm}$. Similarly, the flow resistance $R_{flow}$ showing a strong decrease with increasing width, becomes almost insensitive to variations of the width beyond the same level of about $12\,\mathrm{mm}$ (figure 4.5). Based on these results we consider a variation range of

the channel width of $1.6\,\text{mm} \leq w \leq 12.5\,\text{mm}$ for further investigations and refinements on the heater design. Figure 4.2 shows the temperature distribution in the longitudinal cross-section resulting from simulations with a flow rate of $5\,\text{ml}\,\text{min}^{-1}$. The highest flow velocity is obtained with the smallest channel width (1.6 mm) leading to the lowest surface temperature, but to high temperature differences in the outlet plane (figure 4.3). The successive improvement of the homogeneity of the fluid temperature profile in the outlet can be recognized in the following illustrations obtained from simulations with increasing width. At a channel width of 12.5 mm (figure 4.2) the flow velocity is already so low that a significant part of the applied power is dissipated at the module surface.
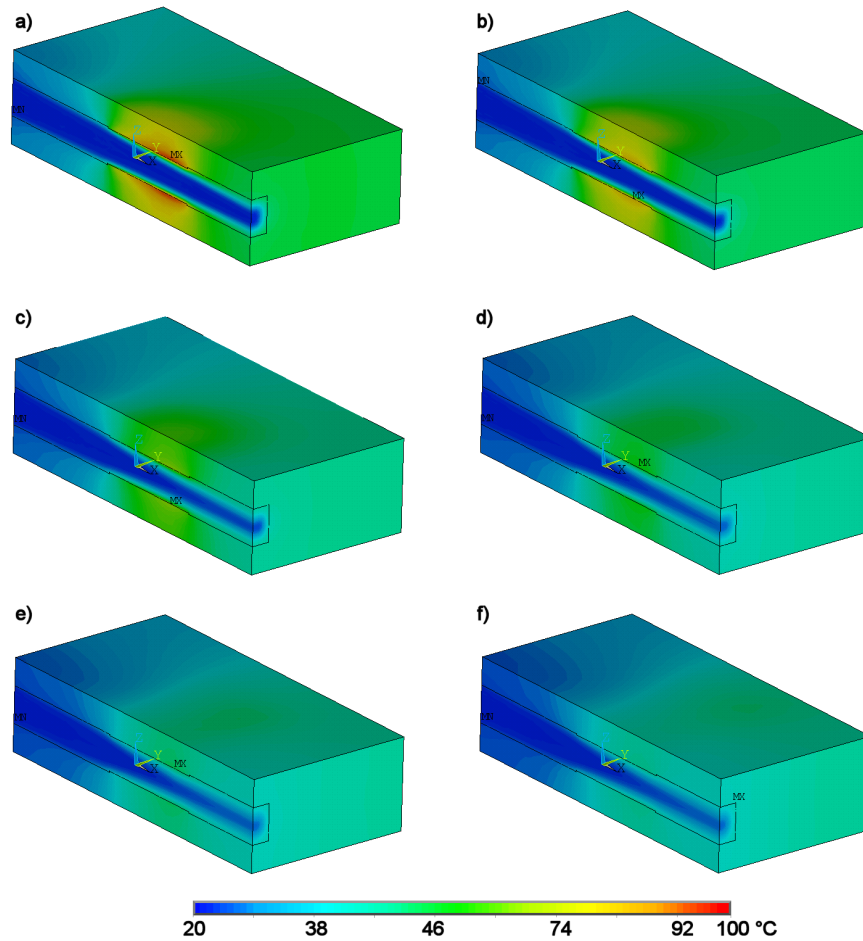


FIGURE 4.2: Temperature distribution using CT800 as bulk material with different chamber width: a) 1.6 mm, b) 2.5 mm, c) 5 mm, d) 7.5 mm, e) 10 mm, and f) 12.5 mm and a flow rate $\dot{V}=5\,\text{ml}\,\text{min}^{-1}$.
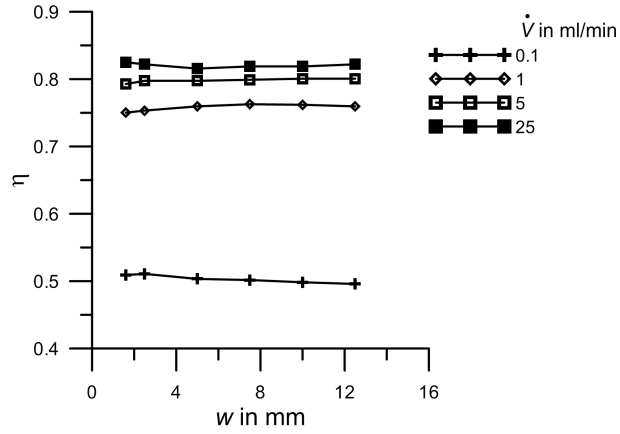
FIGURE 4.3: Heat transfer efficiency obtained with different applied materials using two different flow rates in dependence of the channel width.
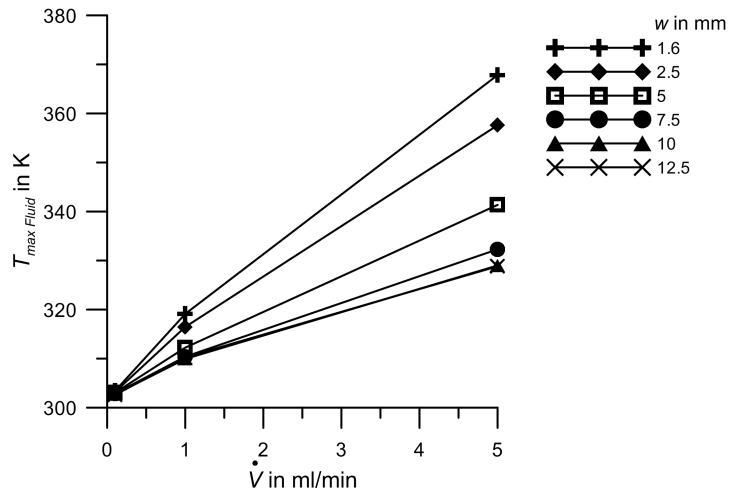


FIGURE 4.4: Maximum fluid temperature for two different flow rates and three different channel widths versus the bulk material's thermal conductivity.
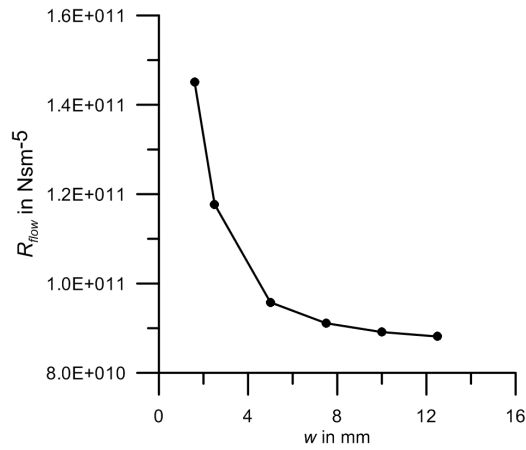


FIGURE 4.5: Resulting flow resistance for varying chamber width.

### 4.1.3 Influence of material properties on the temperature distribution

The heating power is assumed to be generated at the inner sides of the heating layers over a rather large area. The parabolic flow profile of the fluid across the flow axis leads to a strong spatial dependence of the heat transfer coefficient between fluid and heaters. This causes a temperature gradient across the flow axis and in turn influences the temperature homogeneity of the fluid. Nevertheless, a uniform temperature profile can be expected if the heat is spread effectively inside the module block. For this reason, it is important to consider the influence of the thermal conductivity of the chosen block material. In the following investigation, a 10 mm wide heating chamber and flow rates of 1 and 5 ml min$^{-1}$ have been selected. The calculated heating power necessary to heat the fluid from room temperature to the desired level of 37 °C has been applied evenly distributed over the inner surfaces of the two heater layers. Figure 4.8 show the temperature distributions in the longitudinal symmetry plane of the channel obtained for three different values of bulk material thermal conductivity. The maximum observed temperature $T_{maxFluid}$ is decreasing with increasing thermal conductivity regardless of flow rate and the respective channel width (figure 4.7). While at low flow velocity (1 ml min$^{-1}$) a high thermal conductivity ($Al_2O_3$, 27 W m$^{-1}$ K) leads to higher losses due to convection, a higher flow rate 5 ml min$^{-1}$ the same good thermal conductivity helps to improve the heat transfer efficiency $\eta$. This effect can clearly be recognized in figure 4.6 where $\eta$ is more than 10% higher at a flow rate of 5 ml min$^{-1}$ than at 1 ml min$^{-1}$.

### 4.1.4 Effect of additional heated bridges on the temperature distribution

Increasing the channel width slows down the fluid flow inside the heating chamber but the fluid is still only heated on the channel walls. The heat diffusion through the fluid to the channel center is still limited. For higher flow rates, it is necessary to subdivide the volume of moving fluid into separately heated streams. For this purpose, heated bridges or lamellas are introduced into the channel at the widest section. For this study, the overall channel height was kept constant (h = 1.6 mm) and additional 100 μm thick layers were introduced as bridges inside the heating chamber (figure 4.9). Figures 4.10 and figure 4.7 show the heat transfer efficiency and the maximum fluid temperature in dependence on the number of heated bridges. The relation between number of heated bridges and flow resistance is shown in figure 4.12. Figure 4.13 shows the temperature distribution of the fluid volume with a chamber width w = 10 mm and a flow rate $\dot{V} = 5$ ml min$^{-1}$ for a different number of heated bridges: a) two layers as
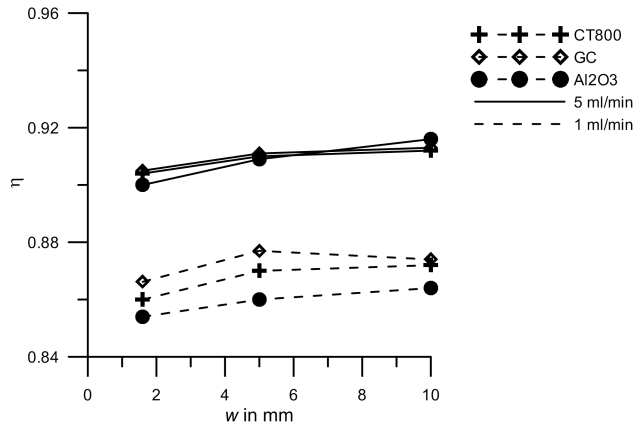
FIGURE 4.6: Heat transfer efficiency with different applied materials.
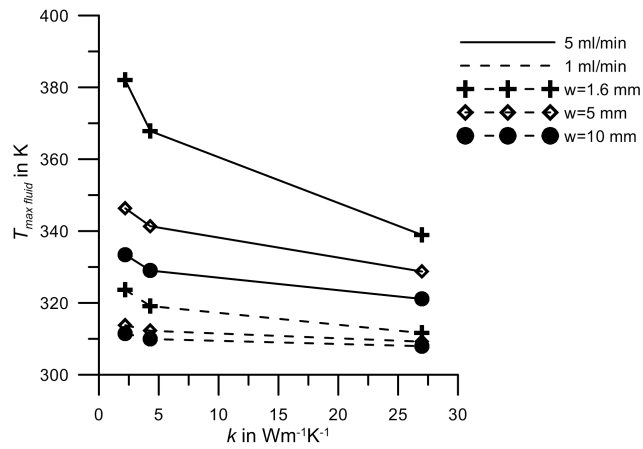


FIGURE 4.7: Maximum fluid temperature for different flow rate and bulk materials.

before (at the upper and lower side of the body) and b) to d) with additional one to three heated bridges (sub figures a to d) for the two materials A) $Al_2O_3$ and B) Heraeus CT800. With increasing number of heated bridges, a generally improved homogeneity of the temperature profile over the cross section of the channel can be observed. When in addition a material like $Al_2O_3$ with a better thermal conductivity is used, the heat can be distributed across the heating layers more easily and thus a greater amount of heat is transferred to the fluid at lower differential temperature. This results in a further improvement of the temperature profile at the module outlet.
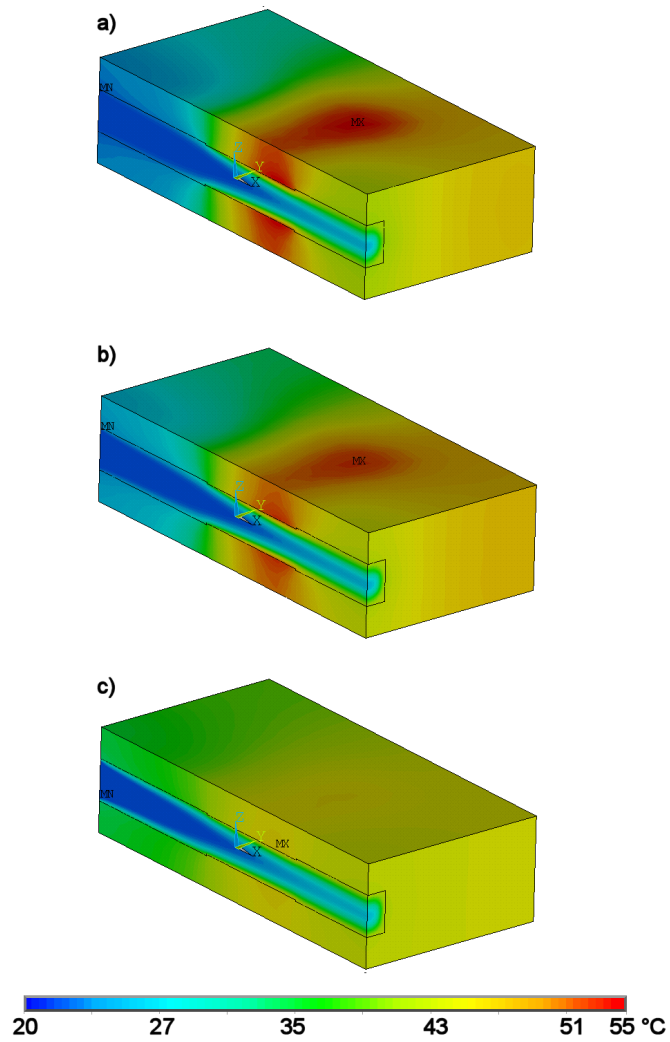
FIGURE 4.8: Temperature distribution using different bulk materials:
a) CeramTec GC (k = 1.2 Wm⁻¹K⁻¹), b) Heraeus CT800 (k = 4.3 Wm⁻¹K⁻¹) and c) Al$_2$O$_3$
(k = 27 Wm⁻¹K⁻¹) at a flow rate of $\dot{V}$ = 5 ml min⁻¹ and a chamber width of w = 10 mm.
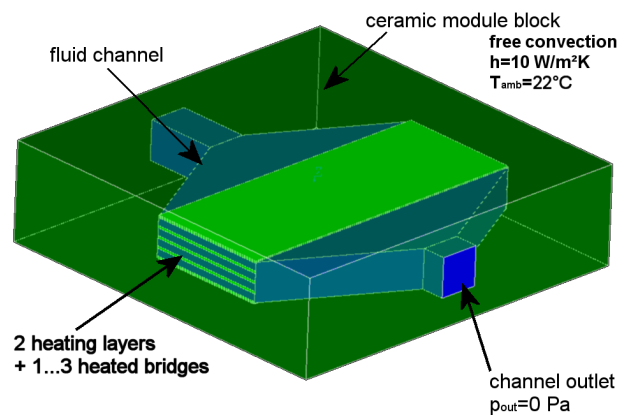


FIGURE 4.9: Extended model of flow-through heater with additional heated bridges.
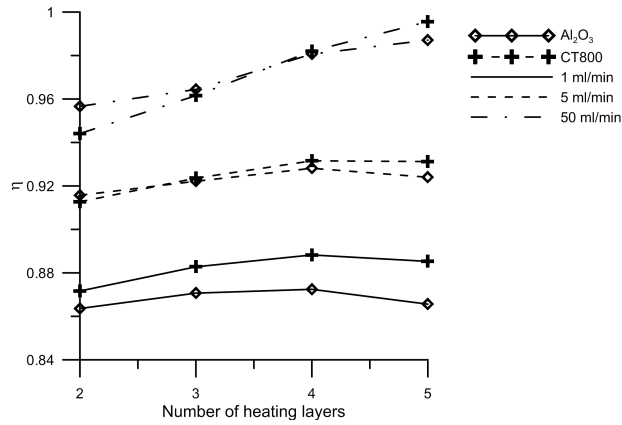
FIGURE 4.10: Heat transfer efficiency for w = 10 mm, depending on flow rate, material and number of heated bridges.
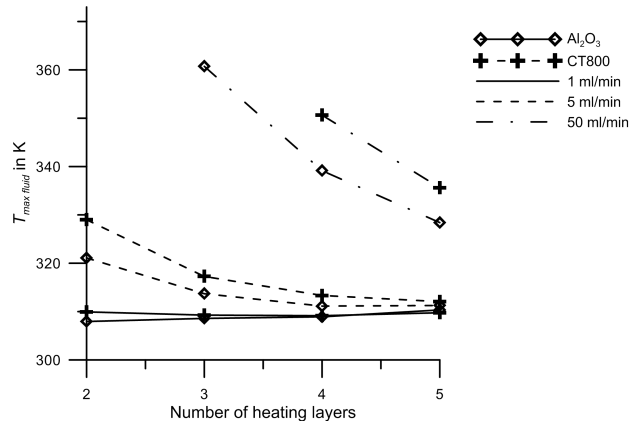


FIGURE 4.11: Maximum fluid temperature inside the channel system for w = 10 mm, depending on flow rate, material and number of heated bridges.
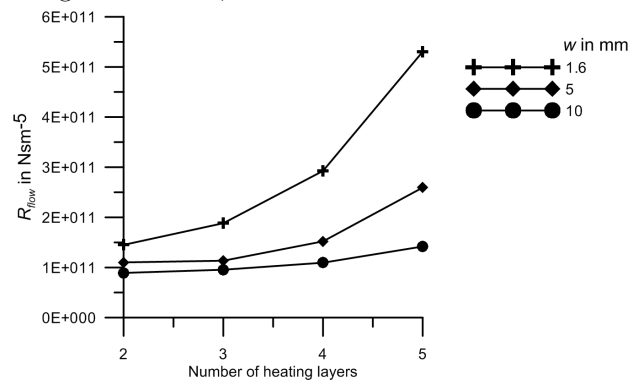


FIGURE 4.12: Resulting flow resistance for varying chamber width and number of heated bridges.
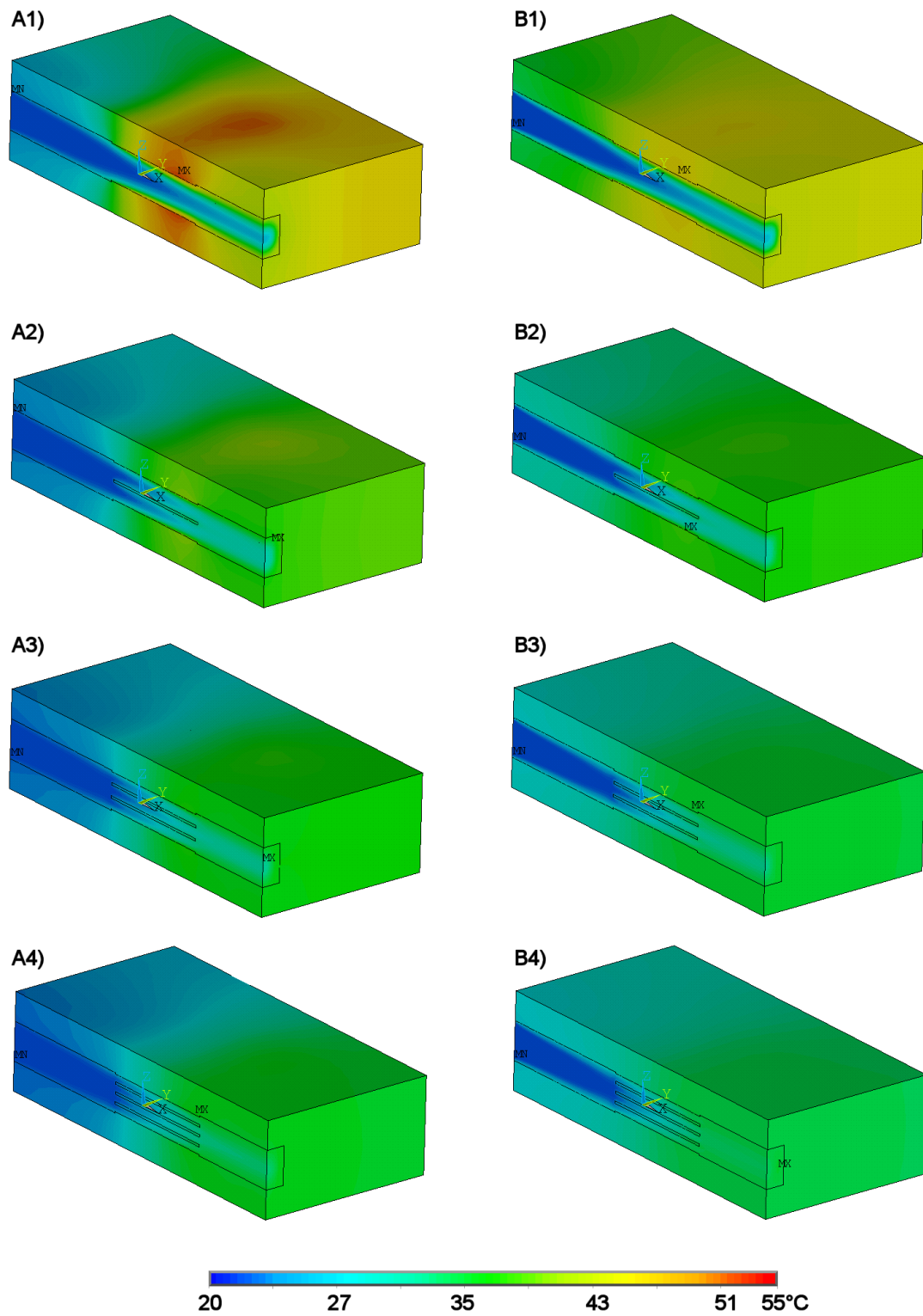
FIGURE 4.13: Temperature distribution using different materials and number of heated bridges: A) CT800 and B) $Al_2O_3$ as bulk material with 2 to 5 heating layers($1 = 2$ heating layers, $4 = +3$ heated bridges), $\dot{V} = 5\,\mathrm{ml\,min^{-1}}$ and $w = 10\,\mathrm{mm}$

### 4.1.5 Result Summary

The FE-analyses showed that a high thermal conductivity is beneficial for the temperature profile. Also the additional heated bridges improve the temperature homogeneity and the heat transfer efficiency. Therefore, $Al_2O_3$ sintered at high temperature $1500\,°C$ would be desirable as bulk material. However, only LTCC pastes are available with the required electrical properties that are not compatible with the high sintering temperature. For this reason, Heraeus CT800 was chosen instead, which is fired at $865\,°C$ as the best alternative to $Al_2O_3$ tapes for the realization of a prototype. The study also showed that an optimal flow rate exists where the temperature profile at the outlet is mostly homogeneous. If the channel is widened too much an equally distributed power across the bridges leads to a hot spot inside the channel. This means the design parameters channel width and number of heated bridges can pose a limit regarding the range of flow rates. Therefore, an adjusted power dissipation and heater design considering the localized flow rate of each specific lamella is a further possibility to reach the desired temperature distribution.

## 4.2 Design of Test Vehicle Design and Realization of Prototype

At the first glance, the design presented in this section seems oversized for its purpose especially when using a very large bridge structure inside the module. However, the reason that this particular design was chosen to explore the feasibility not only as a flow-through heater that is operated near room temperature but also for potential application in high temperature chemical synthesis. The feasibility is not only determined by the fact that the module can be manufactured but also to obtain the predicted quality of the temperature profile. An important topic is therefore the verification of the achieved temperature profile inside the channel. A measurement system using a scanning technique with a CNC-system employing a miniature thermocouple was developed and successfully used for this purpose. Additionally, the design was first created inside a PCB-layout system and the geometry data transferred to the ANSYS simulation environment. A special method had to be developed in order to transfer the layout-data to ANSYS easily, which is described in the next chapter.

### 4.2.1 Prototype design and simulation based optimization

As a trial for the feasibility of the proposed setup, a module layout with three heating layers was considered (one bottom, one top and one additional heater in the middle of the fluid channel). The heater structure is a simple meander resistor with one temperature sensor in the up- and one in the downstream region. For simplicity of fabrication, the layout is equal for all three heating layers with cut-outs enabling the access to the embedded layers. Figure 4.19 gives an impression of the layer stack-up. This simplistic approach was chosen to minimize the number of screens required and to omit vias, which require additional process steps during prototype realization. The design of the module was created using PCB-CAD Software and further processed using the in-house tool TRESCOM [33]. The actual simulation was again performed in ANSYS. The inlet was set to the respective inlet temperature of $25\,°C$ and zero inlet pressure. A negative pressure was applied to the outlet in order to achieve the desired flow rate. To the outer surfaces, a convection boundary condition was applied using a heat transfer coefficient of $10\,W\,m^{-2}\,K$ and the same temperature like the inlet of $25\,°C$. The simulation was performed with two separate solver runs for electrical simulation and fluid simulation with mutual exchange of electrical power loss created by the temperature dependent resistance and temperature distribution calculated from the fluid flow.

Figure 4.14 shows the temperature distribution on the topside of the module as well as a cross section through the module where a significantly higher temperature at the heater/fluid interface is observed. The channel outlet's temperature profile as well as the fluid velocity is shown in detail in figure 4.15. The temperature distribution inside the heater section hints at two problems:

a) The localized higher temperature of the heater can cause thermomechanical problems. Therefore, this effect is limiting the possible input power to the heater.

b) The fluid is already overheated at the heater while at the outlet the desired temperature is not reached at the particular flow velocity. Furthermore, the fluid velocity profile exhibits a slight asymmetry in vertical direction, which is caused by the single sided input flow. In addition, the asymmetry of the conductor lines in vicinity of the heater influences the quality of the temperature profile in a negative way.

The electrical simulation results show that no significant difference in power loss density is present across the meander, only at the bends of the meander the expected maxima are observed (figure 4.17). Also the voltage drop is without abnormalities as can be seen in figure 4.16.
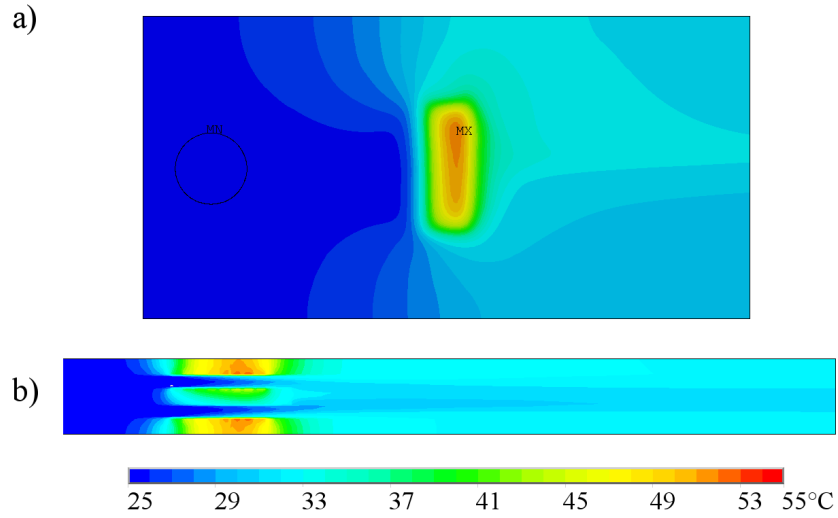
FIGURE 4.14: Temperature distribution using $Al_2O_3$ substrates with 3 heating layers and a flow rate of $\dot{V}=20\,\mathrm{ml\,min^{-1}}$ as a) top view and b) cross section.
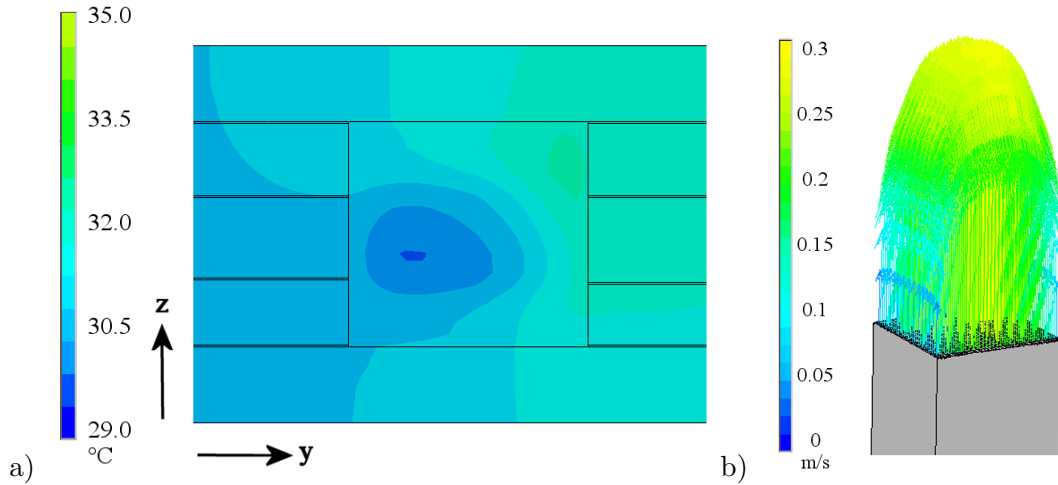


FIGURE 4.15: a) Temperature distribution at the outlet surface and b) corresponding fluid velocity profile.

## 4.2.2 Manufacturing

For the heating bridges (lamellas) the unfired tape layers were first structured with a q-switched Nd:YAG laser. Then resistor and conductor structures were applied via screen-printing followed by a drying step. The heating layers were combined with a cover layer of same thickness to seal in the electric components but provide acceptable thermal coupling to the fluid. The rest of the module was processed using three different methods to achieve the most reliable and geometrically correct prototype. Figure 4.18 shows the proposed stackup for the LTCC version, which can be replaced by an equivalent version made in thickfilm technology. The layers are laser-structured sintered-alumina substrates that after applying the conductive and resistive traces followed by sintering are joined with glass solder.

67
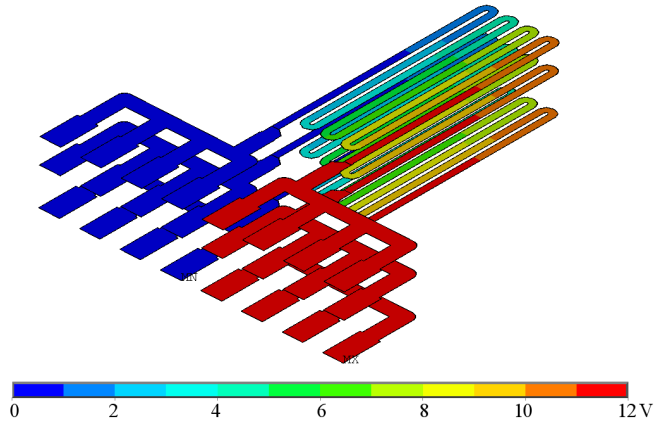
FIGURE 4.16: Simulated potential across meander with an operating voltage of 12 V.
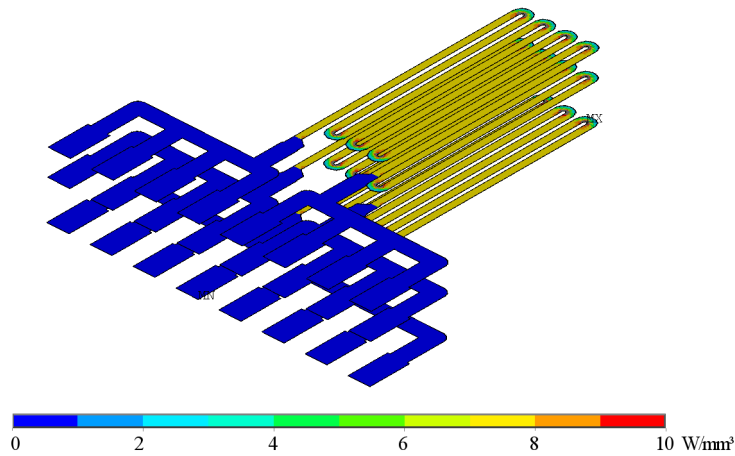


FIGURE 4.17: Power loss density of the meander with an operating voltage of 12 V.

**Method A: Step-by-step lamination**

In order to ensure proper lamination of all layers a complex step-by-step lamination process had to be developed in order to avoid damaging of the channel structure on one hand but also to achieve sufficient adhesion between the layers on the other hand (figure 4.19). No problems occurred during the pre-lamination steps. Figure 4.20 shows the pre-laminated layers inside the press form before final lamination. During the final lamination the module was deformed. Both top and bottom surface in the heater section bulged into the fluid chamber. The heating resistors and temperature sensors were distorted and resistance values differed by a factor of 5. The channel cross section depends on the lamination pressure as can be seen in figure 4.21 after sintering. A reduced lamination pressure leads to a less deformed module but also to delamination as the lamination pressure is $24 \, \text{N} \, \text{mm}^{-2}$. It was not possible to reduce the lamination pressure far enough to achieve an undeformed but well laminated module (figure 4.22). From this investigation it becomes obvious that the use of sacrificial filler cannot be
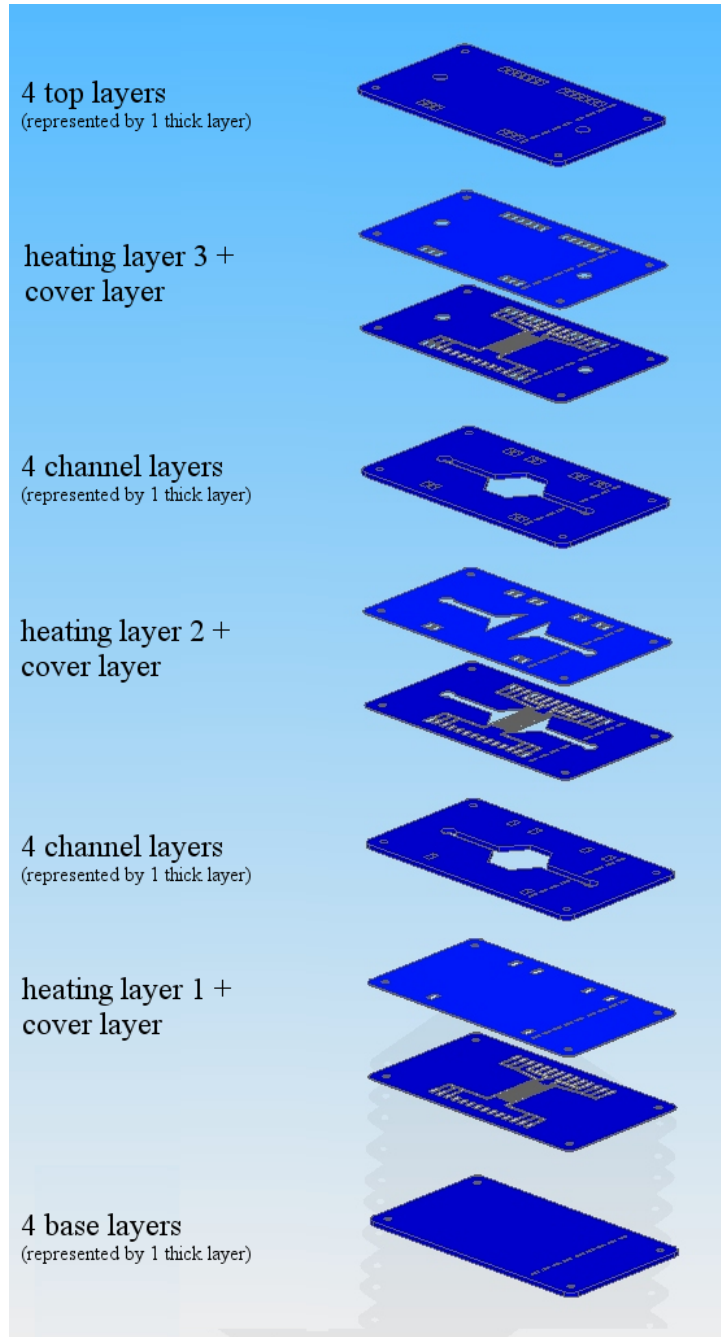
FIGURE 4.18: Layer stackup for continuous-flow LTCC heater module.

avoided and that a particular fabrication process had to be developed to cope with this deformation problem.

**Method B: Single step lamination with sacrificial material filling**

Because the pressure distribution inside the module during lamination is severely distorted by the cavities, a lamination process with sacrificial material had to be developed.
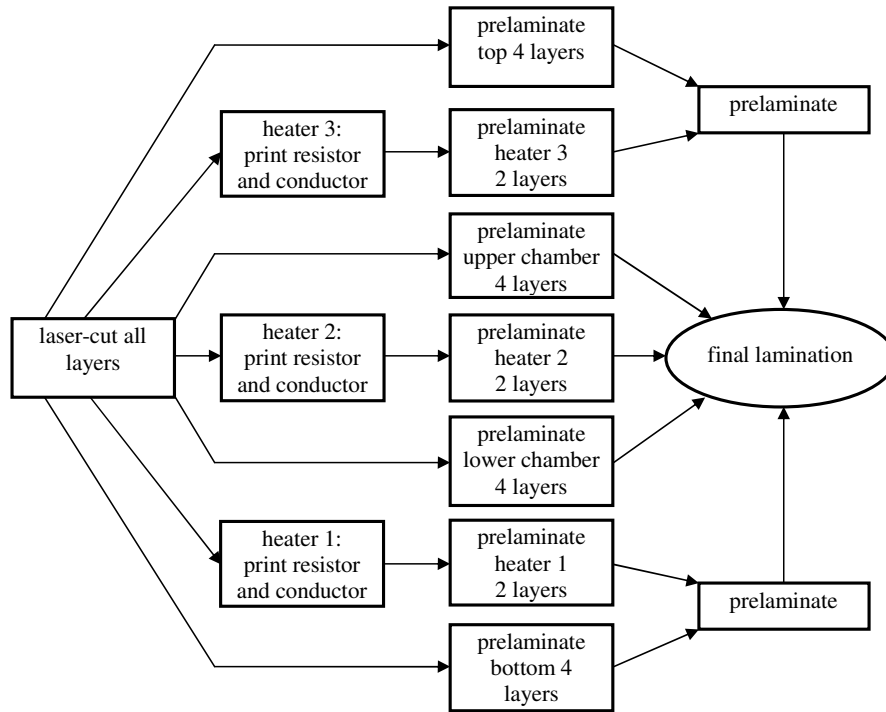
FIGURE 4.19: Lamination procedure for continuous-flow LTCC heater module.

The principle of using a filling material during sintering that evaporates or burns off during firing was successfully applied by Bruno Balluch et.al. [31, 34]. However, the use of powder or liquid material is limited when it comes to narrow cavities or high aspect ratios. It cannot be guaranteed that the material will settle equally well throughout the channel system. Especially powders can clog the channels during filling and a homogeneous filling is impossible. Furthermore the particles can be easily distributed between the tape layers if the layers are not properly clamped which is impossible for structures like bridges inside the channel. For this reason, PMMA tape in similar thickness as the LTCC tapes structured by laser cutting was considered. Another readily available material is polystyrene. Both materials where evaluated as a sacrificial material. The processing of the tapes including printing was the same as Method A, but for lamination sacrificial inlays were cut with a $CO_2$-Laser (see figure 4.23) and stacked together with the LTCC tapes inside the lamination fixture. The complex lamination process was reduced to one lamination step (70 bar, 70 °C, 4 min) which gives good results after lamination (see figure 4.24). The results after firing showed that melting of the sacrificial material leads to transportation of ceramic particle in both cases - polystyrene and PMMA. At the glass transition temperature the polymer exhibits a much higher thermal expansion which leads to either rupture of the chamber or shearing of the bridge due to slight asymmetries during manufacturing of the yet unsintered stack (see figure 4.25). Investigations show that PMMA decomposition starts at 360 °C with a strong temperature
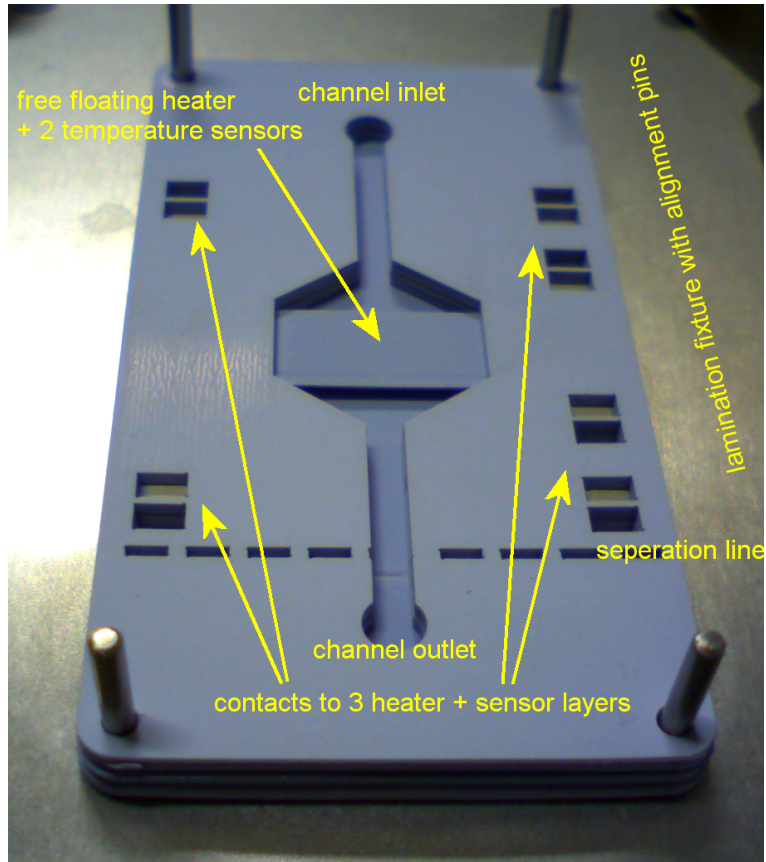
FIGURE 4.20:  Assembled pre-laminated parts of heater module before final lamination.
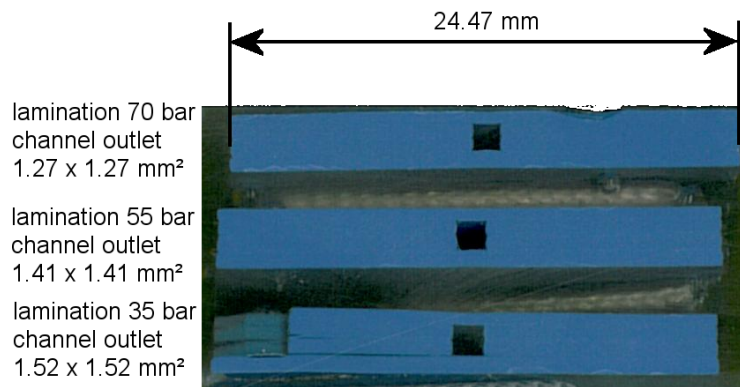


FIGURE 4.21:  Heater modules channel cross sections near outlet.

sensitivity[34].  Temperature variations of few degrees can cause excessive decomposition and pressure build-up inside the module leading again to rupture.  Boiling and decomposition during binder burn out of the polymers also caused transport of ceramic material that settles on the bottom of the channel.  If the inlay is to thick, high compression of the tape occurs in the chamber region (slightly visible as darker tape color) whereas the neighboring regions show slight delamination because of reduced lamination pressure.

FIGURE 4.22: Squashed module after lamination and sintering when using the required lamination pressure for layer adhesion.

This causes warpage of the chamber cover layers due to reduced shrinkage during sintering. The opposite is the case for samples with to thin sacrificial inlays. The color of the cover layers in the chamber region is slightly brighter than the surrounding material. The sample with the thinnest inlays already showed some wrinkle-like coloring of the cover layers which were also bent into the chamber. After binder burnout, delamination of the cover layers became obvious.

**Method C: Multi Step lamination with constrained sintering combined with adhesive**

The problem during lamination is that the free bridge sections carrying the heating meander must not be compressed a second time during the final lamination step which also leads to forcing material inward the channel. Compressing causes stretching and thinning of the conductor tracks and makes the free bridge buckling slightly during lamination. By reducing the lamination pressure and using constrained sintering layers made from alumina the main module is prevented from shrinking laterally which puts tensile stress on the bridges keeping them straight after sintering. Additionally, transparent nail paint thinned with isopropanol was used to fixate the layers before lamination. This is necessary because the heating layers are laminated to the cover layers in a separate step, but do not have any contact where the contact arrays are during the following laminations. The result showed that the constrained sintering works in principle but due to the thickness of the module the bridge experienced too much tension and the resistors had too high resistance or no contact, which can be explained by cracking of the bridge. An investigation in which only the pre-laminated blocks were sintered showed a paste incompatibility that becomes especially a problem with the low lamination pressures that had to be used.
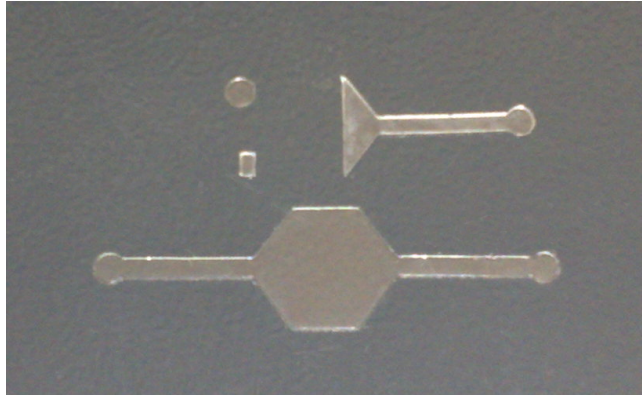
FIGURE 4.23: PMMA inlays as sacrificial material
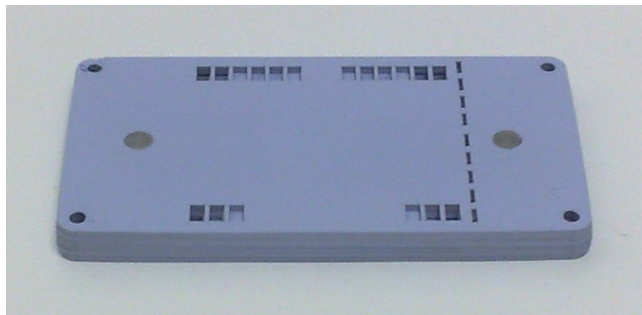


FIGURE 4.24: Heater module incorporating sacrificial material after lamination



FIGURE 4.25: Heater module incorporating sacrificial material after binder burnout

**Method D: Multiple alumina substrates bonded by glass solder**

Because the LTCC variant was very problematic when using resistor and conductor pastes inside the design an alternate approach was needed. The layout remained unchanged but the substrates made of $600\,\mu m$ thick alumina were used. The heating meander (ESL29230) and the conductor paste (ESL9695) were applied in two sequential series of printing/drying/sintering steps and the bridge heater was passivated by a glass layer (ESL4771). Figure 4.26 shows the fired separate alumina substrates, details of the meander and sensor resistors can be seen in figure 4.27. The module is finished after the sinter and final reflow cycle for the glass paste (ESL4031-B). Eventually, the method D proved to lead to a functional prototype (figure 4.28).
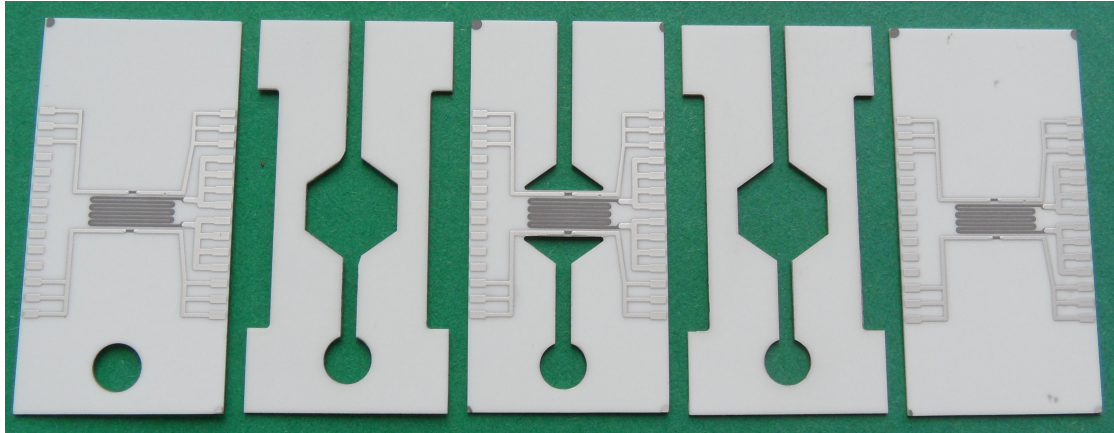
FIGURE 4.26: Alumina layers for heater module using prefired substrates.



upstream temperature sensor

heating
meander

downstream temperature sensor
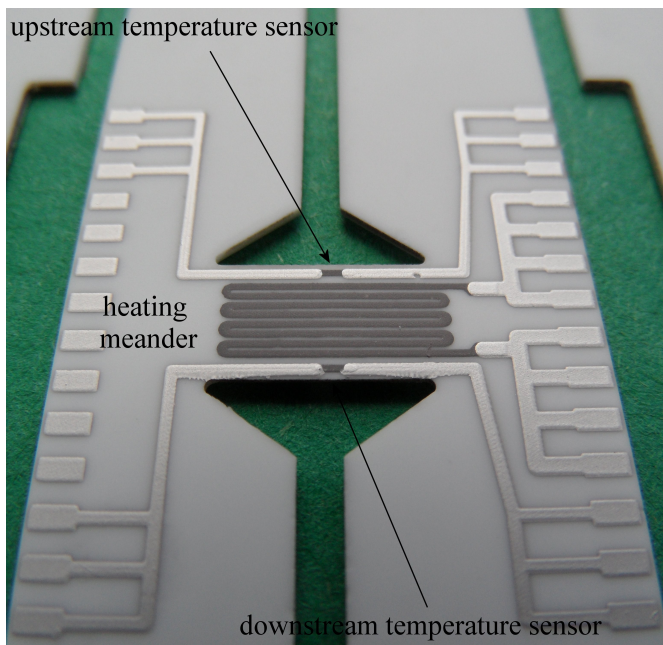
FIGURE 4.27: Heater bridge for heater module using prefired substrates.
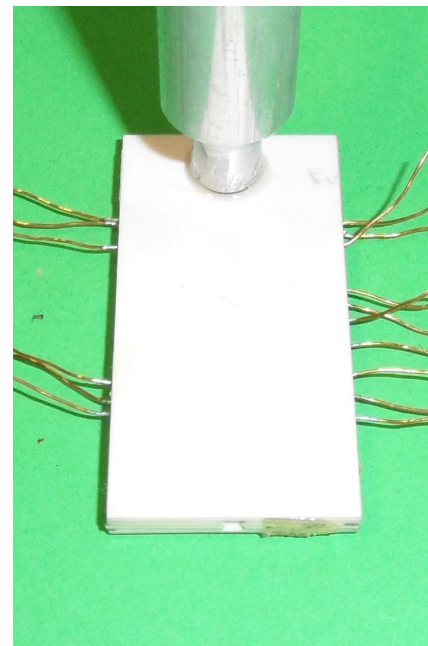


FIGURE 4.28: Module with wires and water connection.

**Manufacturing summary**

The original goal of using LTCC technology and only $80\,\mu m$ thick layers could not be achieved. Instead, $240\,\mu m$ thick tape had to be used because of excessive sagging and tearing of the bridge. This is a disadvantage at higher power densities, which are required for higher flow rates. A strong temperature gradient inside the bridge can lead to mechanical stresses in addition to the forces created by the flow resistance and system pressure that leads to structural failure. Due to paste incompatibilities and problems with sacrificial material, a satisfying prototype could not be realized in LTCC technology although dummy samples without electrical functionality suggested otherwise. By using

alumina substrates (method D) combined with a low-temperature-firing glass paste a working prototype was obtained.

### 4.2.3 Verification measurement

Because the most important property of the flow-through heater is the temperature distribution in the fluid cross section, a measurement method had to be developed to assess the quality of the temperature profile. The temperature inside the fluid is not easily accessible and can hardly be determined by observation from outside. The temperature dependence of a fluorescent dye has been used for temperature measurement [35]], but the set-up for the optical measurement is rather complex.

Therefore, a type-K micro-thermocouple was made of two $50\,\mu m$ thick wires (Ni-NiCr). The small wire diameter is necessary in order to prevent excessive distortion of the temperature profile or fluid flow. These wires are very thin and without further reinforcement, unpredictable motion in the streaming fluid may result. An epoxy-coat was successfully applied strengthening the wires and forming a sharp needle-like probe that could easily be operated inside the fluid stream (shown as detail view in figure 4.30). The probe was moved by a stepper motor positioning system while measuring the temperature with a synchronized data acquisition system in a pre-programmed zigzag pattern. By using a sync signal from the CNC control, the sampling for the measurement is easily synchronized to the motion of the probe. Figure 4.29 shows the schematic for the veri-



FIGURE 4.29: Verification measurement schematic for the flow-through heater.

fication measurement of the flow-through heater and figure 4.30 an image of the actual measurement setup. The pump a) feeds water from reservoir b) into the heater module c). On each heater layer, a resistor $R_{IN}$ and $R_{OUT}$ are used to measure the temperature

at the upstream and downstream region immediately before and after the heater. The latter is shown as heating resistor $R_{HEAT}$, the index number denotes the corresponding layer. The fluid leaves the module and passes a thermocouple e) that is positioned using a CNC system d). The reservoir temperature is monitored by another thermocouple f). The module was mounted vertically on a rail by means of a tube adapter, which was glued to the module using epoxy. The adapter is connected by a silicon rubber hose to a brushless-DC pump. For the measurement, the pump was adjusted to the desired flow rate and checked again after the measurement. The heater voltages $U_{HEATER1,2,3}$ are manually adjusted to match the input powers obtained from the simulation. Figure 4.31
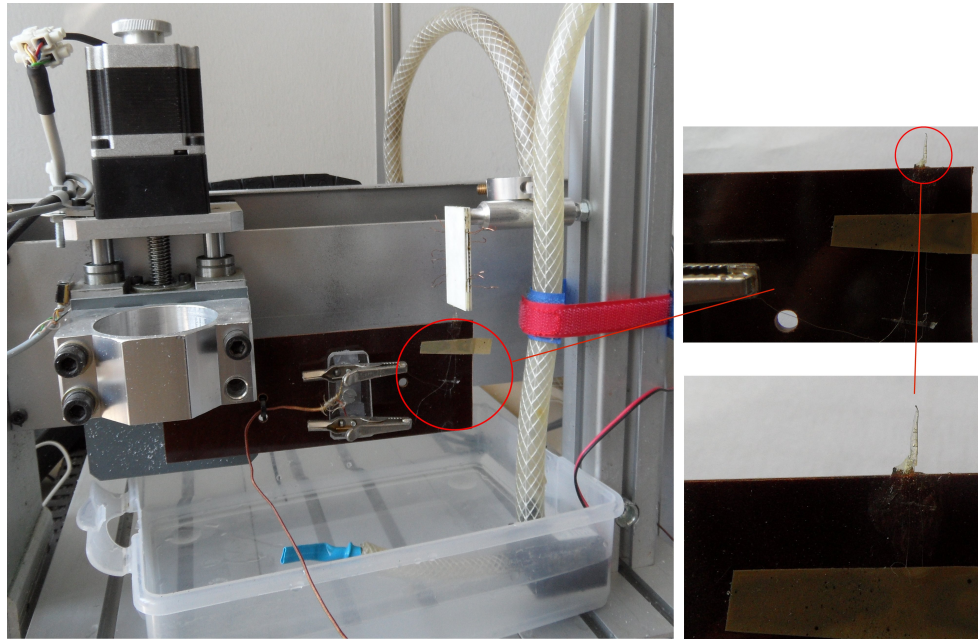


FIGURE 4.30: Verification measurement setup.

shows the simulated and the measured temperature profile in comparison, table 4.3 summarizes the corresponding resistance and temperature values all of which are in perfect agreement with those verified by the measurements. Several deviations are noticeable because of the slight misalignment of the ceramic layers that have a large impact on fluid flow and the temperature distribution. The measured temperature distribution shows that the maximum is broader than predicted by the simulation. This has two reasons: the water wets the sensor even outside the cross section of the fluid channel and makes the peak appear broader. However, the asymmetric fluid flow also increases the temperature and does indeed broaden the maximum. The temperature minimum in the center of the channel is also broader and deeper, which should not be the case. The reason for this deviation is most likely the different layer thickness of the glass solder with possible air gaps that allow the water to flow in a not enough precisely predictable way.

a)



b)
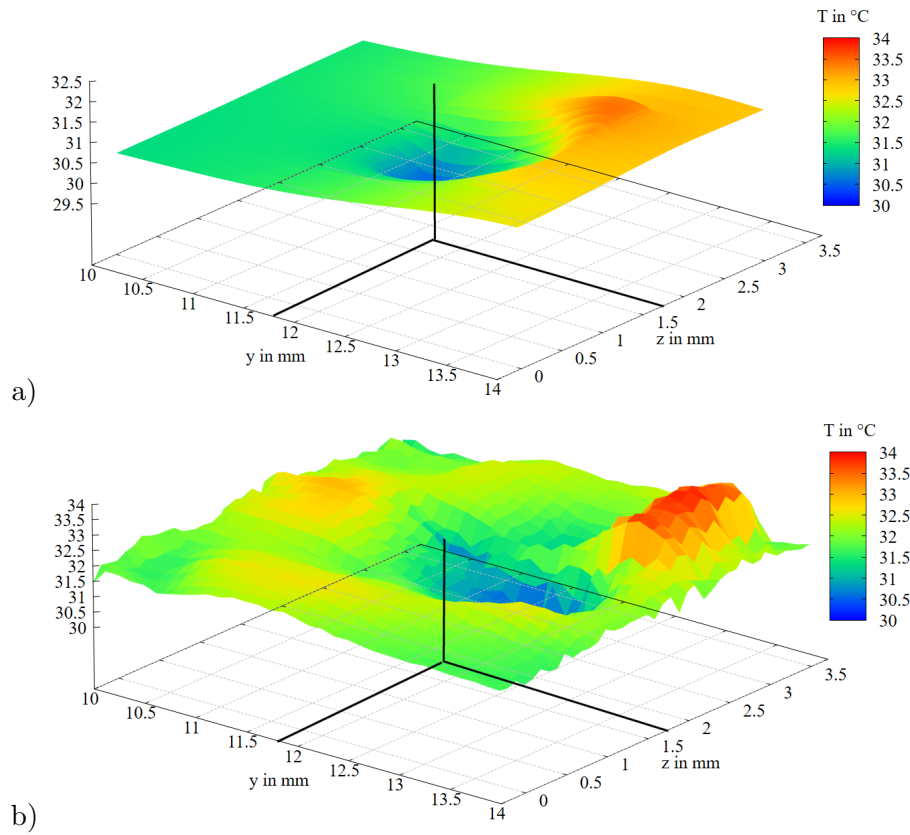
FIGURE 4.31: Simulated (a) and measured (b) outlet temperature profile: $P = 3 \times 4\,\mathrm{W}$ and $\dot{V} = 20\,\mathrm{ml}$. ($y$ denotes the width koordinate of the module and $z$ the height.

| Layer | Resistor | Value $\Omega$ | TCR $ppmK^{-1}$ | Temperature | |
|---|---|---|---|---|---|
| | | | | measured °C | simulated °C |
| | $R_1$ | 0.95 | 2830 | 26.8 | 27.1 |
| 1 | $R_2$ | 1.02 | 2870 | 40.9 | 41.3 |
| | $R_H$ | 52.3 | 3360 | — | — |
| | $R_1$ | 0.98 | 2841 | 24.9 | 25.1 |
| 2 | $R_2$ | 0.97 | 2846 | 34.0 | 34.2 |
| | $R_H$ | 49.6 | 3339 | — | — |
| | $R_1$ | 0.99 | 2851 | 27.0 | 27.1 |
| 3 | $R_2$ | 0.95 | 2856 | 42.0 | 41.3 |
| | $R_H$ | 52.2 | 3350 | — | — |

TABLE 4.3: Resistors of flowheater for each layer and their corresponding measured and simulated temperature where applicable.

## 4.3   Summary

The FE-analyses showed that it is possible to design a continuous-flow heater and obtain a homogeneous temperature profile at the outlet. For a high flow rate, the velocity profile inside the channel must be taken into account as the heating resistor structure has to be matched to the flow profile and the resulting heat removal in lateral direction perpendicular do the flow. The simulation results show that the current simple design is able to heat water at a flow rate of $5\,\mathrm{ml\,min^{-1}}$ to the desired temperature.

The study of the manufacturing process revealed that before a stable ceramic continuous-flow heater can be realized in LTCC technology, it is important to evaluate sacrificial material like PMMA as filler. Care must be taken that the filler does not influence the properties of the fired conductor and resistor traces inside the structure due to wash-out of the paste and LTCC binder and particle transport. A frame to stabilize the structure and achieve a homogeneous pressure distribution inside the structure during final lamination is necessary as well as to find a compatible paste system for the given application that does not need high compression.

The contingency set-up using alumina substrates that were bonded with glass-paste proved a viable option. However, the manufacturing tolerances of the different flow cross sections lead to a small difference in flow profile and an unforeseeable distortion of the temperature distribution. This would also be true for the LTCC module and, therefore, this type of flow-through heater is hard to realize for temperature sensitive applications. This means that the overall design might seem feasible during simulation when all dimensions are perfect, however, severe problems in flow stability and heat transfer, especially for higher flow rates, might appear. It can be concluded that the design can be used for the intended application but for creation of a precise temperature profile a lot of work has to be done regarding material selection, process optimization and the design of the structure itself.

As the design was first created inside a PCB-layout system the geometry data had to be transferred to the ANSYS simulation environment. The attempt to use the exported layout inside SolidEdge to create the 3D-model and further process it in ANSYS-Workbench or ANSYS-Mechanical failed during gluing of the separate volumes. It proved rather difficult to combine very thin layers that represent electrical screen-printed parts of the module with the larger fluid layers. Additionally, automatic geometry correction due to keypoint mismatch caused by round-off errors leads to distorted and damaged geometry itself. These hard-to-detect errors not only make it difficult in case of a simple model like

the flow-through heater but the work involved processing highly complex data like multilayer PCB files is simply impossible. A novel method with a data reduction algorithm was especially developed for such cases, which is presented in the next chapter.

# Chapter 5

# PCB and LTCC Layout Design and Data Transfer

The functional blocks of microfluidic systems can be defined as components in a CAD-package like Graffy-Hyde (optimized for LTCC design) or similar tools like PCAD, ORCAD, EAGLE, Zuken etc. as schematic parts. The components in the actual PCB-design can be defined on a per-layer basis where cutouts for channels, resistors, connectors and conductor lines are located. Additionally sub-circuits such as amplifiers and heater drivers and even micro-controllers can be included. The transfer between a PCB-Layout system that is used for PCB and LTCC design is usually possible for low complexity cases via a DXF-format. Advanced packages also allow the export as 3D-geometry with additional parts like housing and mechanical components e.g. screws. If the substructures are created as 3D-Geometry directly from the Layout system or an external CAD-package like SolidEdge, a direct translation into a FEM-model is usually performed, however unexpected problems can occur. For instance, the combination of very thin geometry with long and short structures at the same time can lead to failure when "gluing" the volumes or minor round off errors in floating point values lead to an automated repair of the geometry that actually destroys the model. When a complicated layout is imported, it is not unusual that several thousand sub-volumes are created. Because of the high number of entities, it is impossible to check for errors in the resulting geometry, often because the errors are introduced not directly during import but rather before the meshing starts. If the layer count and number of details get too high it becomes problematic to create a correct mesh within a reasonable amount of time. In addition, the dielectric which is created by a Boolean operation from the copper structures and embedded components takes a high computational effort and only feasible for very simple structures.

The processing of the 3D-model when imported into the ANSYS environment can be performed in two ways:

a) Every volume is meshed separately and special contact/target pairs of 2D-elementsare are created to couple the elements. This means that coupling coefficients must be calculated before the solver run and fields are interpolated across the sub-component boundaries; a step that leads to loss of precision. However, the meshing can be performed in parallel and is very fast. By choosing an appropriate mesh size, the loss of precision can be controlled, but this technique might not be applicable for a multiphysics simulation where the results (Joule losses in temperature dependent electrical simulation and temperature field of the fluidic simulation) are transferred.

b) "Gluing" of the volumes where surfaces are touching, they are united to form shared areas and assure a continuous mesh. This guarantees high precision because a detailed mesh can be generated in critical areas and this can be done mostly fully automatic. The algorithm performing this task might not have problems if the key points are exactly the same but fails when minor deviations of the coordinates are present.

Additional to the above-mentioned problems, special licenses or additional software might be required to read the design data (eg.g ANSYS ICEpak, NETEX-G). Even if it is possible to read the data in one software module, it is not necessarily easy or possible to use it in a different module or software package without any problems. Therefore, an existing thermal simulation tool named TRESCOM (originally developed at the Institut für Werkstoffe der Elektrotechnik, TU Wien [33], further developed by Gernot Hanreich and Martin Mündlein) was used as basis to create models of real world layouts of arbitrary complexity by processing layer data into voxels (finite volume modeling with orthogonal grid). One particular feature of TRESCOM is that a model is created by assigning a distinct, user defined, color to each voxel representing one distinct material. In this way complementarity of all material filled volumes and heat transfer coefficients between them are provided automatically.

## 5.1   Data conversion and model creation

The most basic method to transfer model data as for instance generated by a CAD program is to use a voxel representation of the model using bitmaps in conjunction with the most common output routine that is available in all software packages: the printing function. By utilizing either PostScript or PDF as intermediate format and GhostScript® to create the bitmaps with a given resolution a voxel representation can be easily created where the chosen resolution sets the obtainable detail level and the

color represents the material. Because the bitmaps are rather large, in the frame of this PhD-Work the TRESCOM source code had to be greatly modified to accommodate for the higher data volume in both the computation part and the display part of physical model and results. Also the solver was changed from a SOR(successive over-relaxation)- to a Red/Black parallelizing SOR algorithm using a 64 Bit-compiler. While the data transfer is now straight forward, fine details with comparatively large models lead to excessive model sizes and memory consumption, which raises the need to find some method of reducing the model size.
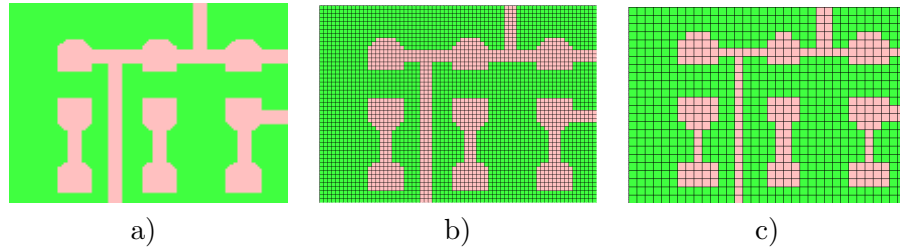


FIGURE 5.1: Rasterization of pads and copper tracks at different resolution: a) 20 µm, b) 40 µm and c) 80 µm.

Figure 5.1 shows a part of a PCB conductor structure rasterized as bitmap at different resolution. It can be clearly seen that the circular shape has been degraded into a classical chunky form that will cause problems in certain situation where the correct shape is important such as high frequency applications but also mechanical or fluidic applications. For thermal or electrical simulation, it is enough that the cross-sections equivalent. If the error made is too large, a finer rasterizing grid has to be chosen. A simple mesh can be directly generated from the voxel data by using the size and coordinate information to write out a node list and an element list for ANSYS. It becomes clear immediately that the orthogonal grid representation which needs an x, y and z-size information scales with $3 \cdot n$ while the node coordinates are stored with $n^3$ memory consumption. A representation with 2D-shell elements, which store layer information internally, might be possible in some cases where each 2D-element represents a column of the model. Unfortunately, this cannot be used in conjunction with fluid simulation.

Furthermore, TRESCOM only allows thermal simulation without any electrical, mechanical or fluidic computation. To address this shortcoming, an export routine for ANSYS was developed that allows reducing the model with a selectable coarsening factor. In order to compare the effectiveness of the conversion procedure and the data reduction algorithms three different models were chosen:

a) a simple $D^2PAK$ compatible package of a Schottky double diode,

b) an LTCC flow-through heater and

c) a highly integrated camera module with embedded passives as well as ICs and additional SMT components on both sides of the PCB.

Figure 5.2 shows the three different models that were used as 3D view created in the in-house tool TRESCOM. The test models have different characteristics making it necessary to use different resolutions for rasterization, which leads to unacceptable high memory consumption. Table 5.1 lists the key features such as vias count, size and number of layers as well as the necessary resolution. It is evident that especially the camera module (c) has an enormous memory consumption but also the other models result in a large model. To reduce the data size two methods were investigated: a simple combination of adjacent slices (x-z and y-z- planes) with equivalent material stacks and a recursive cell-enlargement algorithm[36].



a)                                    b)                                    c)
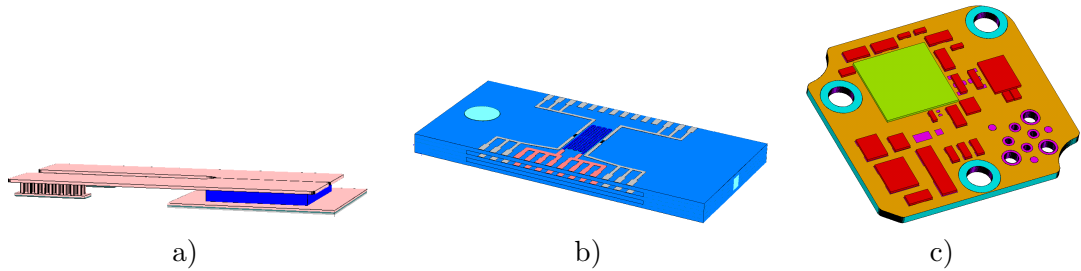
FIGURE 5.2: 3D-view of the test models:
a) D$^2$PAK compatible package, b) LTCC flow through heater, c) camera PCB.

## 5.2 Coarsening by equal slice search and merge

Due to the necessary high lateral resolution, the memory consumption and computation times needed for processing models with high spatial resolution might be quite large. If a model has large areas without any material change, an appreciable reduction of lateral discretization steps can be achieved by searching for equal slices of the model in the x-z- and y-z-planes. The same method could be used for x-y-slices but as the model is layer based, it has already the optimal discretization in vertical direction. If equal slices are found, they can be replaced by a slice with their combined width. This approach is simple and easy to implement (figure 5.3) but an excessive use of this function will create elements with large aspect ratio. As can be seen in figure 5.4 using the D$^2$PAK model as example [37? ], the reduction has already reached the aspect limit and cannot be reduced by a maximum possible factor of 7.75 (table 5.1). The reason are the vias within the stack that enforce a very fine resolution in the corresponding areas. Furthermore, geometry angles different from 90 degree cause a poor slice matching leading to unsatisfactory coarsening. This effect poses a significant limitation of this approach, which is especially unsuited for the camera PCB [38]. For

such cases a second meshing and coarsening process was developed that can overcome these shortcomings.
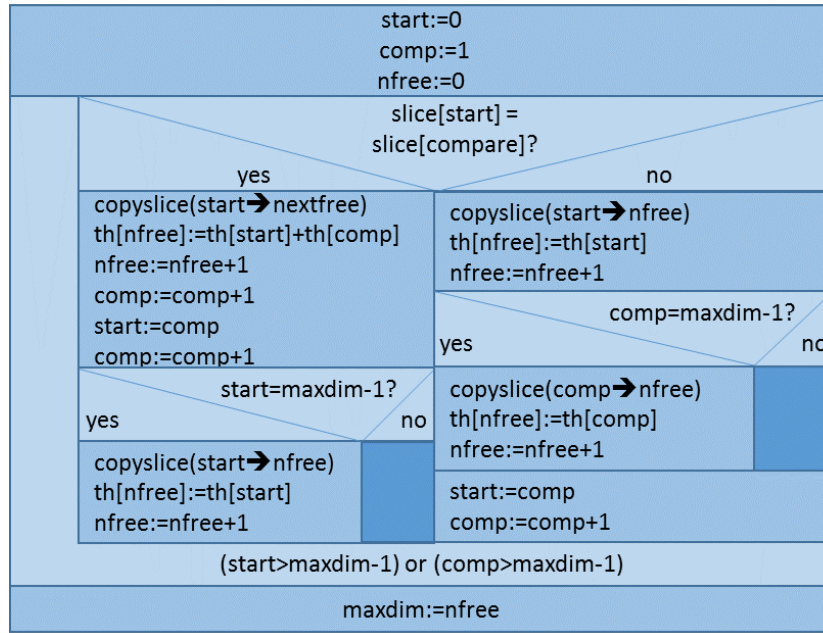


FIGURE 5.3: Slice combining algorithm.
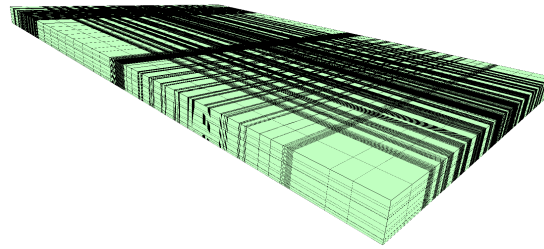


FIGURE 5.4: External view of D$^2$PAK compatible package model with bad reduction at package edges due to internal fine structures.

## 5.3 Cell reduction recursive enlargement

For an effective coarsening of the model, the method works in three main steps:

a) Column type search

A column represents the local material sequence in vertical direction. The first stage is to create a column type matrix (CTA) in which the column types are stored. The model is traversed beginning at x=0; y=0 and the current column is compared to all other columns. If a match is found, a 32 Bit column type number is written to the CTA and the column marked as "processed". The column type number starts at 0 representing empty columns and is increased by one for each new column type. The first non-matching

| Model | Features and size | cell count |
|-------|-------------------|------------|
| D$^2$PAK package | $4.5 \times 5.4 \times 0.15\,\text{mm}^3$ chip, 88 of $150\,\mu\text{m}$ vias, 12 layers | 18.6 M (2.4 M) |
| LTCC Flow heater | $50 \times 255 \times 3\,\text{mm}^3$ total size, fluidic channel, three $12\,\mu\text{m}$ thick heating meander structures | 32 M (7 M) |
| Camera PCB | 11 copper layers, 10 dielectric layers, embedded and SMT passives + chips, $22 \times 23 \times 0.8\,\text{mm}^3$ total size, extremely high complexity | 36.7 M (36.7 M) |

TABLE 5.1: Number of cells for the three test models after import and minimum number after slice combining.

location is also remembered for the start of the next loop. The next loop is started with the next unprocessed column until all columns have been processed. The procedure is shown in Figure 5.7a as Nassi-Shneiderman-diagram. The column type number can also be used to create layered shell elements for ANSYS later on if desired. The 3D-model is reduced to a 2D-representation similar to a top-view X-ray image where the material sequence in perpendicular direction (z-direction) is considered.

If only a PCB without any components is considered, each layer can be composed locally of FR4 material or copper which can be represented as 1 Bit. If all permutations occur, the maximum expected bit count needed to store the column type is equal to the number of layers. This means, that a 50 layer model would already consume 50 bits of the count variable, however as the horizontal resolution of the model is limited to $< 65535$ cells (16 Bit) in x and y direction each, a total of 4 Gibi ($4 \cdot 1024^3$) permutations are possible no matter of how many materials are actually used inside the model. Therefore, a 32 Bit variable is sufficient to store the column type.

b) Reduction

In this step, a search is performed for locations that have the same column type numbers. Based on the equality of neighboring columns, points in between are marked where potentially a higher order element can be created. Figure 5.5a shows the original representation with filled circles where the color represents two different column types. In the first iteration, each junction between 4 adjacent cells is marked if those cells have the same column type. Figure 5.5b shows the larger cells that have been created. Cells that have been altered are filled with corresponding color; unchanged cells are marked with filled circles. Those elements that can be used to create larger elements have been left white and marked accordingly. One drawback that can be already observed is that

some original sized cells have been cut in half while a bigger cell has been created. However, this guarantees a finer resolution at critical areas like vias with strong heat flux or current density. Figure 5.5c shows the newly created cells where again some cells have been cut in half into triangles. All nodes that are surrounded by higher order elements can now be marked in the following iteration – Figure 5.5d shows one final mark with no further possibilities. Because the marks are placed where an output is required, the marks must be placed in such a manner that no overlapping cells are created. In Figure 5.5b a mark could be created right below the first mark but this would cause overlapping cells. In general no mark above or below, left or right of the considered location must be placed in even iterations. The distance for mark exclusion is given by iteration number $2^{\text{Iteration-1}}$ as this would create overlapping cells.



| a) | b) | c) | d) |
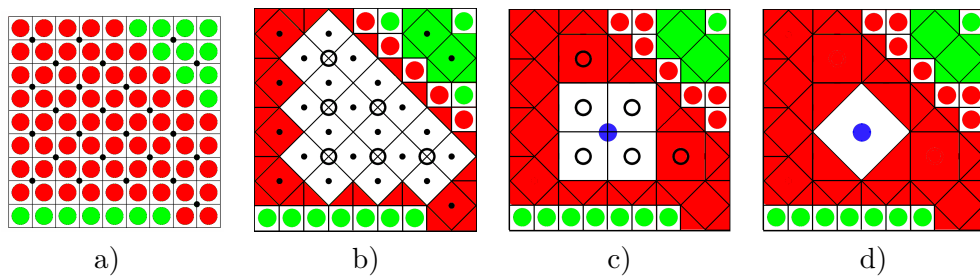
FIGURE 5.5: Cells of the current size with markings for the next size increment:
a) original representation, b) $2^{\text{nd}}$ size, c) $3^{\text{rd}}$ size and d) $4^{\text{th}}$ size elements.

A similar situation is in figure 5.5c where diagonally no marks must be placed; the top and bottom locations are also forbidden but are automatically excluded by the previous markings determined by the algorithm. For each iteration, the resulting higher order elements have $\sqrt{2}$ of the side length and twice the area of cells from the previous iteration. This principle can be continued until no more coarsening is possible or the maximum desired level of coarsening is reached. In order to store the markings efficiently a bit mask matrix is used where each bit represents a mark for each coarsening level and a single "1" starting from the LSB is shifted left for each iteration. This part of the algorithm is shown in Figure 5.7b and c. Table 5.2 gives an overview of the number of elements of increasing size for different models that can be created from the newly generated elements from the previous iteration. In this Table the afore mentioned effect can be observed where an optimum reduction is already reached with the 4th size for the camera PCB whereas, in contrary, the flow heater and D$^2$PAK models show that a significant amount of the elements can be enlarged even to the $9^{\text{th}}$ size and beyond. Ideally, as the element area doubles in each iteration step, the number of larger sized elements should be 50% of the previous iteration. The reason for the low reduction in cells at the camera PCB is it's high complexity as it consists of 12 copper layers with 11 dielectric layers, solder layers and embedded as well as surface mounted components and a detailed mesh is needed at many locations within the model.
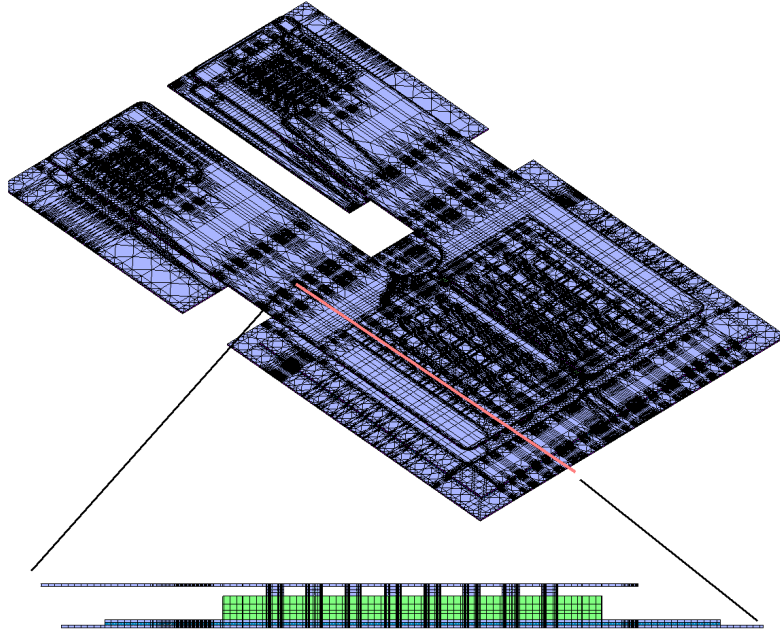
FIGURE 5.6: Inner structure of D²PAK model processed with the reduction algorithm.

c) Output

An element list is created in iterations from the array holding the markings for each element size and column type. The node numbers and coordinates are computed from the current position and size level of the current iteration. Elements that touch a higher order mark are cut in into triangles, elements that touch more than one mark are discarded (figure 5.7d). At the end, a complete model file is created with the smallest elements written first and the largest last. For practical reasons the software creates an ANSYS input file containing the material properties for the simulation, node and element lists, power losses and boundary conditions as well as solver commands. Post processing is automatically performed to display the temperature distribution.

| Iteration | D2PAK | Flow heater | Camera |
| --- | --- | --- | --- |
| base size | 1551875 | 1690956 | 1360216 |
| 2nd | 752999 | 813839 | 463212 |
| 3rd | 355032 | 374703 | 128461 |
| 4th | 164200 | 168791 | 34919 |
| 5th | 74668 | 74493 | 9020 |
| 6th | 33890 | 32823 | 2239 |
| 7th | 14613 | 14288 | 555 |
| 8th | 6147 | 6190 | 224 |
| 9th | 2486 | 2521 | 99 |

TABLE 5.2: Number of enlarged cells for the three test models that can be created from the previous iteration.

**a)**

CTA: Column Type Array 32bit integer
VVect: Vertical material vector

init CTA all 0x80000000
init VVect all 0
startx:=0; starty:=0;
nextstartx:=0; nextstarty:=0; actcol:=0;

change:=false

j:=starty to maxy-1

i:=startx to maxx-1

CTA[i,j] AND 0x80000000 <>0 ?

yes | no

Vect=Model[i,j]? | change?

yes | no | yes | no

CTA[i,j]:=actcol | | | nextstartx:=i
nextstarty:=j
change:=true

startx:=0

Model[nextstartx,nextstarty]➜VVect
actcol:=actcol+1
starty:=nextstarty
startx:=nextstartx

((startx>=maxx-1) and (starty>=maxy-1)) or not change

**b)**

redstatistic array: stores number of cells per level
levelflags: array holding the marks for larger cells
dc: search distance from the current position

level:=0; levelflags initialize all 0

redstatistic[level]:=0

level=0 ?

yes | no

dc:=0 | dc:=1 << (level >>1)

j:=dc+1 to maxy-1-dc

i:=dc+1 to maxx-1-dc

checkmark(i,j,level) ?

yes | no

levelflags[i,j] :=levelflags[i,j] or (1 shl level)
redstatistic[level]:=redstatistic[level]+1

startx:=0

level:=level+1

(level=maxlevel+1) or (redstatistic[level-1]=0)

**c)**

function Checkmark(a,b,level): checks at location a,b and for current level if a mark should be set.

result:=false
currentmark:=1 << level
previousmark:=1 <<(level-1)
distance dp:=1 << ((level-1) >>1)
dc:=1 << (level >>1)

| level | | |
|---|---|---|
| even | odd | 0 |
| previous mark in levelflags @[a-dp, b] AND @[a+dp ,b] AND @[a, b-dp] AND @[a, b+dp] and no current mark in levelflags @[a-dc, b-dc] OR @[a+dc, b-dc] OR @[a-dc, b+dc] OR @[a+dc, b+dc] then result:=true | previous mark in levelflags @[a-dp, b-dp] AND @[a+dp, b-dp] AND @[a-dp, b+dp] AND @[a+dp, b+dp] and no current mark in levelflags @[a-dc, b] OR @[a+dc, b] OR @[a, b-dc] OR @[a, b+dc] then result:=true | if CTA[a, b ]= CTA[a, b-1]= CTA[a-1, b ]= CTA[a-1, b-1] then result:=1 |

**d)**

output base size elements

j:=0 to maxy-1

i:=0 to maxx-1

levelflags[i,j] <>0 and not CTA[i,j]=0?

yes | no

n_marks:=Sum of marks in levelflags@ [i, j], [i+1, j], [i, j+1], [i+1, j+1]

| n_marks | | |
|---|---|---|
| 0 | 1 | >1 |
| write elements[1] as block (8 nodes) | write elements as wedges (6 nodes)[1]: levelflags<>0@ [i, j]: lower right [i+1, i]: upper right [i, j+1]: lower left [i+1, j+1]: upper left | no output |

level:=0

j:=0 to maxy-1

i:=0 to maxx-1

mask:=1 << level
nextmask:=mask << 1
distance dc:=1 << (level >> 1)

levelflags[i,j] AND mask<>0 and not CTA[i,j]=0 ?

yes | no

n_marks:=Sum of marks for current level (levelflags[a, b] AND nextmask)@

level EVEN:
  [i-dc, j], [i+dc, j], [i, j-dc], [i, j+dc]

level ODD:
  [i-dc, j-dc], [i+dc, j-dc], [i-dc, d+dc], [i+dc, d+dc]

| n_marks | | |
|---|---|---|
| 0 | 1 | >1 |
| write elements[1] as blocks (8 nodes) | write elements as wedges (6 nodes) where levelflags AND nextmask<>0@ level EVEN: [i-dc, j-dc]: top right [i+dc, j-dc]: top left [i –dc, j+dc]: bottom right [i+dc, j+dc]: bottom left level ODD: [i-dc, j]: right [i+dc, j]: left [i, j-dc]: top [i, j-dc]: bottom | no out-put |

level:=level+1

(level=maxlevel+1) or (redstatistic[level-1]=0)

[1] the node index is calculated for the elements as follows where k is the layer number:

nindex:=k*(maxx+1)*(maxy+1)+j*maxx+1+i+1

base elements: [i, j], [i+1, i], [i, j+1],[i+1, j+1]

level EVEN:     [i-dc, j-dc], [i+dc, j-dc], [i –dc, j+dc], [i+dc, j+dc]

level ODD:      [i-dc, j], [i+dc, j], [i, j-dc], [i, j-dc]

FIGURE 5.7: Reduction algorithm: a) cell type search, b) marking of possible larger cells, c) mark decision function and d) cell output.

88

## 5.4 Results

a) Reduction in memory consumption

The algorithm makes it possible to easily create complex models and reduce the model data significantly as table 5.3 shows. Even for models that do not allow a great reduction in element and node count it is possible to use layered elements (shell-elements) and obtain at least a drastically reduced database size. The memory required for the solver remains unchanged because the number of unknowns stays the same.

b) Influence on simulation results

The $D^2PAK$ diode model created in SolidEdge and meshed in ANSYS Workbench was compared to an equivalent model created by the reduction algorithm. Thermal and electrical simulation showed no significant difference. Fine details are preserved where a change of materials occurs anywhere inside the model which is beneficial for via to copper plane connections. If the vertical resolution has to be increased too, only the whole layer can be split. Automatic mesh refinement based on different criteria might not be possible in general. The algorithm mesh convergence is not automatically obtained and has to be checked by using different resolutions. Especially when using mechanical simulations the jagged contours of round features can create stress risers and require an even higher resolution.

| Model | as imported | slice combining | selective coarsening |
|---|---|---|---|
| $D^2PAK$ package | 11.0 GB | 1.4 GB | 1.6 GB(271 M) |
| LTCC Flow heater | 16.8 GB | 1.5 GB | 3.0 GB(156 M) |
| Camera PCB | 19.4 GB | not applicable | 14.3 GB(1.1 GB) |

TABLE 5.3: Reduction method and database size as ANSYS model with Solid70(Shell131) elements.

c) Computation time

Considering all steps in model creation, meshing and solving a significant reduction in time can be achieved when processing a large number of geometric objects. Because a continuous mesh is created, no contacts or interfaces need to be considered and while the algorithm might not be optimal for all cases, the ease of use of the program can help reduce manpower. Extending this algorithm to 3D mesh generation is possible but the selective coarsening approach might require prohibitive amounts of memory.

A further improvement could be achieved by including the original associative geometry information. This would be beneficial for automated mesh morphing in ANSYS, but such a method requires the processing of the original vector data.

# Chapter 6

# Conclusions and Outlook

The main motivation for this work was to show that intelligent modular design of microfluidic modules is possible and by designing appropriate heater structures, an existing microfluidic system can be further miniaturized. The power requirements are comparatively low and allow the use in mobile appliances.

a) Design method

The investigations showed that a trial-and-error approach is not only time consuming but also not feasible due to the unpredictable settling time. By implementing a design rule, an automated heater design is possible where not only a desired temperature profile is reached after a desired time but also the profile itself exhibits no transient overheating. This means the whole temperature distribution is synchronous during transients, which is important for simplified temperature regulation using only one reference point for temperature measurement and only one control loop. This design method also limits mechanical stresses, which are caused by CTE-mismatch of the materials and the occurring temperature gradient. For practical reasons, alternative methods like parameterizing a meander or fence structure is more convenient because the structure is less susceptible to manufacturing flaws like pinholes during screen-printing.

b) Temperature profile homogeneity and settling time

The results obtained with the development of a measuring prototype show clearly that it is possible to design stable temperature distributions with a profile flatness better than $100\,\text{mK}$ over the critical section. The heat-up period can be made sufficiently short and the realization as thick film module with a plastic lid is feasible staying compatible with existing components. From experience, it is also possible to realize such a module completely in LTCC technology, whereas the application of the enzymes into the channel have to be done by pipette and a lid has to be used separately. LTCC technology has the

advantage over thick film technology as it is a 2.5D approach and it is easy to integrate fluid channels as well as sensor structures together with the heating resistors.

c) Flow-through heater

The flow-through heater was meant to increase the regulation speed of the system as well as to serve as a study object for the implementation of high-temperature-capable structures such as heating fins for chemical applications. A flow-through flow heater allows heating the fluid to the desired temperature before it enters the critical measurement section and, therefore, lowers the settling time of the system considerably. Unfortunately, an LTCC-based heater could not be successfully implemented because the dimensions were too ambitious and mostly unforeseen problems with paste compatibility and difference in compression of the material during lamination occurred. A thick film version using alumina substrates was successfully built and a measuring setup designed to validate the fluid temperature inside the liquid. The temperature profile at the output of the heater suggests that the physical model deviates slightly from the original CAD model and, therefore, the temperature profile is a bit distorted, which is significant at higher flow rates.

d) CAD design and simulation

The application of a standard PCB design package allows using circuit symbols in the schematics editor to design the fluidic and electric circuitry simultaneously which is fundamental for an easy-to-use modular design system. The problem to transfer the CAD-data of arbitrary origin into the simulation software was solved by creating a voxel based method and reduce the data with a newly developed reduction algorithm that was successfully used during the EMPOWER and EDDEMA research projects.

e) Material characterization

Investigations of the behavior of some LTCC materials as dielectric showed significant ion conductivity at elevated temperatures as well as chemical instability where material diffusion of the conductive paste occurred. In the case of one LTCC material, even an extremely low temperature where ion conductivity became significant was found. Some materials also showed significant softening at the sintering temperature for thickfilm pastes. This is important for applying additional structures in a so-called post-fire process (sintering process after the main LTCC module has been sintered) as these tape material can suffer deformation during further sintering cycles - they cannot be considered "refire safe". Because not all LTCC tapes are available for a prolonged time, new improved materials having different composition have to be investigated regarding their mechanical and electric properties as well.

The thesis performed lays a groundwork for the design of not only ceramic based but also for PCB and silicon based layered applications. The future use for designing stacked assemblies, assemblies with embedded components, micro reactors for chemical synthesis etc. is an interesting field that is worth pursuing because high frequency, optical (embedded fibers), high temperature and high-pressure requirements can be found on an adequate multiphysical modeling-base.

# Appendix A

# LTCC-Technology, Materials and Characterization

## A.1 LTCC-Technology overview, applications and novelty uses

For a long time ceramics have been used as isolators with a high dielectric strength and low ionic conductivity in high voltage applications as well as in RF-applications [39]. Ceramics as circuit carriers were pursued because the polymers used at the beginning of electrical engineering (phenolic resin and Bakelite) were not as thermally stable as modern high-$T_g$ PCB materials and the resulting products were not sufficiently reliable. This thickfilm and hybrid technology started in the early 1960s when IBM developed modules based on a 1/2 inch ceramic wafer [40, 41]. In thickfilm technology where alumina substrates are used, the conductive and resistive areas are applied by screen-printing where every type of paste is printed, dried and fired. When using a ceramic wafer at first only single sided circuits are possible. Hole drilling (fired) or punching (unfired) makes it possible to create double sided ceramic circuits. However, the desire for higher integration densities leaded to the development of isolating pastes that allow the creation of true multilayer circuits. The main problem is the creation of so-called pin-holes that are introduced during the printing step and create a potential air void between two signal layers on top of each other. This can lead to breakdown when a high enough electric field strength is present whereby this phenomenon is not necessarily detectable during manufacturing. This leads to failures at the final inspection or after a certain time in the field. To create a solution LTCC technology was developed where the conductive and resistive paste layers are printed on unfired tapes that are dried, stacked, laminated and fired as one solid block. The following sections give an overview

of the composition and the manufacturing of LTCC modules as it is performed at our institute.

## A.2 LTCC composition and Manufacturing procedure

### Chemical composition of the LTCC tapes

LTCC tapes usually consist of a large portion of alumina, only the Ferro A6 tape fires as Wollenstite $CaSiO_3$ The Heraeus CT700/CT800 tape series uses barium aluminum silicate, the CeramTec GC and the Motorola T2000 is based on anorthite $CaAl_2Si_2O_8$[9]. The following tables give the chemical composition and phases present in the various LTCC tapes. Toskov et al. [42] investigated the chemical stability of the materials, which is crucial for chemical applications.

| Tape | Dupont 951 | Dupont 943 | Ferro A6 | Heraeus CT800 | Heraeus CT700 | Motorola T2000 |
|---|---|---|---|---|---|---|
| Phase Structure | $\alpha$-$Al_2O_3$ $Ca(Si, Al)_4O_8$ | $\alpha$-$Al_2O_3$ $(Ca)Al_2B_2O_7$ | $CaSiO_3$ | $\alpha$-$Al_2O_3$ $BaAl_2Si_2O_8$ | $\alpha$-$Al_2O_3$ $BaAl_2Si_2O_8$ | $\alpha$-$Al_2O_3$ $CaAl_2Si_2O_8$ |
| Minor Phases | | $Ca(Si, Al)_2O_8$ | $MgSiO_3$ $SiO_2$ $CaB_2O_4$ | $(Mg, Ca)Al_2Si_2O_8$ | $SiO_2$ $(Mg, Ca)SiO_3$ | $CaSiO_3$ |

TABLE A.1: Phase structures present in the laminate tapes as determined by X-ray diffraction analyzes. The major phases are listed first, followed by the minor phases[9].

| Element | Dupont 951 | Dupont 943 | Ferro A6 | Heraeus CT800 | Heraeus CT700 | Motorola T2000 |
|---|---|---|---|---|---|---|
| Al | 42 | 76 | 1.5 | 41 | 31 | 52 |
| Si | 47 | 4 | 48 | 39 | 42 | 28 |
| Ca | 7 | 9 | 47 | 2 | 5.5 | 8.5 |
| K | 1 | 0.5 | | 1 | 1.0 | |
| Mg | | | 1.5 | 3.5 | 3.5 | |
| Zn | | | | 0.5 | 0.5 | 2.5 |
| Ti | | 7.5 | | 5.5 | 6.5 | 6.0 |
| Co | 0.5 | 0.5 | | 0.5 | 1.0 | |
| Ba | | | | 3.5 | 5.0 | 0.5 |

TABLE A.2: Chemical Composition (Atomic per cent) of the fired tapes by EDS[9].

### Structuring

The sheets of unfired tape (size e.g. 8x8 sq.inch) are either punched with a specifically designed tool or drilled and cut by laser which is a more universal process without

special tooling. At the ISAS laboratory a ROFIN Solid state Nd:YAG laser is used to cut the sheets to $7 \, \text{x} \, 5 \, \text{cm}^2$ large pieces for an internal standard press-form. The cutting behavior of this specific laser was investigated by Balluch et al. [34] on several LTCC tape products. These pre-investigated parameters were used for structuring in this work.

### Screen-printing and Via-Filling

Laser cutting, via filling and screen-printing has to be performed for each tape layer. Screen-printing is done using a 30 to $50 \, \mu\text{m}$ stencil from MURAKAMI and a screen having 200 to 325 meshes per inch. Via filling is usually performed by using a stainless steel stencil and a via filling paste in the same screen-printer in which the conductors are printed. The specific via-filling paste does not flow after the printing cycle in order to fill the vias flat and reduce the chance of voids inside the laminate. In this work, only the flow-through heater in chapter 4 is LTCC based. It's design was modified using cut outs that allowed contacting the deeper layers with spring probes and no vias were needed. Each print is followed by a drying cycle at $75 \, °\text{C}$.

### Stacking and Lamination

The tape layers are stacked inside a press-form where polyethylene sheets are used to keep the LTCC material from sticking to the press-form during lamination. This polyethylene sheets are removed after lamination. Depending on the tape material rather low pressures of 30 bar up to 150 bar are necessary. In the following chapters and sections the processing parameters are given separately for the manufacturing steps. The lamination pressure plays an important role in compacting the material and changing its shrinkage during sintering. Inhomogeneous pressure leads to warpage severe deformations and rupture during sintering.

### Sintering

Sintering can be performed using a belt furnace or a box furnace in a temperatures range of 850 to $950 \, °\text{C}$ compared to $1600 \, °\text{C}$ for alumina or zirconia (HTCC). The belt furnace transports the samples on a belt and has the advantage that it can be operated continuously at very short cycle times of e.g. 30 min 3 h. The disadvantage is the inherent gradient inside along the transport direction. Therefore, the belt furnace is only suitable for rather thin and small laminates. Bigger samples - especially when sacrificial material is used - need a long burn out cycle and slow sintering process. A box furnace offers this advantage at the cost of a long cool down period. It is usually operated in shifts or

overnight. The figures below show typical sintering profiles as used for the used LTCC materials.

## A.3   Material properties

In order to construct LTCC microfluidic modules it is also important to determine the mechanical properties of the materials. The mechanical properties like thermal coefficient of expansion, Young's modulus and flexural strength are not only important for later use of the modules but are very important during manufacturing. Differences in thermal expansion and Young's modulus lead to stress, warpage and fracture in the cool-down phase during sintering or reduced durability in operation. Depending on the micro fluidic application itself, the operating temperature range can be rather low (up to 100 °C for biological modules) or in a high region for chemical syntheses. Another application is the realization of mechanical sensors in LTCC technology where usually the changes of mechanical properties along with temperature are taken into account. The investigations carried out using commercially off-the-shelf available ceramic tapes (Ferro A6, Heraeus "high k" CT765, zero shrinkage HL800, CeramTec GC) show, that the dielectric behavior can change dramatically before mechanical effects become relevant. This chapter presents the results for characterization of the different properties used for FEM-analyzes in the design phase.

### A.3.1   Thermal expansion of LTCC tape materials [1]

For examining the coefficient of thermal expansion of different ceramic materials, sample blocks with a sintered size of about 5 x 5 x 20 mm$^2$ have been prepared. For this purpose, stripes of unfired tapes were structured with the laser, stacked in a lamination fixture, laminated at the appropriate pressure and later fired inside a box furnace. Samples for the measurement were then cut out of these blocks, ground and finally polished. The TCE was derived from fitted curves of the measurement of relative expansion, which provided better results instead of deriving the TCE directly from the measured values. The thermal expansion was investigated up to a temperature of 800 K using a thermo-mechanical analyzer TMA2940 from TA Instruments. The results shown in figure A.1 and A.2 were later used for calculation of the relative permittivity.
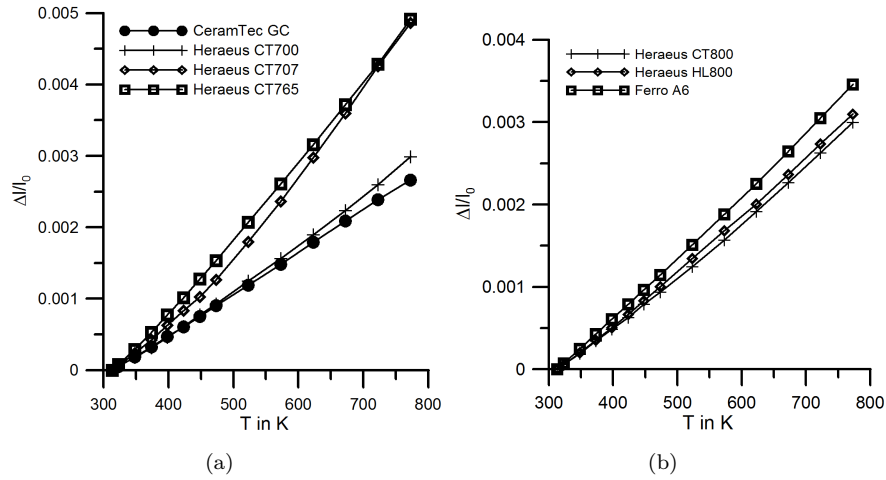
FIGURE A.1: Thermal expansion of different tape materials.
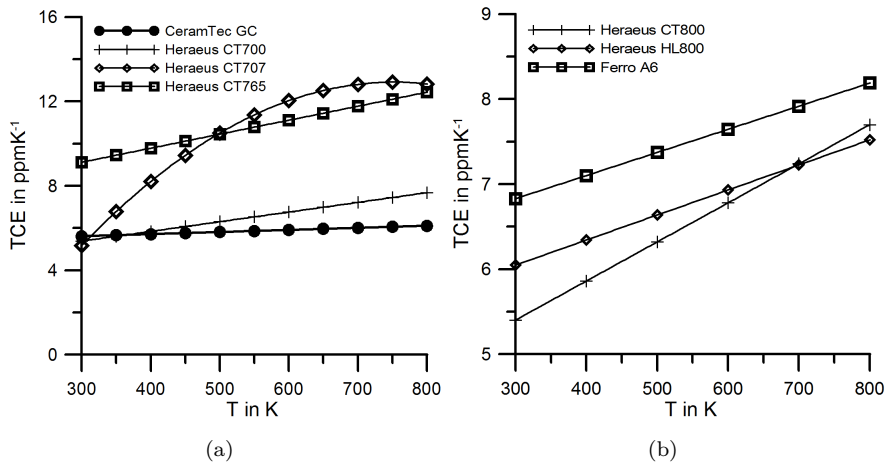


FIGURE A.2: Calculated thermal coefficient of expansion of different tape materials.

## A.3.2   YOUNG's Modulus of LTCC tape materials [2]

**Static 3 point bending test**

The three point bending test is conducted according to the principle shown in figure A.3. The beam to be tested is freely supported between two bearings. At the central position of the sample a force is exerted which results in a deflection of the beam.
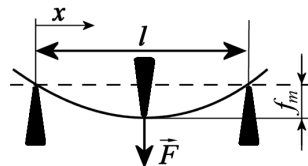


FIGURE A.3: Principle of bending test.

97

The relationship between Young's modulus, deflection, forces and geometric parameters are given by equations A.1 and A.2 [43].

$$E = \frac{Fl^3}{48 f_m I} \tag{A.1}$$

$$I = \frac{w d^3}{12} \tag{A.2}$$

$E$ is the Young's modulus of elasticity in Pa, $F$ the Force in N acting in the center, $f_m$ is the maximum deflection in m at $x = l/2$, $l$ the bearing distance, I the moment of inertia of plane area in $m^4$, $w$ the width and $d$ the thickness of the sample.

**Bending test set-up**

A schematic of the applied 3-point bending test set-up is shown in figure A.4. The support carrying the bearings (made up of $300\,\mu m$ thick ceramic blades) with a separation distance of 43.5 mm is positioned onto a microbalance. The sample is placed on the bearings and the total weight of the bearing support including the sample to be tested are balanced. The fired LTCC beam element is deflected at the central position of bearing clearance by a ceramic wedge, which is displaced by a micrometer. The resulting force is recorded by the microbalance.

**LTCC test sample preparation**

LTCC tapes of three different suppliers have been evaluated where single layer and co-laminated double layers of the corresponding tapes have been fired. Samples were allowed to freely shrink during the course of sintering, additionally samples have been prepared that have been co-laminated with the Ceramtec A-tape - a pure alumina tape - in order to prevent lateral shrinkage of the LTCC tape during firing. This constrained sintering results in increased shrinkage in thickness of the tape. After firing, the brittle alumina tape can be removed from the LTCC substrate. Furthermore, it became obvious, that mechanical stress induced in the green state of tapes by handling and machining procedures leads to warping and inhomogeneous material thickness in the fired state. A uniform plane surface for a single layer of tape could only be attained by co-lamination with the Ceramtec A tape, which is provided for a constrained sintering process. The relevant processing parameters for the lamination and firing of the tapes are summarized in table A.3. The lamination process has been conducted in an uniaxial press (Wabash) and firing of tapes has been performed in a conventional five zones thick film furnace
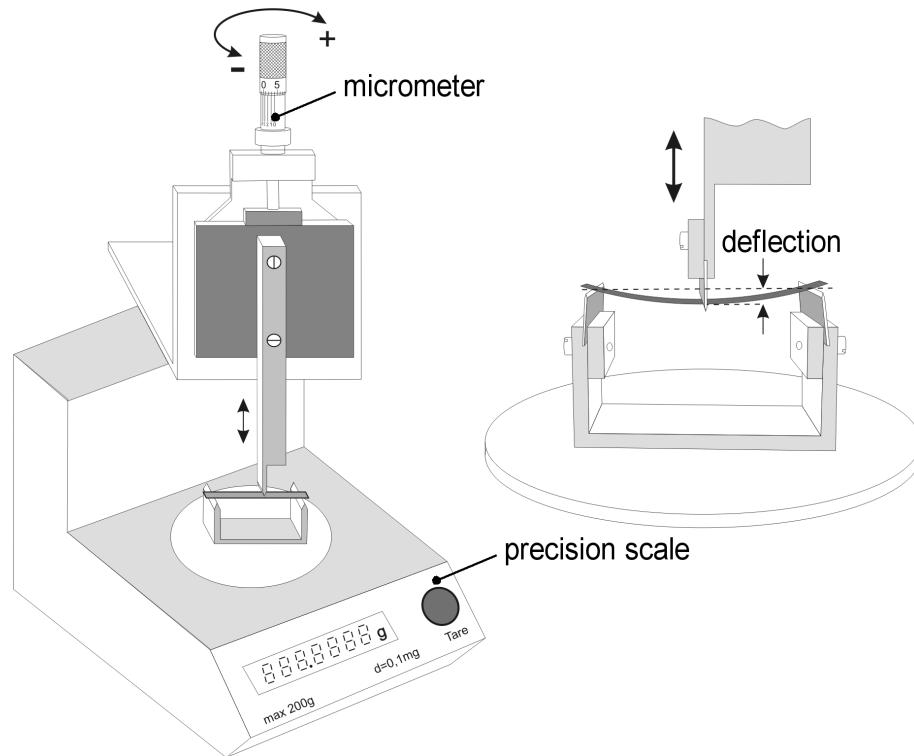
FIGURE A.4: Bending test set-up.

(BTU-Explorer). Test samples with the length of 50 mm and width of 5 mm have been cut out of the fired tape sheets by a Nd:YAG laser. The relative large-size sample has been selected in order to eliminate a potential influence of the laser machined edge zones on the mechanical performance of the beam element. The laser machining of the LTCC tapes has been conducted with a Q-switched diode pumped 120 W Nd:YAG-laser (Rofin Sinar Powerline 100D). Plain LTCC stripes and on both sides metalized LTCC beams have been prepared for the bending tests. The double-sided metallization has been applied to a selected number of samples via screen-printing (Heraeus AgPd-conductor paste C4140D, 325 mesh screen coated with a 50 μm thick Murakami stencil, resulting fired thickness of metallization: 11 μm) in order to evaluate the influence of a metal layer on the mechanical performance of the fired LTCC tapes.

**Results of bending test**

The graphs in figures A.5a to A.7a show the force-deflection characteristics of the different plain tape samples. All considered samples show a linear characteristic. The corresponding values for spring constant and Young's modulus are indicated in the graphs. The large deflection range for the considered bearing clearance of 43.5 mm is somewhat remarkable. The graphs in figures A.5b to A.7b demonstrate the influence of metallization on the mechanical performance characteristic of beam elements. The

applied metallization contributes to an increase of spring constant as well as Young's modulus and a dramatic change in mechanical performance. Bending of metalized LTCC tapes may result in a plastic deformation of samples. This is reflected by a hysteretic characteristic as demonstrated in the above mentioned graphs.

| Material | Thickness unfired $[\mu m]$ | Sinteringmethod | Lamination parameter | Peak firing temperature & dwell time |
|---|---|---|---|---|
| Heraeus CT700 | 130 | constrained | $2.3\,\text{N/mm}^2$, $95\,°\text{C}$, $3\,\text{min}$ | $865\,°\text{C}$, |
| | | free | $2.3\,\text{N/mm}^2$, $95\,°\text{C}$, $3\,\text{min}$ | $25\,\text{min}$ |
| Ferro A6 | 110 | constrained | $24\,\text{N/mm}^2$, $95\,°\text{C}$,$3\,\text{min}$ | $850\,°\text{C}$, |
| | | free | $24\,\text{N/mm}^2$, $95\,°\text{C}$, $3\,\text{min}$ | $15\,\text{min}$ |
| Cer- amTec GC | 100 | constrained | $4\,\text{N/mm}^2$, $70\,°\text{C}$, $3\,\text{min}$ | $890\,°\text{C}$, $15\,\text{min}$ |
| Cer- amTec GC | 300 | constrained | $4\,\text{N/mm}^2$, $70\,°\text{C}$, $3\,\text{min}$ | $890\,°\text{C}$, |
| | | free | $4\,\text{N/mm}^2$, $70\,°\text{C}$, $3\,\text{min}$ | $15\,\text{min}$ |

TABLE A.3: Processing Parameters of the tapes.

| Material | Sintering method | Number of layers | Fired thickness | spring constant | Young's modulus |
|---|---|---|---|---|---|
| Heraeus CT700 | free | 1 | 125 | 30.9 | 65.1 |
| | | 2 | 200 | 160 | 82.3 |
| | constrained | 1 | 80 | 7.3 | 58.7 |
| | | 2 | 150 | 52 | 63.4 |
| Ferro A6 | free | 1 | 110 | 18.3 | 56.6 |
| | | 2 | 200 | 160 | 82.3 |
| | constrained | 1 | 110 | 20.6 | 63.7 |
| | | 2 | 190 | 108.6 | 65.2 |
| CeramTec GC | free 300 µm | 1 | 240 | 430.4 | 128.1 |
| | constrained 300 µm | 1 | 175 | 111.2 | 85.4 |
| | constrained 100 µm | 1 | 65 | 5 | 74.9 |

TABLE A.4: Young's modulus and spring constant of LTCC material samples.

**Temperature dependence (Dynamic 3 point Bending test)[1]**

For the measurement of Young's Modulus samples with a size of 5 x $50\,\text{mm}^2$ were prepared. A dynamic 3-point bending test with $20\,\text{mm}$ bearing distance and a deflection

(a) plain samples

(b) double sided metallization
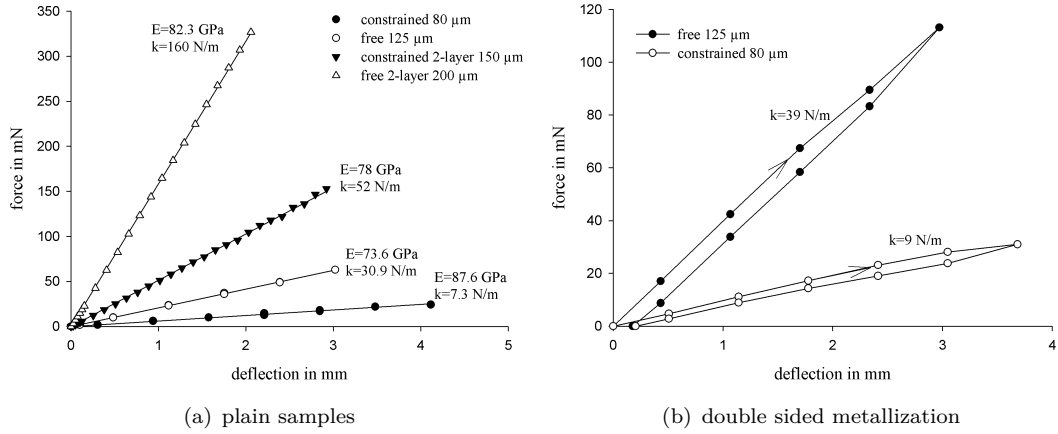
FIGURE A.5: Force-deflection diagram of Heraeus CT700 samples.



(a) plain samples

(b) double sided metallization
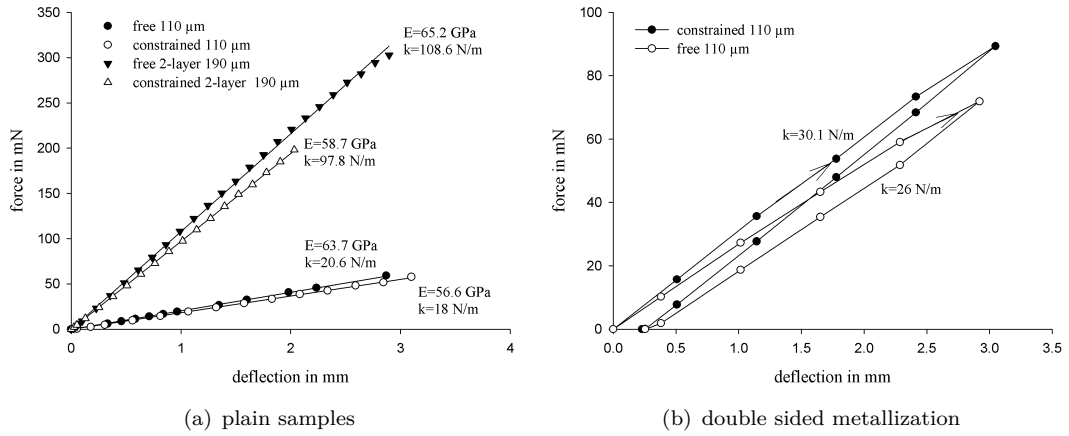
FIGURE A.6: Force-deflection diagram of Ferro A6 samples.



(a) plain samples

(b) double sided metallization
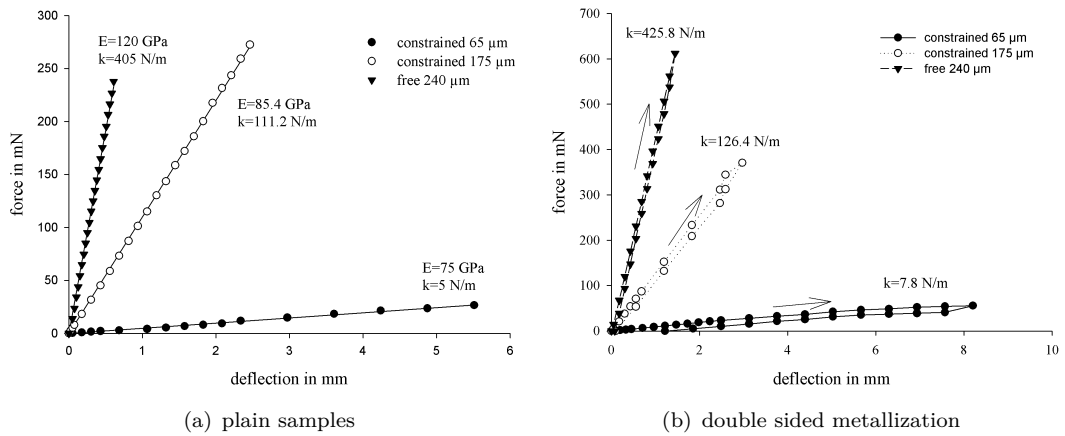
FIGURE A.7: Force-deflection diagram of CeramTec GC samples.

amplitude of 100 μm was performed over a temperature range from 300 to 800 K using a TA Instruments DMA2980 automated tester. Table A.5 shows the material thickness, thermal coefficient of expansion and Young's modulus at room temperature. The temperature dependence of Young's modulus is plotted in figure A.8 for the investigated LTCC tape materials.

| Material | Cer-amTec GC | Heraeus CT700 | Heraeus CT707 | Heraeus CT765 | Heraeus CT800 | Heraeus HL800 | Ferro A6 |
|---|---|---|---|---|---|---|---|
| thickness [μm] | 242 | 121 | 120 | 320 | 66 | 70 | 108 |
| TCE [ppm/K] @ 300 K | 5.61 | 5.38 | 5.17 | 9.12 | 5.04 | 6.05 | 6.83 |
| Young's Modulus [GPa] @ 300 K | 107 | 73 | 54 | 85.5 | 91.5 | 66 | 66 |

TABLE A.5: Materials property data.
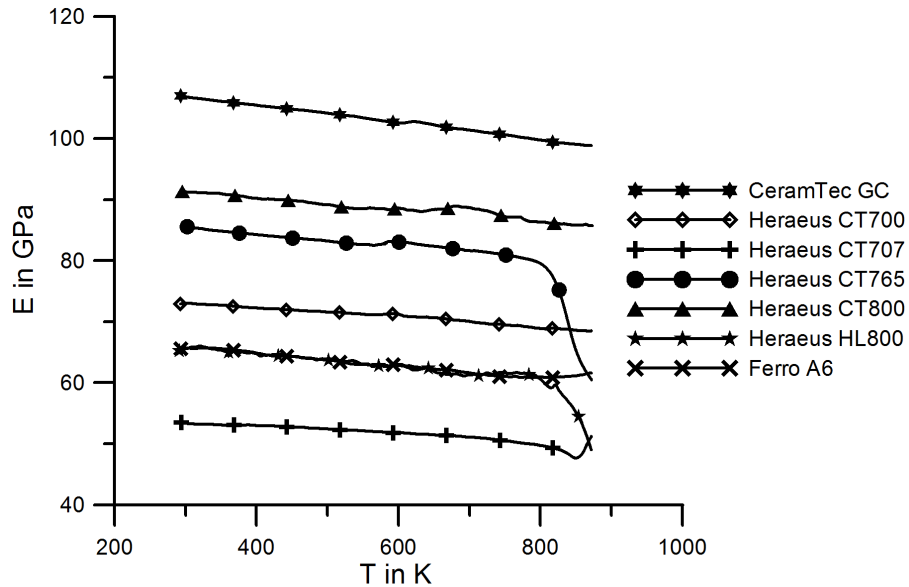


FIGURE A.8: Young's modulus of investigated tape materials.

### A.3.3 Dielectric properties of LTCC tape materials[1]

The characterization was done in two steps. In the first step, disc shape capacitors were characterized at 1 kHz frequency up to 725 °C to evaluate the material and test for resinate paste compatibility (Heraeus RP26001/59). In the second step, capacitor

samples where LTCC tape material and paste were cofired were characterized from DC to 20 MHz again up to a temperature of 725 °C. These results were used to develop a capacitive wireless temperature sensor to be used inside a module where the temperature profile inside that module is not distorted by the sensor due to connections.

## Temperature dependence of the permittivity at low frequency

For the measurement of the permittivity of the LTCC tape samples, discs with 10 mm diameter fired inside a conventional belt furnace with 2 h cycle time were prepared. A double-sided metallization was applied using a post firing process at a peak temperature of 850 °C and 10 min dwell time. Because a thick metallization can cause thermal strain that prevents undisturbed thermal expansion of the capacitor samples, a AuPd-resinate paste from Heraeus (RP26001/59) yielding a 200 nm thick metallization was used. The capacitance was measured at a test frequency of 1 kHz over temperature and the permittivity was then calculated from the measured capacitance of the samples and their respective geometry. For the calculation, it was assumed that the capacitor consists only of a circular plate of material where the applied electrodes are extremely thin and do not interfere with the thermal expansion of the bulk material. Effects of stray fields at the border zones were neglected. The measurement was carried out using a box furnace together with a LCR131 component tester. The temperature was tracked with a type-K thermocouple probe near the sample. The connections were fed through a ceramic multi-hole tube into the furnace chamber. The resistivity of the samples was also measured at 725 °C to get a quick overview of the material behavior - no guard ring electrode was used for this measurement. The results are summarized in table A.6 and figure A.9.

| Material | Fired sample thickness d [$\mu m$] | $C$ @ 300 K [pF] | $\varepsilon_r$ @ 300 K [1] | Resistance R @ 1000K [$\Omega$] |
|---|---|---|---|---|
| CeramTec GC | 240 | 22.6 | 7.80 | 590k |
| Heraeus CT700 | 170 | 29.5 | 7.22 | 370k |
| Heraeus CT707 | 110 | 49.2 | 6.39 | 240k |
| Heraeus CT765 | 110 | 270 | 42.7 | 100k |
| Heraeus CT800 | 180 | 29.2 | 7.54 | 5M |
| Heraeus HL800 | 180 | 38.3 After test: 44.8 | 8.82 | 89 |
| Ferro A6 | 380 (4 layers) | 11.3 | 6.18 | 82k |

TABLE A.6: Capacitance and relative permittivity of circular capacitor samples at 1kHz test frequency.
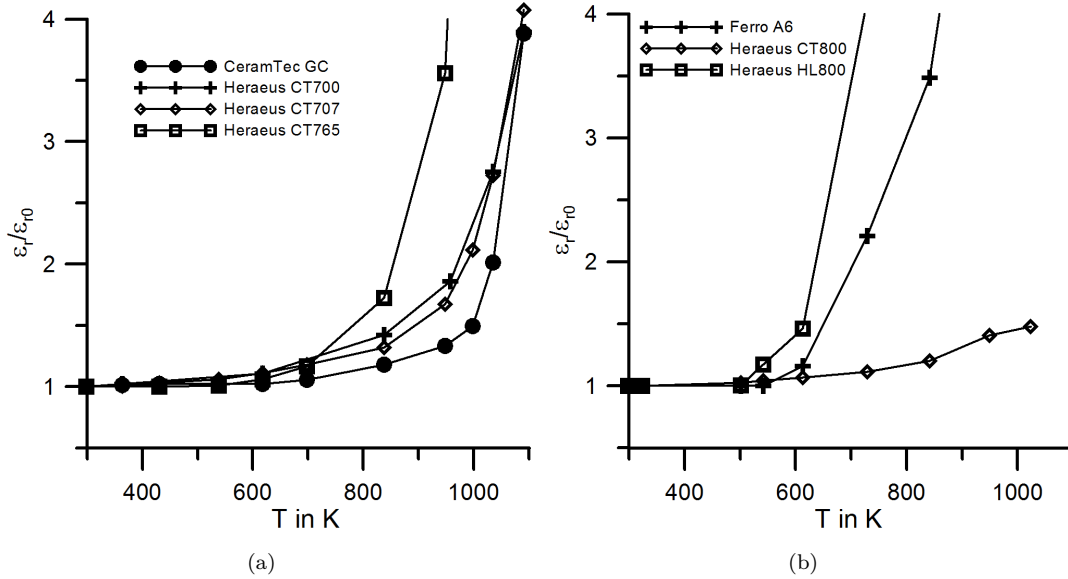
FIGURE A.9: Permittivity vs. temperature characteristics.

### A.3.4 Impedance Spectroscopy[3]

Impedance spectroscopy investigates the impedance behavior of a sample over frequency and temperature to identify the influence of the microscopic structure comprised of different grains, grain boundaries and impurities inside the ceramic on the dielectric properties. For these investigations, the sample preparation and experimental set-up are discussed and measurement of the impedance versus temperature is presented. An attempt is made to interpret the results using a "lumped" R-C-constant phase element (CPE) model from which the DC-conductivity is derived and activation energies are calculated by means of an enhanced Arrhenius theory. Conclusions are drawn about the suitability of the tape materials for different applications.

**Sample preparation**

For all materials, capacitor samples with an unfired size of 12 x 12 $mm^2$ and electrodes of 10 x 10 $mm^2$ (figure A.10) were manufactured. The electrodes were screen-printed onto the unfired tapes using TC7304 silver conductor paste from Heraeus. After a lamination step using a computer controlled uni-axial press (Carver) the samples were fired inside a belt furnace at the appropriate temperature. Table A.7 gives an overview of the prepared samples with their respective material and processing parameters.

| Material | Screen | Lamination | Peak firing temperature |
|----------|--------|------------|-------------------------|
| Heraeus CT765 | stainless steel | $7\,\mathrm{N/mm^2}$, $70\,^{\circ}\mathrm{C}$, $3\,\mathrm{min}$ | $900\,^{\circ}\mathrm{C}$, $25\,\mathrm{min}$ |
| Heraeus HL800 | 320 mesh | | $865\,^{\circ}\mathrm{C}$, $25\,\mathrm{min}$ |
| Ferro A6 | Murakami | $11\,\mathrm{N/mm^2}$, $70\,^{\circ}\mathrm{C}$, $3\,\mathrm{min}$ | $850\,^{\circ}\mathrm{C}$, $25\,\mathrm{min}$ |
| CeramTec GC | $30\,\mathrm{\mu m}$ stencil | $4\,\mathrm{N/mm^2}$, $70\,^{\circ}\mathrm{C}$, $3\,\mathrm{min}$ | $885\,^{\circ}\mathrm{C}$, $25\,\mathrm{min}$ |

TABLE A.7: Processing parameters for tape samples.

**Experimental set-up**

For measuring the impedance at elevated temperature, the samples were placed inside a sample holder consisting of a closed-end fused-silica tube with a side-port for sample insertion and a push rod that clamps the electrode and the sample by spring force (Figure A.11 and A.12). Silver wires and electrodes establish contact to the screen-printed electrodes on the sample surface. A type-K thermocouple is used to measure the actual temperature close to the sample. A fused-silica sleeve protects the sample from the atmospheric influence inside the tube furnace used for the measurement.
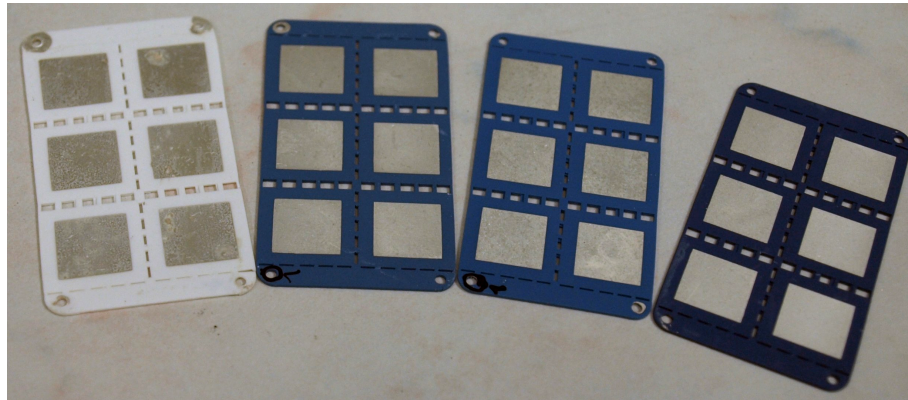


FIGURE A.10: Capacitor samples made of different LTCC tape material before separation.



FIGURE A.11: Measurement assembly.
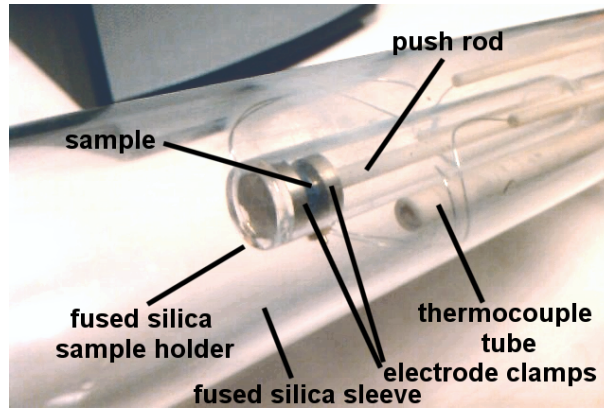
FIGURE A.12: Sample holder detail inside measurement assembly.

Impedance measurement was carried out using an electro chemical impedance analyzer (Novocontrol ALPHA) that is connected to the sample holder by $50\,\Omega$ BNC-cables. A Keithley 2000 high-resolution multimeter was used with a type-K thermocouple for temperature measurement. The temperature inside the tube furnace is controlled by an EUROTHERM 94 temperature controller with a separate thermocouple. The measurements were conducted automatically using a standard PC with custom software. The measurement equipment was controlled via GPIB-Bus and the temperature controller via RS232 interface respectively.

**Measurement results**

Due to the rather complex set-up that is necessary for measurements at elevated temperature and low expected capacitance values of the samples, measurement of the capacitance and calculation of the permittivity was carried out at room temperature first using a simplified set-up. Figure A.13 shows the expected stable permittivity and low losses at room temperature over a frequency range from $10\,\text{Hz}$ to $2\,\text{MHz}$. Only the HL800 (zero shrinkage 3 layer tape material) from Heraeus shows a significant change of impedance over frequency. This effect is independent of sample thickness and is pronounced when the samples are soaked in water and dried.

**Impedance Spectrum**

For further investigations, an extended impedance scan was carried out inside a tube furnace where the temperature is increased from room temperature up to maximum temperature of approximately $650\,^{\circ}\text{C}$ in $25\,^{\circ}\text{C}$ steps. Figure A.14 show the Nyquist plots for the different LTCC tape materials only at elevated temperature up to a frequency of $2\,\text{MHz}$ where they exhibit the lowest impedance. The plots show, that the impedance

(a) Permittivity vs. frequency      (b) $\tan\delta$ vs. frequency
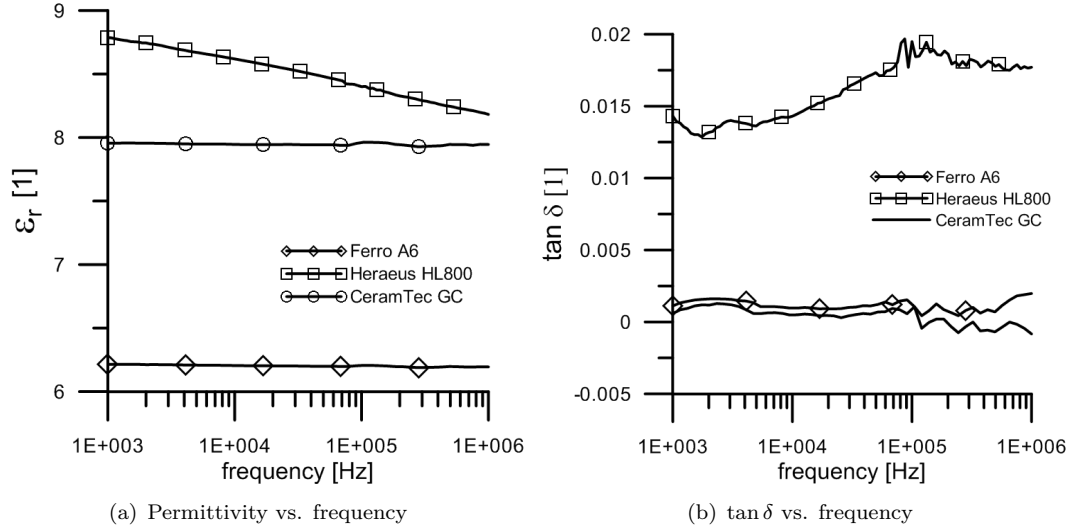
FIGURE A.13: Permittivity and loss tangent of tape materials.

spans several orders of magnitude at temperatures around 600 °C, especially the HL800 material becomes highly conductive. To investigate the contribution of different effects (losses inside dielectric, influence of grains) to the overall impedance of a polycrystalline bulk material the impedance spectrum has been measured at different temperature. At the first sight the impedance plots in figure A.14 show the form of a semi-circle which is usually associated with a simple parallel R-C-circuit as generally used to describe the losses (modeled with R) inside a capacitor C with a given permittivity. However, when an attempt is made to fit a semi-circle to reconstruct these plots it becomes obvious, that a different equivalent circuit is needed to describe the material behavior. With increasing temperature, the ion mobility also increases and effects the overall impedance which can be described by the following equivalent circuit (shown in figure A.15 as used for a typical polycrystalline glass or glass-ceramic dielectric material [44]. The ionic influence on the dielectric properties are modeled with a so-called constant phase element (CPE) described by equation A.3.

$$Z = Z_0 \cdot (j\omega)^{-P} \tag{A.3}$$

For capacitive effects, the parameter P ranges from 0 to 1 where 0 means pure resistive behavior and 1 a pure capacitor. The resistive part is proportional to the imaginary part of the impedance independent of frequency hence the name constant phase element. The impedance curves were fitted to the equivalent circuit by means of the program ZVIEW (Scribner Associates). The fitting process itself can be problematic when phase changes occur or the effects of ion conductivity become too weak. The obtained parameter values can be of poor quality in certain temperature regions and can only be used for qualitative information.

**Activation energy of ionic and electronic conductivity**

The ion conductivity $\sigma$ of a crystal can be expressed by a modified Arrhenius equation as A.4:

$$\sigma(T) = \frac{s_0}{T} \cdot e^{-\frac{E_A}{k_B T}} \tag{A.4}$$

where $\sigma$ denotes the ion conductivity dependent on temperature T in K, $s_0$ the reference conductivity term in S K, $E_A$ the activation energy in J and $k_B$ the Boltzmann constant. This equation can be transformed by using the natural logarithm to:

$$ln(\sigma T) = ln(\sigma_0) - \frac{E_A}{k_B T} \tag{A.5}$$

Comparison with a linear equation

$$y = mx + b \tag{A.6}$$

allows to extract the activation energy by plotting ln $(\sigma T)$ over $T^{-1}$ :

$$E_A = -m k_B \tag{A.7}$$

The curves in figure A.19 show 2 linear regions that can be correlated with the activation

| Material | Activation energy in J |
|---|---|
| Heraeus CT765 | 11.8x10-20 |
| Heraeus HL800 | 10.38x10-20 |
| Ferro A6 | 6.9x10-20 |
| CeramTec GC | 12x10-20 |

TABLE A.8: Processing parameters for tape samples.

energy of 2 physical effects. This can be ion-conductivity, electron-conductivity or even hole-conductivity. Because the measurements are less precise at lower temperature, only the activation energies for the high temperature region have been extracted. The lower the activation energy is, the lower the temperature where the ion mobility becomes noticeable as impedance change.
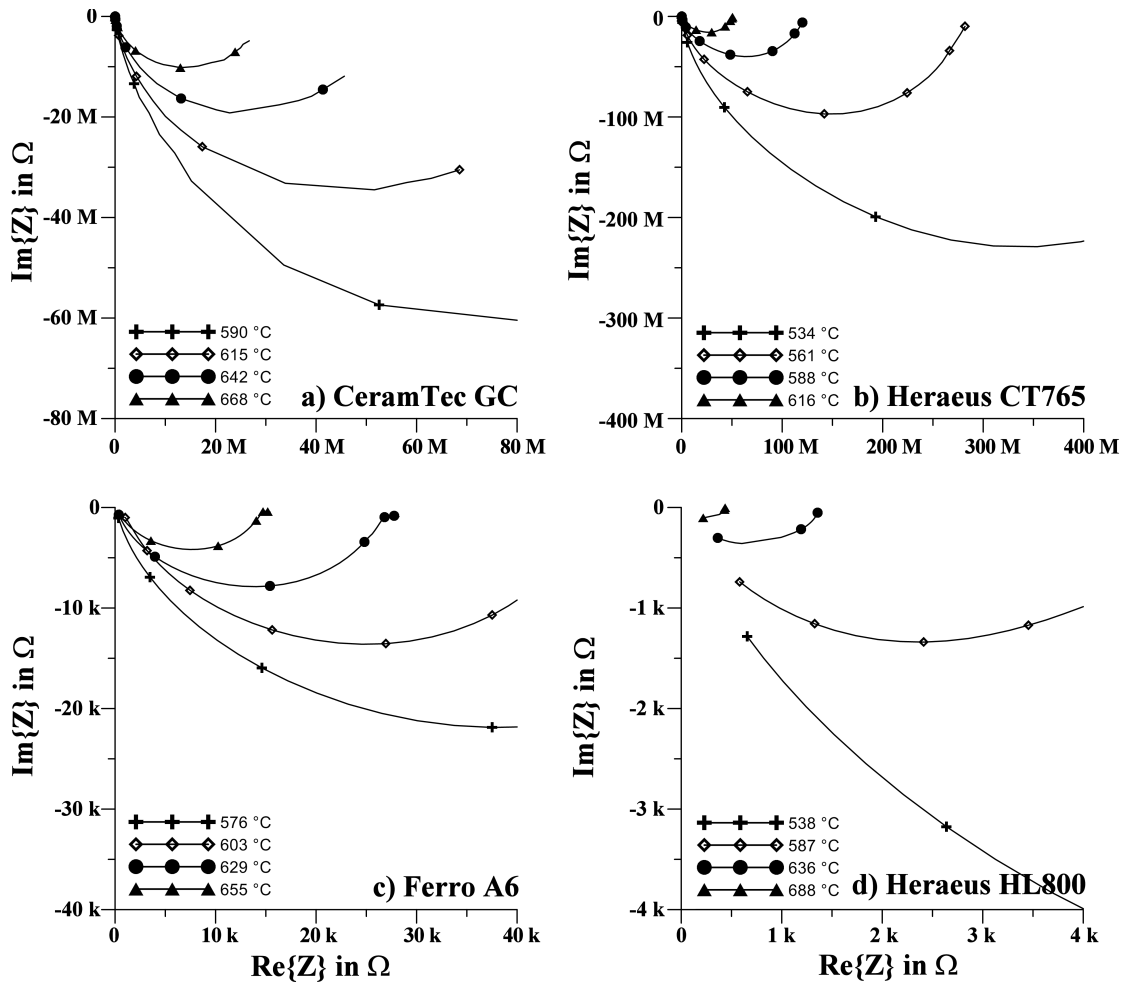
FIGURE A.14: Impedance of different LTCC tape sample from 1 Hz to 2 MHz: a) CeramTec GC, b) Heraeus CT765, c) Ferro A6 and d) Heraeus HL800.
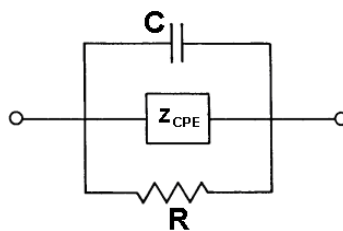


FIGURE A.15: Equivalent circuit for polycrystalline dielectric.
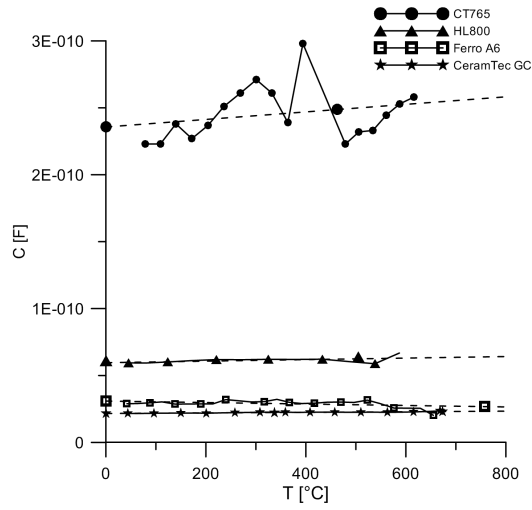
FIGURE A.16: Temperature dependence of equivalent circuit's capacitance.
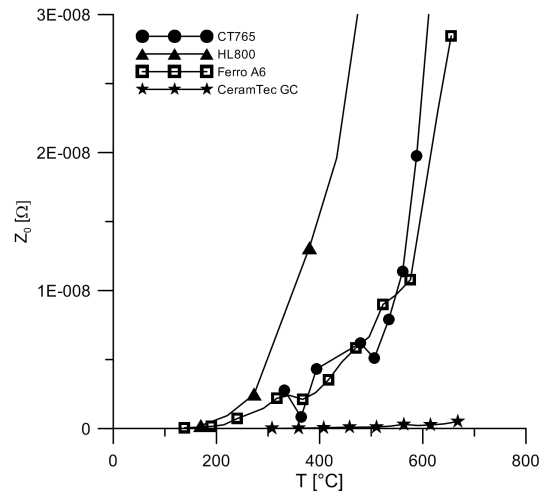


FIGURE A.17: Temperature dependence of equivalent circuit's CPE-Z0 Parameter.
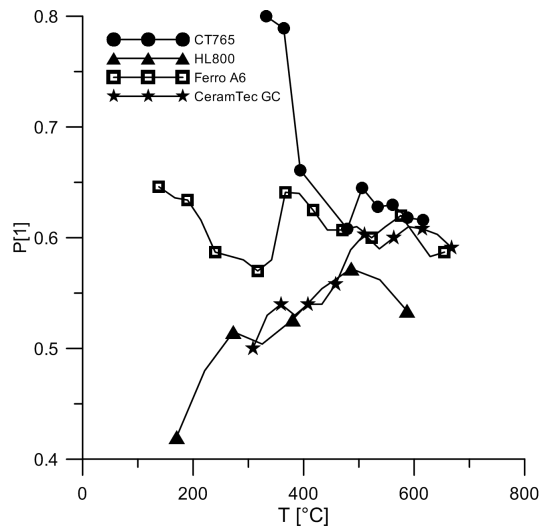


FIGURE A.18: Temperature dependence of equivalent circuit's CPE P parameter.
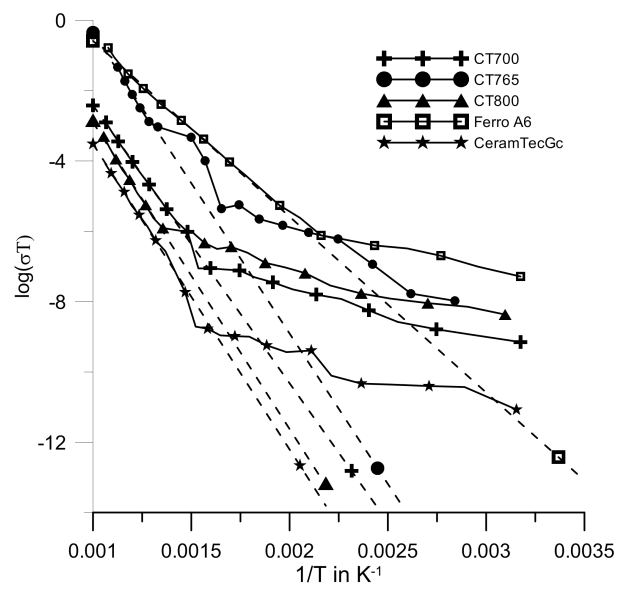
FIGURE A.19: Diagram for extraction of the activation energies.

## A.4 Hot embossing of channels and cavities

As lamination is a crucial step in the manufacturing process of LTCC modules, it is important that the material is compressed equally throughout the whole module. If areas exist, where the lamination pressure was not sufficient, warpage and delamination can occur. If the structures to be manufactured include channels with high aspect ratios or chambers, a sacrificial filler material must be used or the lamination has to be done in several steps. One possibility is the embossing technique that allows imprinting the structure onto the surface. During the work with several LTCC tapes it was noticed, that some tapes seem to flow and equalize the lamination pressure while other are more compressed and exhibit lower shrinkage as a result. Figure A.20 shows the difference in lamination pressure and resulting compression of laminated structured tapes and embossing the stack to form a cavity. In order to choose the best material for a microfluidic system, extreme dimensions were chosen to provoke a significant distortion to benchmark the materials.
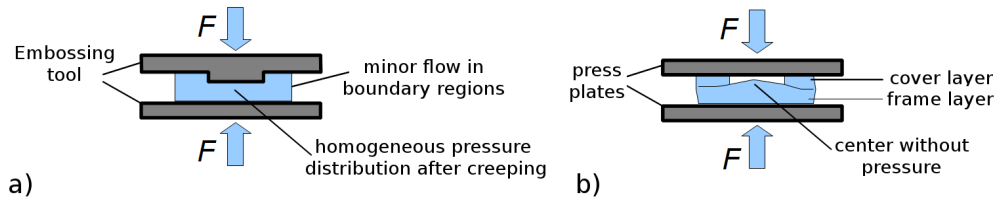


FIGURE A.20: Stresses and material flow during lamination and embossing.

### Press form and tools

For the embossing tests a uniaxial hydraulic press from Carver (Wabash,USA) was used. Because this press only offers flat press plates, a lamination tool was designed (see figure A.21) providing guiding bolts and alignment pins as well as a push screw to gently pull out the pins from the laminated structure. As embossing-tool laser-ablated polymer-inlays were used (figure A.22a) with a surface roughness sufficient for the rather coarse structures.

### Embossing tests

For the embossing tests, ceramic tapes with processing parameters listed in table A.9 were used. Depending on the tape thickness, 1 to 4 layers were laminated and embossed at the same time. The difference in material density between embossed areas and non-embossed regions became immediately visible with the CT-tape series from Heraeus
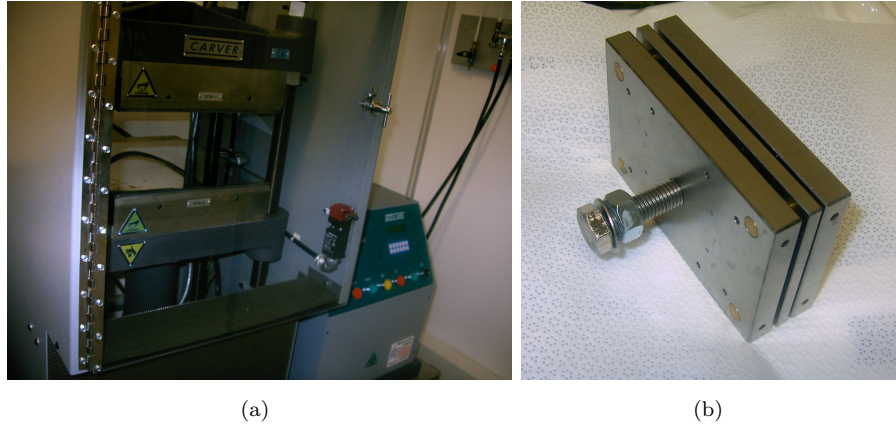
FIGURE A.21: Laminating press and pressing tool used in embossing test.
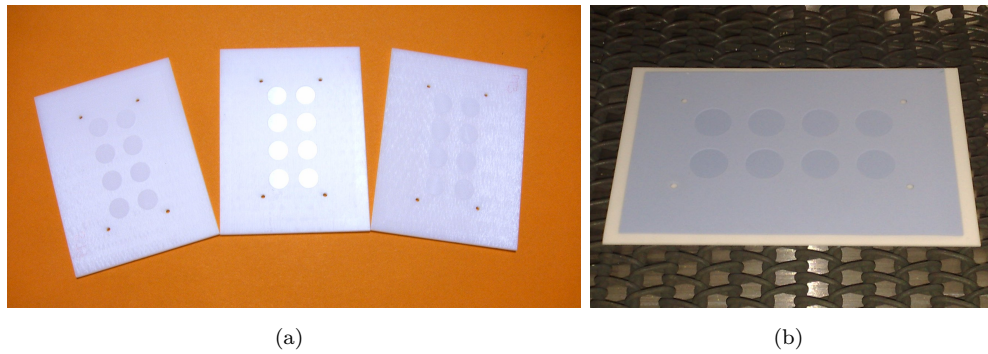


FIGURE A.22: Embossing tools and material compression:
a) Embossing tools with 50 µm, 75 µm and 100 µm embossing height and b) the visible compressed material in Heraeus CT700 tape with 100 µm embossing depth.

(figure A.22b) whereas the CeramTec tape is softer and more tolerant. This behavior is caused by the higher solid content of the Heraeus series, which limits the material flow during embossing and limits geometry size that can be embossed. This effect becomes dominant and prevents the material from being further compressed and effectivly blocks the embossing tool. In extreme cases, the areas outside the embossed zone are not laminated at all.

## A.5 Suitability of materials for different applications

The investigations of the dielectric properties show a dramatic change of impedance of LTCC materials versus temperature. Some materials (Heraeus HL800) exhibit a significant change in permittivity and conductivity already in a very low temperature region of around 150 °C, which is within the region of many automotive under hood applications. To obtain information about the long-term stability of LTCC modules at elevated temperature the activation energies can be an indication for the suitability of

a given application. For chemical applications, this can also mean a reduced inertness of the material for reactions at elevated temperatures or contamination of the analytes and degraded measurement accuracy. Further investigations are necessary to correlate the impedance effects with long-term stability of LTCC modules and their suitability in certain applications - this will be performed in future work.

The Young's modulus depends on the manufacturing parameters and is in the range of 50 to 130 MPa for the investigated tape materials. A significant difference of up to +50% for free sintering compared to constrained sintering can be observed for certain tape materials. Together with the difference in thermal expansion, a significant temperature gradient can lead to cracking of the module due to induced thermomechanical stress. The design of a module must consider the mechanical stress when elevated temperatures inside the modules are desired as well as the achieved sintered density of the material which depends on process parameters like lamination pressure and sintering temperature as well as process speed and dwell time.

| Material | tape thickness unfired in µm | pressure in bar | sintering profile | thickness fired (1 layer) in µm | emboss- ing result |
|---|---|---|---|---|---|
| Heraeus CT700 | 300 | 70 | 865 °C, 30 min peak | 240 | mediocre |
| Heraeus CT707 | 185 | 70 | 865 °C, 30 min peak | 150 | mediocre |
| Heraeus CT800 | 238 | 70 | 865 °C, 30 min peak | 238 | good |
| CeramTec GC | 300 | 50 | 900 °C, 30 min peak | 240 | very good |

TABLE A.9: Processing parameters for embossing samples.

| | | |
|---|---|---|
| a) 1 Layer, 50 µm | b) 1 Layer, 100 µm | |
| c) 2 Layer, 50 µm | d) 2 Layer, 100 µm | e) 3 Layer, 150 µm |
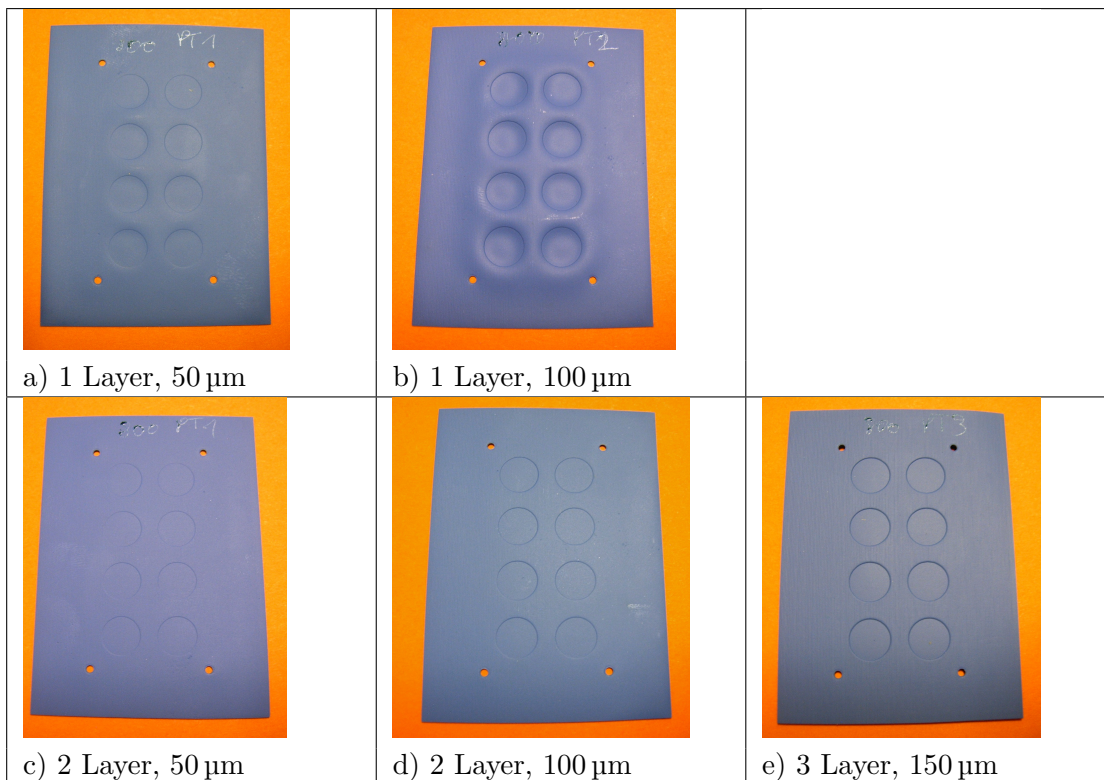
TABLE A.10: Embossing results for Heraeus CT800.

| | | |
|---|---|---|
| a) 1 Layer, 50 µm | b) 1 Layer, 100 µm | |
| c) 2 Layer, 50 µm | d) 2 Layer, 100 µm | e) 3 Layer, 150 µm |
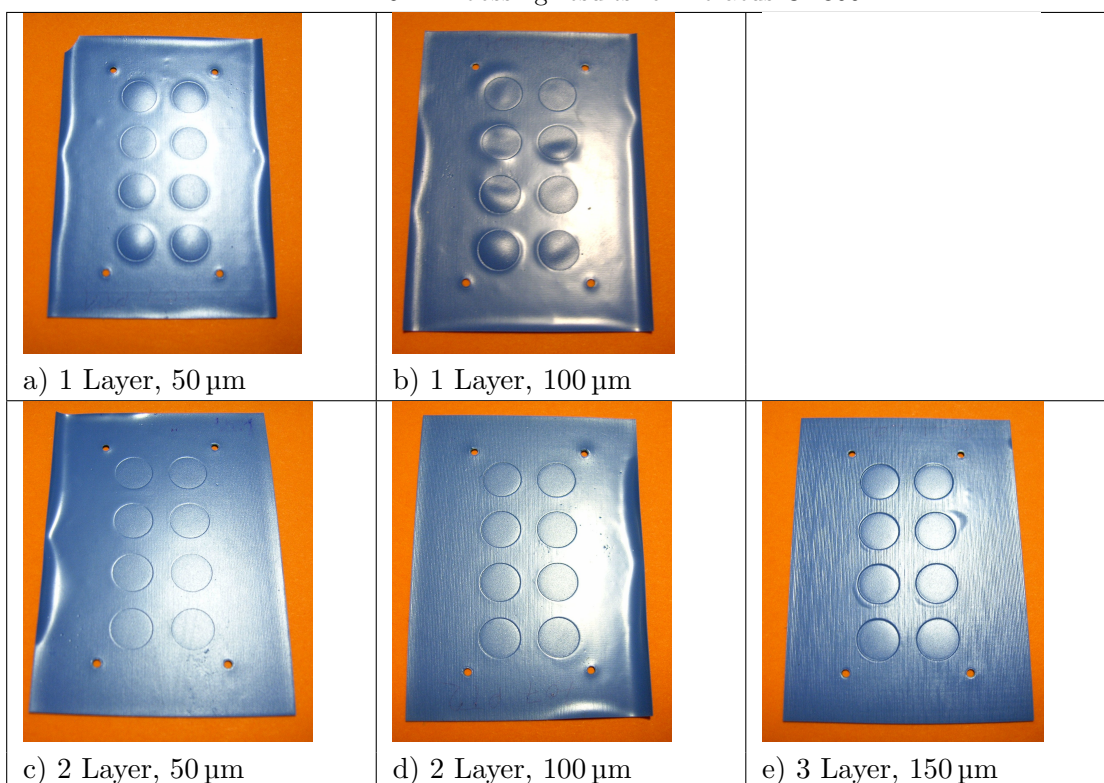
TABLE A.11: Embossing results for Heraeus CT707.

| | | |
|---|---|---|
|  |  | |
| a) 1 Layer, 50 µm | b) 1 Layer, 100 µm | |
|  |  |  |
| c) 2 Layer, 50 µm | d) 2 Layer, 100 µm | e) 2 Layer, 150 µm |
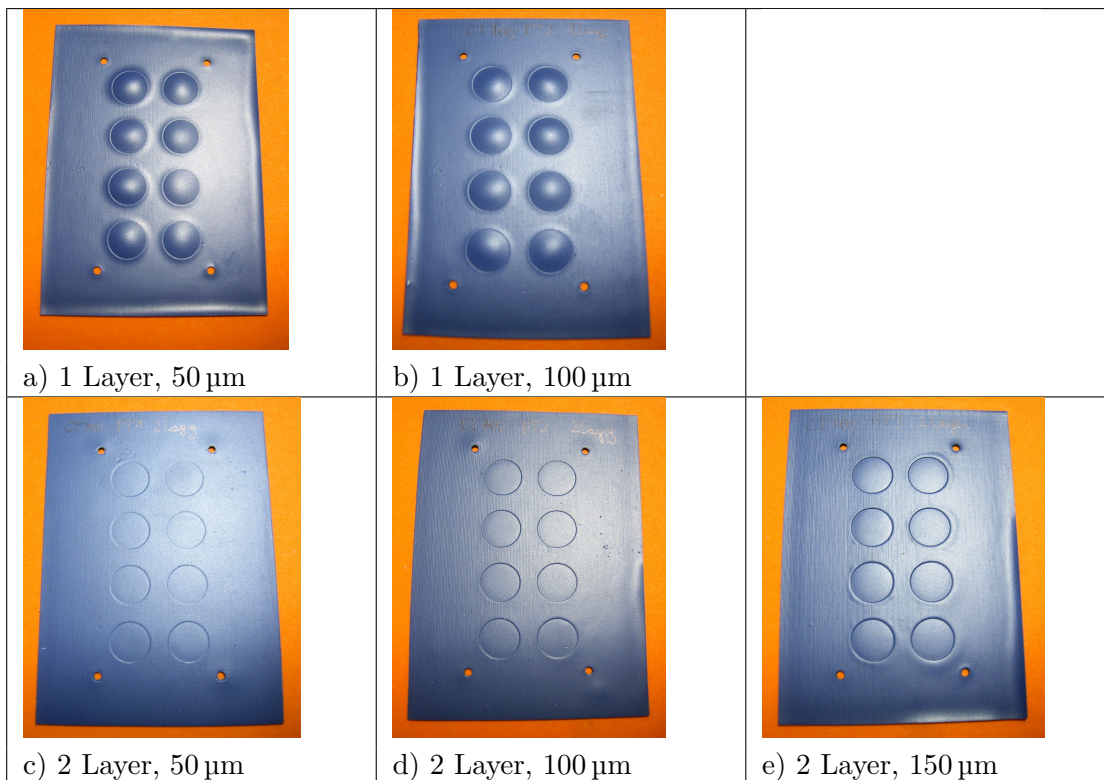
TABLE A.12: Embossing results for Heraeus CT700.

| | | |
|---|---|---|
|  |  |  |
| a) 1 Layer, 50 µm | b) 1 Layer, 100 µm | c) 2 Layer, 150 µm |
|  |  |  |
| d) 2 Layer, 50 µm | e) 2 Layer, 100 µm | f) 3 Layer, 150 µm |
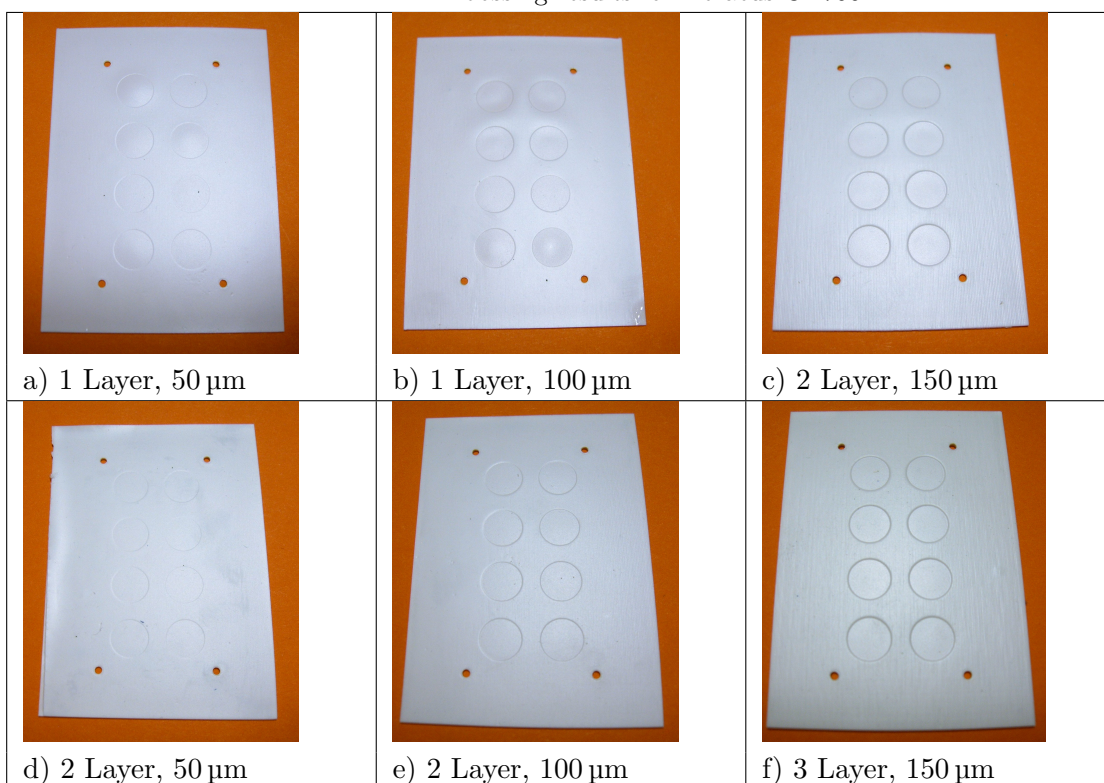
TABLE A.13: Embossing results for CeramTec GC.

|  |  |  |
|---|---|---|
| a) 2 Layer, 50 µm | b) 2 Layer, 100 µm | 3 Layer, 150 µm |
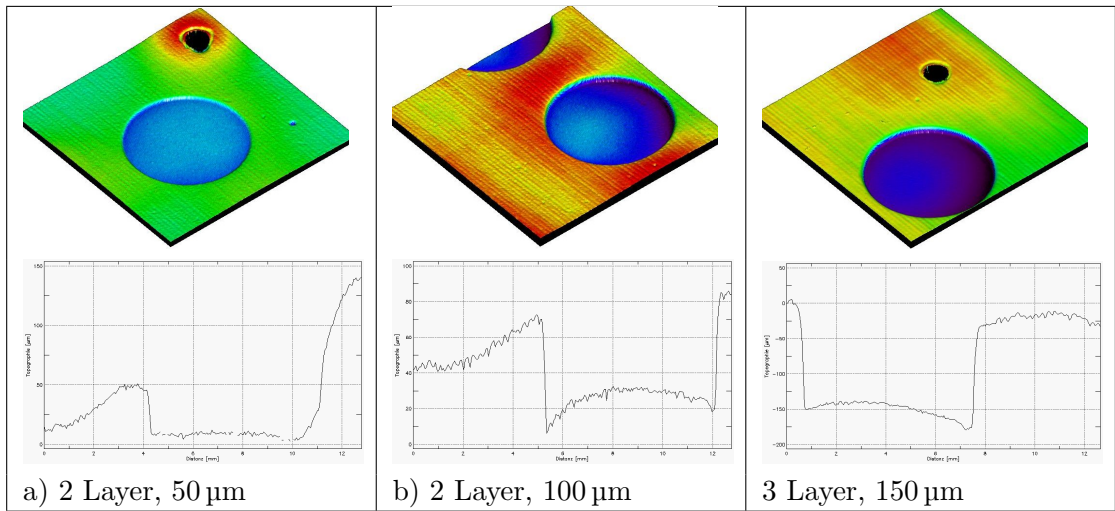
TABLE A.14: 3D-scans for Heraeus CT800.



|  |  |  |
|---|---|---|
| a) 2 Layer, 50 µm | b) 2 Layer, 100 µm | 3 Layer, 150 µm |
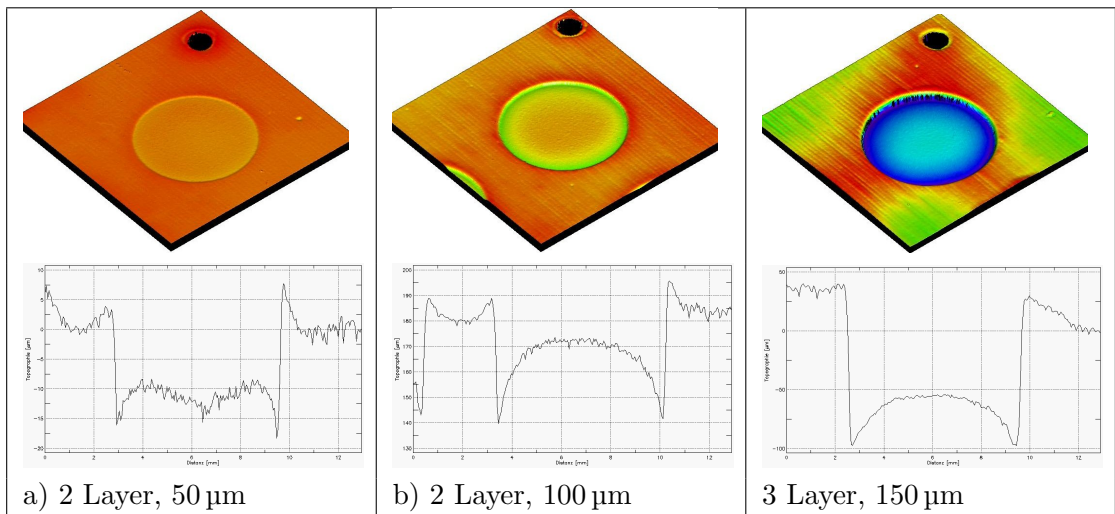
TABLE A.15: 3D-scans for Heraeus CT707.



|  |  |  |
|---|---|---|
| a) 2 Layer, 50 µm | b) 2 Layer, 100 µm | 2 Layer, 150 µm |
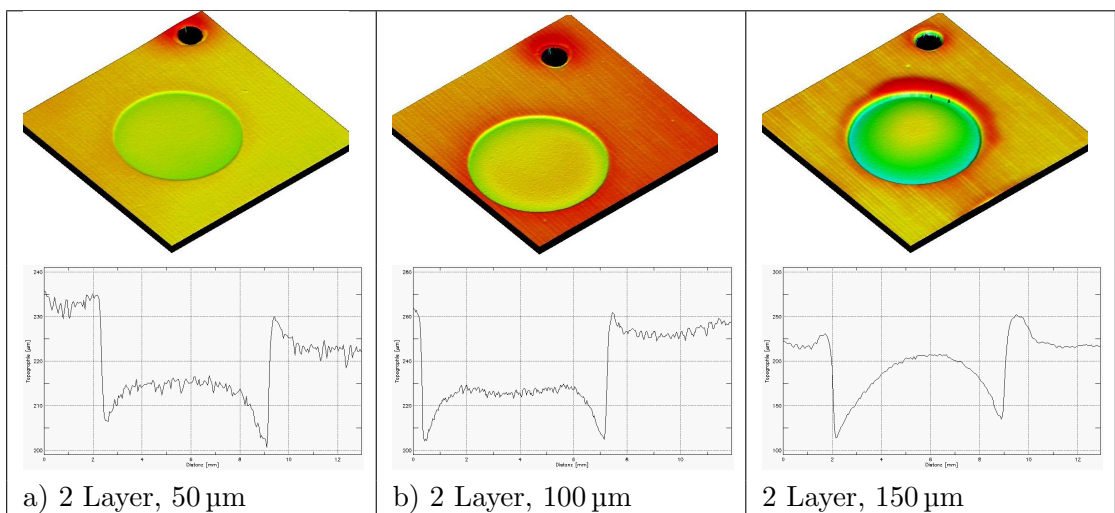
TABLE A.16: 3D-scans for Heraeus CT700.

117

|  |  |  |
|---|---|---|
| a) 2 Layer, 50 µm | b) 2 Layer, 100 µm | 3 Layer, 150 µm |
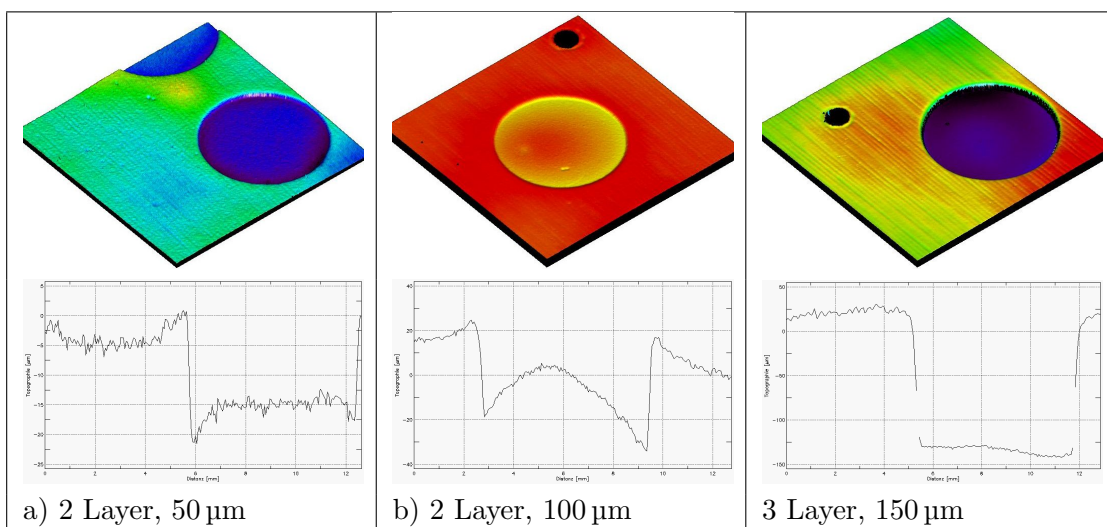
TABLE A.17: 3D-scans for CeramTec GC.

# Appendix B

# Publications

## B.1   Journals

1. N. Blaž, Andrea Marić, G. Radosavljević, L. Živanov, G. Stojanovic, I. Atassi, M. Unger, W. Smetana: "Determination of Electrical and Magnetic Characteristics of Different LTCC Tapes"; Proceedings E!4570 IPCTECH. New Generation of 3-D Integrated Passive Components & Microsystems in LTCC-Technology, 1 (2011), 57 - 64.

2. E. Eisermann, K. Höll, W. Smetana, W. Tusler, M. Unger, J. Whitmarsh: "Comparison of low cost, insulated aluminium substrates used as integrated heat sinks with conventional technology"; Microelectronics International, 26 (2009), 2:3 - 2:9.

3. G. Langer, M. Leitgeb, J. Nicolics, M. Unger, H. Hoschopf, F. Wenzl: "Advanced Thermal Management Solutions on PCBs for High-Power Applications"; SMT Magazine, 6 (2014), 12 - 32.

4. G. Radosavljević, A. Marić, G. Stojanović, W. Smetana, M. Unger, H. Homolka: "Application of the LTCC technology for the fabrication of the RF 3D inductor"; Romanian Journal of Information Science and Technology, 11 (2008), 2; 193 - 202.

5. G. Radosavljević, A. Marić, M. Unger, N. Blaz, W. Smetana, L. Živanov: "Electrical, mechanical and temperature characterization of commercialy available LTCC dielectric materials"; Hemijska industrija, 67 (2013), 4; 621 - 628.

6. G. Radosavljević, W. Smetana, A. Marić, L. Živanov, M. Unger, G. Stangl: "Parameters affecting the sensitivity of LTCC pressure sensors"; Microelectronics International, 27 (2010), 3; 159 - 165.

7. G. Radosavljević, L. Živanov, W. Smetana, A. Marić, M. Unger, L. Nad: "Wireless Embedded Resonant Pressure Sensor Fabricated in the Standard LTCC Technology"; IEEE Sensors Journal, 9 (2009), 1956 - 1962.

8. M. Unger, W. Smetana, J. Nicolics: "Analyses of Fluid Temperature Profile in a Continuous-Flow Heater for Lab-In-Module Application"; Proceedings E!4570 IPCTECH. New Generation of 3-D Integrated Passive Components & Microsystems in LTCC-Technology, 1 (2011), 92 - 107.

## B.2 Publications in Proceedings

1. M. Unger, J. Nicolics: "Discretisation and Data Reduction Algorithm for FE Modelling of Complex Multilayer PCBs with Embedded Components"; in: "Proceedings of the 2018 41st International Spring Seminar on Electronics Technology (ISSE)", IEEE Xplore, 2018, ISBN: 978-1-5386-5731-7, S. 1 - 6.

2. M. Franz, M. Unger, G. Schmid, J. Nicolics: "Environmental Assessment of a New Developed Camera System for Automotive Application"; in: "Proceedings of the 2018 41st International Spring Seminar on Electronics Technology (ISSE)", IEEE Xplore, 2018, ISBN: 978-1-5386-5731-7, S. 1 - 7.

3. M. Franz, M. Unger: "Ecological Aspects of a Novel Embedding Technology for Automotive Power Applications"; in: "Book of Abstracts", IEEE 39th International Spring Seminar on Electronics Technology, May 18-22, Pilsen, Czech Republic, University of West Bohemia in Pilsen, 2016, ISBN: 978-80-261-0618-0, 195 - 196.

4. G. Mišković, L. Vuckovic, J. Fernandez, H. Homolka, M. Unger, G. Radosavljević: "Investigation on Physical and Electrical Behaviour of LTCC Dielectric Tapes"; in: "Proceedings 37th Int. Spring Seminar on Electronics Technology", IEEE Computer Society, 2014, ISBN: 978-1-4799-4455-2, 6 pages.

5. M. Unger, J. Fleig, M. Ahrens, W. Smetana, G. Radosavljević: "Permittivity and conductivity of various LTCC-tapes at high temperature"; in: "Conference Proceedings", issued by: IEEE; IEEE Xplore, 2010, ISBN: 978-1-4244-7849-1, 6 pages.

6. M. Bilinski, E. Eisermann, K. Jones-Williams, W. Smetana, M. Unger, J. Withmarsh: "Thick film pastes for the manufacture of low cost, insulated aluminium substrates for use as integrated heat sinks for high intensity LEDs"; Poster: International Conference of IMAPS Poland Chapter, Pultusk, Poland; 09-21-2008 - 09-24-2008; in: "Abstracts Proceedings of the XXXII International Conference of IMAPS Poland Chapter", (2008), ISBN: 978-83-917701-6-0; 1 pages.

7. N. Blaž, L. Živanov, G. Radosavljević, M. Unger, W. Smetana: "Determination of electric and magnetic characteristics of basic electronic materials"; Talk: Junior Scientist Conference 2010 (JSC 2010), Vienna, Austria; 04-07-2010 - 04-09-2010; in: "Book of Abstracts", (2010), ISBN: 978-3-200-01797-9; 163 - 164.

8. E. Eisermann, K. Höll, W. Smetana, W. Tusler, M. Unger, J. Withmarsh: "Comparison of low cost, insulated aluminium substrates used as integrated heat sinks with conventional technology"; Poster: International Conference of IMAPS Germany Chapter, Munich, Germany; 10-14-2008 - 10-15-2008; in: "Proceedings of the International Conference of IMAPS German Chapter", (2008), ISBN: 978-83-917701-6-0; 1 pages.

9. G. Langer, M. Leitgeb, J. Nicolics, M. Unger, H. Hoschopf, F. Wenzl: "Advanced Thermal Management Solutions on PCBs for High Power Applications - Best Paper Award"; Talk: Ipc Apex Expo 2014, Las Vegas, Nevada, USA; 03-25-2014 - 03-27-2014; in: "Proceedings", (2014), 15 pages.

10. G. Mišković, J. Fernandez, H. Homolka, M. Unger, L. Vuckovic, G. Radosavljević: "Physical and electrical Characterisation of LTCC Tapes"; Talk: 37th International Spring Seminar on Electronics Technology, Dresden; 05-07-2014 - 05-11-2014; in: "Proceedings 37th Int. Spring Seminar on Electronics Technology", (2014), ISBN: 978-1-4799-4455-2; 110 - 111.

11. G. Radosavljević, W. Smetana, A. Marić, L. Živanov, M. Unger, G. Stangl, G. Stojanovic: "A Sensitivity Improvement of a Non Contact LTCC Resonant Pres¬sure Sensor"; Poster: XXXIII International Conference of IMAPS Poland Chapter, Gliwice-Pszczyna, Poland; 09-21-2009 - 09-24-2009; in: "Proceedings of the XXXIII International Conference of IMAPS Poland Chapter", (2009), ISBN: 978-83-917701-7-7; 304 - 308.

12. G. Radosavljević, W. Smetana, A. Marić, L. Živanov, M. Unger, G. Stojanovic: "LTCC micro force sensor"; Talk: Second ReClMiCo Workshop: New Trends in Integrated Microsystems and Components, Novi Sad, Serbia; 03-05-2010 - 03-06-2010; in: "Proceedings", University of Novs Sad, Faculty of Technical Science, (2010), ISBN: 978-86-7892-287-9; 67 - 73.

13. G. Radosavljević, W. Smetana, A. Marić, L. Živanov, M. Unger, G. Stojanovic: "Micro force sensor fabricated in the LTCC technology"; Poster: 27th International Conference on Microelectronics (MIEL 2010), Nis, Serbia; 05-16-2010 - 05-19-2010; in: "Conference Proceedings", (2010), ISBN: 978-1-4244-7200-0; 221 - 224.

14. G. Radosavljević, L. Živanov, A. Marić, L. Nad, W. Smetana, M. Unger: "Performance Improvement of a Resonant Pressure Sensor by Means of Model Based

Design Optimisation"; Poster: IEEE SENSORS 2008 Conference, LECCE, Italien; 10-25-2008 - 10-29-2008; in: "Proceedings of the 7th Conference on Sensors IEEE Sensors 2008", (2008), 1008 - 1011.

15. G. Radosavljević, L. Živanov, A. Marić, G. Stojanovic, W. Smetana, M. Unger: "Mikro senzor sile namenjen za rad u ekstremnim uslovima okruzenja (in Serbian)"; Talk: VII Simpozijum industrijska elektronika INDEL 2008, Banja Luka, Bosnia and Hercegovina; 11-06-2008 - 11-08-2008; in: "Conference Proceedings", (2008), 1 - 4.

16. G. Radosavljević, L. Živanov, L. Nad, A. Marić, W. Smetana, M. Unger: "Resonant pressure sensor designed for the LTCC-technology"; Poster: ETRAN 2008, Palic, Serbia; 06-08-2008 - 06-12-2008; in: "Proceedings of 52nd ETRAN Conference", (2008), MO1.5-1 - MO1.5-4.

17. W. Smetana, G. Radosavljević, M. Unger, L. Živanov, T. Koch: "A Capacitive Temperature Sensor Concept Realized in LTCCTechnology"; Poster: Smart Systems Integration 2009 (SSI), Brussels, Belgium; 03-10-2009 - 03-11-2009; in: "Smart Systems Integration 2009 Proceedings", (2009), ISBN: 978-3-89838-616-6; 1 - 4.

18. M. Unger, J. Nicolics, G. Langer, F. Wenzl, W. Nemitz, P. Fulmek, S. Schweitzer: "Thermal Performance Study of Direct Attached High-Power LEDs using an Innovative Submount Technique"; Talk: Electronics System-Integration Technology Conference (ESTC 2014), Helsinki, Finland; 09-16-2014 - 09-18-2014; in: "Proceedings ESTC 2014", (2014), 171 - 176.

19. M. Unger, J. Nicolics, G. Langer, F. Wenzl, W. Nemitz, P. Fulmek, S. Schweitzer: "Thermal Performance Study of Direct Attached High-Power LEDs using an Innovative Submount Technique"; Talk: 37th International Spring Seminar on Electronics Technology, Dresden; 05-07-2014 - 05-11-2014; in: "Proceedings of the 37th ISSE", (2014), ISBN: 978-1-4799-4026-4; 6 pages.

20. M. Unger, J. Nicolics, M. Morianz, H. Stahr, F. Dosseul, D. Manessis: "Thermomechanical comparison of novel embedded high-power packages using FEM-simulations"; Talk: IMAPS Nordic Conference 2015, Helsingor, Denmark; 06-08-2015 - 06-09-2015; in: "Proceedings of IMAPS Nordic Conference 2015", (2015), 126 - 133.

21. M. Unger, G. Radosavljević, W. Smetana, L. Živanov, T. Koch: "Parameters Governing the Sensor Characteristic of Capacitive Temperature Sensors built up in LTCC-Technology"; Poster: 32nd International Spring Seminar on Electronics

Technology (ISSE), Brno, Czech Republic; 05-13-2009 - 05-17-2009; in: "ISSE 2009 Conference Proceedings", (2009), ISBN: 978-1-4244-4260-7; 112 - 113.

22. M. Unger, W. Smetana, W. Ehrenzweig: "Mechanical characteristics of LTCC (Low Temperature Cofired Ceramics) -tapes for mechanical application"; Talk: International Spring Seminar on Electronics Technology (ISSE), Cluj-Napoca, Romania; 05-09-2007 - 05-13-2007; in: "Proceedings of 30th ISSE 2007", (2007), ISBN: 1-4244-1218-8; 59 - 64.

23. M. Unger, W. Smetana, T. Koch, G. Radosavljević: "High Temperature Characteristics of various LTCC-Tapes"; "Proceedings of the XXXIII International Conference of IMAPS Poland Chapter", (2009), ISBN: 978-83-917701-7-7; 355 - 358.

24. M. Unger, W. Smetana, G. Radosavljević, L. Živanov, A. Marić, T. Koch, J. Fleig, M. Ahrens: "High temperature characteristics of various LTCC-tapes"; Talk: Second ReClMiCo Workshop: New Trends in Integrated Microsystems and Components, Novi Sad, Serbia; 03-05-2010 - 03-06-2010; in: "New Trends in Integrated Microsystems and Components", University of Novi Sad, Faculty of Technical Science, (2010), ISBN: 978-86-7892-287-9; 16 - 21.

25. M. Unger, W. Smetana, G. Radosavljević, L. Živanov, L. Nad, A. Marić: "A Wireless Readout Temperature Sensor Realized in LTCC-Technology"; "Abstracts Proceedings of the XXXII International Conference of IMAPS Poland Chapter", (2008), ISBN: 978-83-917701-6-0;

# Bibliography

[1] M. Unger, W. Smetana, T. Koch, and G. Radosavljevic. High temperature characteristics of various ltcc-tapes. In *Proceedings of the XXXIII International Conference of IMAPS Poland Chapter*, pages 355 – 358, 2009.

[2] M. Unger, W. Smetana, and W. Ehrenzweig. Mechanical characteristics of ltcc (low temperature cofired ceramics) -tapes for mechanical application. In *30th International Spring Seminar on Electronics Technology (ISSE)*, pages 59–64, May 2007. doi: 10.1109/ISSE.2007.4432821.

[3] M Unger, J Fleig, M Ahrens, W Smetana, and G Radosavljevic. Permittivity and conductivity of various ltcc-tapes at high temperature. 2007. doi: 10.1109/ISSE. 2010.5547263.

[4] Peter W. Carr, Ruth M. Doherty, Mortimer J. Kamlet, Robert W. Taft, Wayne Melander, and Csaba Horvath. Study of temperature and mobile-phase effects in reversed-phase high-performance liquid chromatography by the use of the solvatochromic comparison method. *Analytical Chemistry*, 58(13):2674–2680, 1986. doi: 10.1021/ac00126a021. URL http://dx.doi.org/10.1021/ac00126a021. PMID: 3813011.

[5] M E Peterson, R M Daniel, M J Danson, and R Eisenthal. The dependence of enzyme activity on temperature: determination and validation of parameters. *Biochemical Journal*, 402:331–337, 2007. doi: 10.1042/bj20061143. URL http://opus.bath.ac.uk/3517/. ID number: ISI:000244762500013.

[6] Mikio Hoshino, Kiyoshi Ikehara, Masashi Imamura, and Yoshimasa Hama. Temperature dependence of absorption spectra of chlorophyll a in hydrocarbons over the temperature range 300–77 k. enthalpy and entropy changes for the formation of dimeric chlorophyll a. *Bulletin of the Chemical Society of Japan*, 56(1):208–211, 1983.

[7] David Ross, Michael Gaitan, and Laurie E. Locascio. Temperature measurement in microfluidic systems using a temperature-dependent fluorescent dye. *Analytical*

*Chemistry*, 73(17):4117–4123, 2001. doi: 10.1021/ac010370l. URL http://dx.doi.org/10.1021/ac010370l. PMID: 11569800.

[8] Jun-ichi Yoshida, Aiichiro Nagaki, and Takeshi Yamada. Flash chemistry: Fast chemical synthesis by using microreactors. *Chemistry – A European Journal*, 14 (25):7450–7459, 2008. ISSN 1521-3765. doi: 10.1002/chem.200800582. URL http://dx.doi.org/10.1002/chem.200800582.

[9] W Kinzy Jones, Yanqing Liu, Brooks Larsen, PENG Wang, and Marc Zampino. Chemical, structural and mechanical properties of the ltcc tapes. In *PROCEEDINGS-SPIE THE INTERNATIONAL SOCIETY FOR OPTICAL ENGINEERING*, pages 669–674. International Society for Optical Engineering; 1999, 2000.

[10] Tyge Greibrokk and Thomas Andersen. High-temperature liquid chromatography. *Journal of Chromatography A*, 1000(1):743–755, 2003.

[11] L. Szepesy and V. Háda. Influence of column characteristics on retention and selectivity in rp-hplc. *Chromatographia*, 54(5):419–419, Sep 2001. ISSN 1612-1112. doi: 10.1007/BF02492697. URL http://dx.doi.org/10.1007/BF02492697.

[12] Collin D. Wick, J.Ilja Siepmann, Wendy L. Klotz, and Mark R. Schure. Temperature effects on the retention of n-alkanes and arenes in helium–squalane gas–liquid chromatography: Experiment and molecular simulation. *Journal of Chromatography A*, 954(1–2):181 – 190, 2002. ISSN 0021-9673. doi: http://dx.doi.org/10.1016/S0021-9673(02)00171-1. URL http://www.sciencedirect.com/science/article/pii/S0021967302001711.

[13] Christopher F. Blanford. The birth of protein electrochemistry. *Chem. Commun.*, 49:11130–11132, 2013. doi: 10.1039/C3CC46060F. URL http://dx.doi.org/10.1039/C3CC46060F.

[14] Karol Malecha, Dorota G. Pijanowska, Leszek J. Golonka, and Piotr Kurek. Low temperature co-fired ceramic (ltcc)-based biosensor for continuous glucose monitoring. *Sensors and Actuators B: Chemical*, 155(2):923 – 929, 2011. ISSN 0925-4005. doi: http://dx.doi.org/10.1016/j.snb.2011.01.002. URL http://www.sciencedirect.com/science/article/pii/S0925400511000050.

[15] Vincent Miralles, Axel Huerre, Florent Malloggi, and Marie-Caroline Jullien. A review of heating and temperature control in microfluidic systems: techniques and applications. *Diagnostics*, 3(1):33–67, 2013.

[16] Ulrich Brackmann. Laser dyes. *Göttingen (Germany): Lambda Physik AG. D*, 37079, 2000.

[17] Korey Moeller, Jason Besecker, Greg Hampikian, Amy Moll, D Plumlee, John Youngsman, and Janet M Hampikian. A prototype continuous flow polymerase chain reaction ltcc device. In *Materials science forum*, volume 539, pages 523–528. Trans Tech Publ, 2007.

[18] Paweł Bembnowicz, Małgorzata Małodobra, Wojciech Kubicki, Patrycja Szczepańska, Anna Górecka-Drzazga, Jan Dziuban, Anna Jonkisz, Anna Karpiewska, Tadeusz Dobosz, and Leszek Golonka. Preliminary studies on ltcc based pcr microreactor. *Sensors and Actuators B: Chemical*, 150(2):715–721, 2010.

[19] Kai Wang, Yangcheng Lu, Huawei Shao, and Guangsheng Luo. Improving selectivity of temperature-sensitive exothermal reactions with microreactor. *Industrial & Engineering Chemistry Research*, 47(14):4683–4688, 2008.

[20] Jingyi An, Laurence Bagnell, Teresa Cablewski, Christopher R Strauss, and Robert W Trainor. Applications of high-temperature aqueous media for synthetic organic reactions. *The Journal of organic chemistry*, 62(8):2505–2511, 1997.

[21] Kaoru Fujimoto, Kohji Omata, Tsutomu Shikada, and Hiroo Tominaga. Vapor phase carbonylation of organic compounds over supported transition metal catalysts. 2. synthesis of acetic acid and methyl acetate from methanol with nickel-active carbon catalyst. *Industrial and Engineering Chemistry Product Research and Development*, 22(3):436–439, 1983. doi: 10.1021/i300011a010. URL http://pubs.acs.org/doi/abs/10.1021/i300011a010.

[22] M.W. de Lange, J.G. van Ommen, and L. Lefferts. Deoxygenation of benzoic acid on metal oxides: 1. the selective pathway to benzaldehyde. *Applied Catalysis A: General*, 220(1–2):41 – 49, 2001. ISSN 0926-860X. doi: http://dx.doi.org/10. 1016/S0926-860X(01)00703-7. URL http://www.sciencedirect.com/science/article/pii/S0926860X01007037.

[23] R. H. Reitsema and N. L. Allphin. Chromate oxidation of alkylaromatic compounds. *The Journal of Organic Chemistry*, 27(1):27–28, 1962. doi: 10.1021/jo01048a006. URL http://pubs.acs.org/doi/abs/10.1021/jo01048a006.

[24] Bruno Balluch, Ibrahim Atassi, Michael Weilguni, Goran Radosavljevic, and Arsim Myrtezani. Realisation of hermetically tight joints for microfluidic applications in ltcc - technology. *Additional Conferences (Device Packaging, HiTEC, HiTEN, & CICMT)*, 2012(CICMT):000423–000427, 2012. doi: 10.4071/CICMT-2012-WA414. URL http://dx.doi.org/10.4071/CICMT-2012-WA414.

[25] Minh Tho Nguyen, Debasis Sengupta, Greet Raspoet, and Luc G. Vanquicken-borne. Theoretical study of the thermal decomposition of acetic acid: Decarboxylation versus dehydration. *The Journal of Physical Chemistry*, 99(31):11883–11888, 1995. doi: 10.1021/j100031a015. URL http://pubs.acs.org/doi/abs/10.1021/j100031a015.

[26] Klemens Graf Gerd Schulz. Regelungstechnik1:lineare und nichtlineare regelung, rechnergestützter reglerentwurf. pages 181–182. Walter de Gruyter GmbH & Co KG. ISBN 9783110414462.

[27] P.D.T.O' CONNOR. Handbook of microelectronics packaging and interconnection technologies, f. n. sinnadurai (ed). electrochemical publications, 1985. *Quality and Reliability Engineering International*, 2(4). doi: 10.1002/qre.4680020418. URL https://onlinelibrary.wiley.com/doi/abs/10.1002/qre.4680020418.

[28] G. Fasching. *Werkstoffe Für Die Elektrotechnik*. Springer Vienna, 2005. ISBN 9783211271872.

[29] J. Nicolics M. Unger, W. Smetana. Analyses of fluid temperature profile in a continuous-flow heater for lab-in-module application. In *Berichte aus der Elektrotechnik: Proceedings E!4570 IPCTECH. New Generation of 3-D Integrated Passive Components & Microsystems in LTCC-Technology*, volume 1, pages 92 – 107, 2011.

[30] H. Bruus. Theoretical microfluidics. page 48–51. Oxford University Press, 2008. ISBN 978–0–19–923508–7.

[31] Walter Smetana, Bruno Balluch, Günther Stangl, Erwin Gaubitzer, Michael Edetsberger, and Gottfried Köhler. A multi-sensor biological monitoring module built up in ltcc-technology. *Microelectronic Engineering*, 84(5):1240–1243, 2007.

[32] PS Christel. Biocompatibility of surgical-grade dense polycrystalline alumina. *Clinical orthopaedics and related research*, 282:10–18, 1992.

[33] J. Nicolics and L. Musiejovsky. Einführung in die wärmelehre und benutzerhandbuch - trescom. Institut für Werkstoffe der Elektrotechnik, TU-Wien, 1995. ISBN 3-85465-001-9.

[34] Walter Smetana, Bruno Balluch, Günther Stangl, Sigrid Lüftl, and Sabine Seidler. Processing procedures for the realization of fine structured channel arrays and bridging elements by ltcc-technology. *Microelectronics Reliability*, 49(6):592–599, 2009. doi: 10.1016/j.microrel.2009.02.023. URL http://dx.doi.org/10.1016/j.microrel.2009.02.023.

[35] David Ross, Michael Gaitan, and Laurie E. Locascio. Temperature measurement in microfluidic systems using a temperature-dependent fluorescent dye. *Analytical Chemistry*, 73(17):4117–4123, 2001. doi: 10.1021/ac010370l. URL http://dx.doi.org/10.1021/ac010370l. PMID: 11569800.

[36] M. Unger and J. Nicolics. Discretisation and data reduction algorithm for fe modelling of complex multilayer pcbs with embedded components. In *2018 41st International Spring Seminar on Electronics Technology (ISSE)*, pages 1–6, May 2018. doi: 10.1109/ISSE.2018.8443671.

[37] M. Unger, H. Stahr, M. Morianz, J. Nicolics, and F. Dosseul. Miniaturized power-diode package with superior thermal performance using embedding technology. In *2016 39th International Spring Seminar on Electronics Technology (ISSE)*, pages 97–105, May 2016. doi: 10.1109/ISSE.2016.7563169.

[38] M. Franz, M. Unger, G. Schmid, and J. Nicolics. Environmental assessment of a new developed camera system for automotive application. In *2018 41st International Spring Seminar on Electronics Technology (ISSE)*, pages 1–8, May 2018. doi: 10.1109/ISSE.2018.8443694.

[39] C. Barry Carter M. Grant Norton. Ceramic materials: Science and engineering. Springer-Verlag New York, 2007. doi: 10.1007/978-1-4614-3523-5.

[40] Fred D. Barlow and Aicha Elshabini. Ceramic interconnect technology handbook. CRC Press/Taylor & Francis, 2007.

[41] A. J. Blodgett and D. R. Barbour. Thermal conduction module: A high-performance multilayer ceramic package. *IBM Journal of Research and Development*, 26(1):30–36, Jan 1982. ISSN 0018-8646. doi: 10.1147/rd.261.0030.

[42] S Toskov, A Maric, N Blaz, G Miskovic, and G Radosavljevic. Properties of ltcc dielectric tape in high temperature and water environment. *International Journal of Materials, Mechanics and Manufacturing*, 1(4), 2013. doi: 10.7763/IJMMM.2013.V1.72.

[43] Norman E. Dowling. Mechanical behavior of materials : Engineering methods for deformation, fracture, and fatigue. pages 852–855. Upper Saddle River, N.J. : Pearson/Prentice Hall, 2007.

[44] Evgenij Barsoukov and J. Ross Macdonald. Impedance spectroscopy theory, experiment, and applications 2nd ed. pages 72–74. John Wiley & Sons. ISBN 0-471-64749-7.

[45] M. Unger, M. Weilguni, and W. Smetana. *Machbarkeitsstudie über ein kombiniertes Heiz- und Temperaturmesssystem für eine Analyseeinheit.* 2009.

[46] M. Unger, J. Nicolics, M. Morianz, H. Stahr, F. Dosseul, and D. Manessis. Thermomechanical comparison of novel embedded high-power packages using fem-simulations. In *Proceedings of IMAPS Nordic Conference 2015*, pages 126 – 133, 2015. ISBN 978-1-5108-0813-3.

[47] Hyung Joo Kim and Colby C. Swan. Voxel-based meshing and unit-cell analysis of textile composites. *Int. Journal for Numerical Methods in Engineering*, 56:977–1006, 2003. doi: 10.1002/nme.594.

[48] Liz U. Gron and Amanda S. Tinsley. Tailoring aqueous solvents for organic reactions: Heck coupling reactions in high temperature water. *Tetrahedron Letters*, 40(2):227 – 230, 1999. ISSN 0040-4039. doi: http://dx.doi.org/10.1016/S0040-4039(98)02323-5. URL http://www.sciencedirect.com/science/article/pii/S0040403998023235.

[49] Karol Malecha, Dorota G. Pijanowska, Leszek J. Golonka, and Władysław Torbicz. {LTCC} microreactor for urea determination in biological fluids. *Sensors and Actuators B: Chemical*, 141(1):301 – 308, 2009. ISSN 0925-4005. doi: http://dx.doi.org/10.1016/j.snb.2009.06.026. URL http://www.sciencedirect.com/science/article/pii/S0925400509005012.

[50] Gary Patterson†. Modeling and scale-up of mixing- and temperature-sensitive chemical reactions. *Industrial & Engineering Chemistry Research*, 44(14):5325–5341, 2005. doi: 10.1021/ie049161s. URL http://dx.doi.org/10.1021/ie049161s.

[51] † Hideyuki F. Arata, *, § Yannick Rondelez, ‡ Hiroyuki Noji, , and Hiroyuki Fujita†. Temperature alternation by an on-chip microheater to reveal enzymatic activity of -galactosidase at high temperatures. *Analytical Chemistry*, 77(15):4810–4814, 2005. doi: 10.1021/ac050385+. URL http://dx.doi.org/10.1021/ac050385+. PMID: 16053292.

[52] H. Bartsch de Torres, C. Rensch, M. Fischer, A. Schober, M. Hoffmann, and J. Müller. Thick film flow sensor for biological microsystems. *Sensors and Actuators A: Physical*, 160(1–2):109 – 115, 2010. ISSN 0924-4247. doi: http://dx.doi.org/10.1016/j.sna.2010.04.010. URL http://www.sciencedirect.com/science/article/pii/S092442471000172X.

[53] Torsten Rabe, Petra Kuchenbecker, Baerbel Schulz, and Martin Schmidt. Hot embossing: An alternative method to produce cavities in ceramic multilayer. *International Journal of Applied Ceramic Technology*, 4(1):38–46, 2007. ISSN 1744-7402. doi: 10.1111/j.1744-7402.2007.02117.x. URL http://dx.doi.org/10.1111/j.1744-7402.2007.02117.x.

[54] Laurence Suzzarini, Jian Lin, and Zhi Yuan Wang. Improved synthesis of benzocyclobutenone by flash vacuum pyrolysis. *Tetrahedron Letters*, 39(13):1695 – 1696, 1998. ISSN 0040-4039. doi: http://dx.doi.org/10.1016/S0040-4039(98)00133-6. URL http://www.sciencedirect.com/science/article/pii/S0040403998001336.

[55] L.J. Golonka, H. Roguszczak, T. Zawada, J. Radojewski, I. Grabowska, M. Chudy, A. Dybko, Z. Brzozka, and D. Stadnik. {LTCC} based microfluidic system with optical detection. *Sensors and Actuators B: Chemical*, 111–112:396 – 402, 2005. ISSN 0925-4005. doi: http://dx.doi.org/10.1016/j.snb.2005.03.065. URL http://www.sciencedirect.com/science/article/pii/S0925400505003059. Eurosensors {XVIII} 2004The 18th European Conference on Solid-State Transducers.

[56] Wenzhi Hu, Kyoshi Hasebe, and Paul R. Haddad. Temperature effects on retention in reversed-phase liquid chromatography of nucleosides and their bases using water as the mobile phase. *Anal. Commun.*, 34:311–314, 1997. doi: 10.1039/A705426B. URL http://dx.doi.org/10.1039/A705426B.

[57] Chiara Fasciani, Carlos J. Bueno Alejo, Michel Grenier, José Carlos Netto-Ferreira, and J. C. Scaiano. High-temperature organic reactions at room temperature using plasmon excitation: Decomposition of dicumyl peroxide. *Organic Letters*, 13 (2):204–207, 2011. doi: 10.1021/ol1026427. URL http://dx.doi.org/10.1021/ol1026427. PMID: 21142017.

[58] D Haidacher, A Vailaya, and C Horváth. Temperature effects in hydrophobic interaction chromatography. *Proceedings of the National Academy of Sciences*, 93(6):2290–2295, 1996. URL http://www.pnas.org/content/93/6/2290.abstract.

[59] F Morhard, J Pipper, R Dahint, and M Grunze. Immobilization of antibodies in micropatterns for cell detection by optical diffraction. *Sensors and Actuators B: Chemical*, 70(1–3):232 – 242, 2000. ISSN 0925-4005. doi: http://dx.doi.org/10.1016/S0925-4005(00)00574-8. URL http://www.sciencedirect.com/science/article/pii/S0925400500005748. Special Issue in Memory of Professor Wolfgang Gopel.

[60] Ulrike Deisinger, Tobias Fey, and Andreas Roosen. Realisation of large cavities in multilayer ceramics by cold low pressure lamination and their characterisation by

ct. *Additional Conferences (Device Packaging, HiTEC, HiTEN, & CICMT)*, 2012 (CICMT):000263–000268, 2012. doi: 10.4071/CICMT-2012-TP66. URL http://dx.doi.org/10.4071/CICMT-2012-TP66.

[61] Darko Belavic, Marko Hrovat, Gregor Dolanc, Marina Santo Zarnik, Janez Holc, and Kostja Makarovic. Design of ltcc-based ceramic structure for chemical microreactor. *Radioengineering*, 21(1):195–200, 2012.

[62] M Schirmer, J Uhlemann, L Rebenklau, T Bauer, and K-J Wolter. 3d-microfluidic reactor in ltcc. In *2008 31st International Spring Seminar on Electronics Technology*, pages 484–489. IEEE, 2008.

[63] M. Unger, J. Fleig, M. Ahrens, W. Smetana, and G. Radosavljevic. Permittivity and conductivity of various ltcc-tapes at high temperature. In *33rd International Spring Seminar on Electronics Technology, ISSE 2010*, pages 93–98, May 2010. doi: 10.1109/ISSE.2010.5547263.

[64] Vincent Miralles, Axel Huerre, Florent Malloggi, and Marie-Caroline Jullien. A review of heating and temperature control in microfluidic systems: Techniques and applications. *Diagnostics*, 3(1):33, 2013. ISSN 2075-4418. doi: 10.3390/diagnostics3010033. URL http://www.mdpi.com/2075-4418/3/1/33.

[65] Tahseen Razzaq, Toma N. Glasnov, and C. Oliver Kappe. Continuous-flow microreactor chemistry under high-temperature/pressure conditions. *European Journal of Organic Chemistry*, 2009(9):1321–1325, 2009. ISSN 1099-0690. doi: 10.1002/ejoc.200900077. URL http://dx.doi.org/10.1002/ejoc.200900077.